Metal Oxide -- Organic Nano-composite and Mesoporous Oxide Films: Fundamental Properties And Applications

Milsom, Elizabeth Victoria

Award date:
2007

Awarding institution:
University of Bath

Metal Oxide – Organic Nano-composite and Mesoporous Oxide Films: Fundamental Properties and Applications

Elizabeth Victoria Milsom

A thesis submitted for the degree of Doctor of Philosophy

University of Bath

Department of Chemistry

October 2007

ProQuest LLC
789 East Eisenhower Parkway
P.O. Box 1346
Ann Arbor, MI 48106-1346

Contents

Acknowledgements

I would like to thank:

- EPSRC for funding
- My supervisor Dr. Frank Marken
- Members of the Marken group past and present, especially: Mike Bonné, Stuart McDonald, Rob French, Najoua Katif, Jan Novak, Katy McKenzie, Susan Scott
- Hugh Perrott for help with the AFM measurements
- Dr. Karen Edler for the SAXS/WAXS measurements
- Prof. Alan Bond and group at Monash University
- Friends and colleagues in the chemistry department, especially: Amanda Chmura, David Bandy, Tom Williams
- My family for their support

Abstract

This thesis describes work carried out during the three years of a project entitled 'Metal Oxide – Organic Nano-composite and Mesoporous Oxide Films: Fundamental Properties and Applications'. The work carried out focuses on nanocomposite films prepared mainly with semiconducting TiO_2 nanoparticles. Initially an investigation is carried out into the structural and electronic properties of a TiO_2-Nafion® film electrode, employing electrochemical and imaging techniques, before more complex redox systems are introduced.

Films of nanoparticulate TiO_2 with the organic binder flavin adenine dinucleotide (FAD) are readily formed with controlled thickness. AFM and SEM microscopy confirms films of 30 nm to 300 nm. FAD as a redox active binder is shown to exhibit two distinct electrochemical reduction responses with direct reduction and indirect reduction via TiO_2. New methods for the measurements of electron diffusion within the mesoporous oxide are presented. A dramatic electronic difference for films before and after calcination is observed.

Structured films of TiO_2 nanoparticles and gold nanoparticles (nominal 20 nm diameter) are formed via a layer-by-layer deposition procedure. TiO_2 nanoparticles are deposited with a Nafion® polyelectrolyte binder and gold nanoparticles are incorporated employing a poly(diallyl-dimethylammonium chloride) polyelectrolyte binder. Calcination at 500°C gives a stable mesoporous TiO_2 – gold nanocomposite. The films are characterised electrochemically and by FEGSEM. It is shown that the oxidation of NO occurs as a highly effective electrocatalytically amplified process at the surface of the gold nanocomposite probably with co-evolution of oxygen.

The immobilisation of hemoglobin as a model biological redox centre is investigated in 40nm TiO_2 and SnO_2- poly(diallyl-dimethylammonium chloride) composite films. It is shown that, perhaps surprisingly, methemoglobin is denatured and even demetallated in the presence of polyelectrolyte or the charged TiO_2 or SnO_2 surface to give Fe(III/II) immobilized in electrochemically active form within the film. Most of this Fe(III/II) can be sequestered and identified in a test reaction with ethylenediaminetetraacetic acid (EDTA).

The physical and redox properties of TiO_2 nanotubes are investigated and compared to TiO_2 nanoparticles. It is shown that adsorption of redox species onto TiO_2 nanoparticles (pzc ca. 6) and on TiO_2 nanotubes (pzc ca. 3) are fundamentally different. Cationic redox systems readily adsorb onto the nanotube material but not onto the nanoparticulate film. Electron transport through both types of TiO_2 materials occurs and redox systems such as the cytochrome *c* (Fe(III/II)) are readily detected.

Finally the method of large-amplitude sinusoidally modulated voltammetry is used to investigate the conductivity of a TiO_2-Nafion® film electrode and probe the reduction mechanism of immobilised ferrocenylmethyl-trimethylammonium$^+$. The low capacitive background of the second harmonic response is exploited to simplify data read out. Application of this system as a reference-free pH probe is explored.

Aims

The project 'Metal Oxide – Organic Nano-composite and Mesoporous Oxide Films: Fundamental Properties and Applications' focuses on the formation of layered oxide films (from nanoparticulate TiO_2, SnO_2, or TiO_2 nanotubes) with small organic binder molecules. Mesoporous functionalised films are formed with controlled thickness in a layer-by-layer approach. By depositing the films onto electrode surfaces, transport and redox properties can be studied.

The main objectives of the study are (i) to investigate how electron and ion transport occurs in mesoporous oxide materials, (ii) how new types of metal oxide thin film structures can be produced, (iii) how different types of oxides affect the behaviour of these thin films, and (iv) how films with combined electron/ion transport can be beneficially applied.

1. Introduction to Nanocomposite Films, Deposition Methods and Experimental Techniques

1.1 Introduction to Nanocomposite Films

1.1.1 Nanocomposites

The design of new composite materials is driven by the desire to secure a property or combination of properties that are not available in any of the individual components. Improved strength, mechanical attributes, high electrical and thermal conductivities are all characteristics that have been sought after in composite materials. In the context of the area of electrochemistry/ photochemistry/ photophysics composite films and particles containing a semiconducting based component have been studied and utilized for their improved electrical or optical response[1]. Often these systems come under the category of nanocomposites, where at least one of the phase dimensions is in the nanometre-size range. Nanoparticles often display properties between those described by solid state physics and the quantum effects of atoms and molecules. Special chemical and physical properties have been shown to be dependent on the particle size, including optical properties, magnetic properties, melting points and surface reactivity[2]. These qualities have been utilized as either an evaluation tool or in applications including photocatalysis, photovoltaic cells, light emitting devices, sensors and fuel cells.

There are many ways to produce a nanocomposite thin film including spin coating, sputter coating, thermal deposition, chemical self assembly and Langmuir- Blodgett techniques. However an area of recent substantial growth is the use of non-covalent interactions to form electrostatic layer-by-layer assemblies, first introduced by Decher in 1991[3] and the primary method for formation of nanocomposites in this thesis. The popularity of the method is due to the ability to create highly diverse thin films with nearly an unlimited range of functional groups incorporated into the structure. The area has progressed to include: electroactive polymers, organic dyes, semiconductor quantum dots, and a wide variety of proteins and other biosystems[4, 5].

Techniques that can follow the layer-by-layer deposition of films include the Quartz Crystal Microbalance (QCM) technique[6]. Imaging techniques such as AFM and FEGSEM allow thickness and film morphology to be studied. Neutron and X-ray diffraction techniques can give insight into the order and porous nature of the films. Electrochemistry is an important tool for the characterisation of mesoporous media but also allows for the development of modified electrodes and sensors by incorporating redox active centres into the nanocomposite films. These thin film environments are of interest for developing modified electrodes as they have very high surface areas, allow diffusion within the pores and provide an extensive triple interface region where the electrode is in contact with both the solution phase and membrane material[7]. Already applications include sensors[8], integrated chemical systems[9] and electrocatalysis[10].

1.1.2 Nanoparticles

The term nanoparticle can be applied to any particle smaller than typically 100nm and containing 20 – 150 000 atoms. Nanoparticles are classified according to their material into metallic, semiconducting or polymeric, and can be synthesised into a variety of shapes such as spheres, rods, wires or tubes[11]. Nanoparticles have found uses in a wide variety of areas including electronics, magnetic and optoelectronics, biomedicine, pharmaceuticals, cosmetics, catalysis, and environmental detection and monitoring.

Nanoparticulate materials have been attractive objects of chemical research due to their bridging status between the solid (bulk) material and molecule[2]. Because of their small size, nanoparticles can exhibit different physical properties from the bulk material. Most of the difference in properties stems from the extremely high surface area of nanoparticles and consequently the large surface to interior ratio of atoms. Surface, edge and corner atoms are less coordinated and therefore less stable than atoms in the interior of the particle or cluster. For this reason, the corner atoms normally exhibit the highest affinity to form bonds to adsorbate molecules, followed by the edge and the in-plane surface atoms. The consequence of such can be enhanced catalytic properties for nanoparticles due to the higher number of binding

sites available. Similarly these size and stability effects can change the nanoparticles physical properties, such as melting points, for the same material when in nanoparticulate compared to bulk form.

1.1.3 Semiconducting Metal Oxide Nanoparticles

The mesoporous structure of the layered nanocomposite films of interest in this thesis are formed primarily from metal-oxide nanoparticles, with small organic molecules acting as either binders or as redox active sites. Semi-conducting nanoparticles are particularly of interest due to their electrical conductivity and light adsorption/emission characteristics. Common semi-conducting nanoparticles used to form thin films have in the past included ZnO, TiO_2, SnO_2, MoO_3 and Fe_2O_3.

In order to understand the processes occurring in the nanocomposite film, the transfer of electrons through the semi-conducting nanoparticles needs to be understood. To gain an understanding of intra-particle electron transfer, the band model of solids is used to describe the energy levels within the metal-oxide. As described by the Pauli Exclusion Principle, the energy levels of identical overlapping electronic orbitals cannot be equal[12]. In a perfect crystal, where there are a large number of atoms, the discrete energy levels of the atoms broaden when the orbitals overlap forming an energy band. The orbitals occupied by the valence electrons are called the 'valence band' of the solid, normally a few eV broad. The band associated with the first excited state, normally unoccupied by electrons is called the 'conduction band' of the solid. Mobile electrons in the conduction band and holes in the valence band normally carry electrical current in the solid.

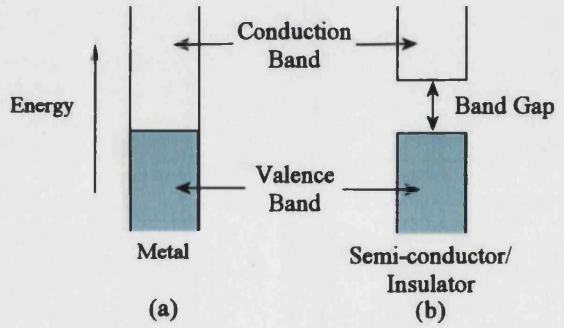

Figure 1.1 Band model of solids diagram for (a) a metal and (b) a semiconductor/ insulator

A forbidden region of energy called the 'band gap' is present in insulators and semiconductors, between a filled valence band and an empty conduction band. For a perfect crystal there are no allowed energy levels for electrons in the band gap. However the band gap model is only accurate for the perfect crystal; for a real crystal with impurities and imperfections the model is incomplete. Impurities and imperfections in the crystal give rise to localised energy levels, such that if an electron or hole occupies one of these levels i) it is localised (it no longer has a wave function extending through the crystal) and ii) it has an energy level in the band gap. Impurities can separated into donors of electrons, often into the conduction band, and acceptors of electrons, either creating a hole in the valence band or extracting an electron from the conduction band.

For semi- conductors the creation of holes in the valence band and electrons in the conduction band can occur when the sample is under illumination and the excitation of an electron across the band gap occurs by adsorption of a photon. The excitation is initiated by light adsorption with energy equal to or greater than the band gap of the semi-conductor[13]. Alternatively the application of an electrical potential to a semiconductor can result in the injection of electrons from an electrode into the conduction band of the semi-conductor. The fate of the separated electron-hole pair can then follow several pathways. Recombination of the electron-hole pair can occur either in the semi-conductor volume or at the surface with the evolution of heat. Alternatively and more importantly electron transfer to an adsorbed organic or inorganic species, or to the solvent, can occur from the migration of electrons and holes to the semi-conductor surface. Photo-induced charge transfer from the semi-conductor to the adsorbed species is termed heterogeneous photocatalysis. An important application of photocatalysis is the purification of contaminants from water or air samples using the UV irradiation of nanocrystalline TiO_2 particles[14]. Electrically induced charge-transfer from the semi-conductor to the adsorbed species is termed heterogeneous electrocatalysis. Compared to other semi-conductors TiO_2 is favoured due to high photoactivity, being biologically and chemically inert, readily available, cheap to use, and also when in the form of nanoparticle films has a high surface area.

1.1.4 Electron transport through nanostructured semiconducting films

For mesoporous films the transfer of electrons between the separate nanoparticles is also an important process affecting the properties of the film. It has been found that electron transport through nanoparticle films is generally slower than in (compact) polycrystalline or monocrystalline materials. This has been discussed in terms of poor inter-particle electron transfer[15]. Electron transport in nanostructured semi-conductor films is assumed to proceed primarily via diffusion and many mechanisms have been proposed including the trapping/detrapping model, where electrons move between band gap states via the conduction band[16]. Alternatively a hopping model has been proposed, where the electrons move between localized band gap states[17]. Understanding the transport of electrons through these films is an important issue and has been the focus of much research[16], for example in the area of photovoltaic devices, where the transport of electrons through a TiO_2 matrix directly affects the device efficiency.

1.2 Self-Assembled Nanostructured Materials

1.2.1 Self Assembly

The term self-assembly implies the spontaneous absorption of molecules or nanoparticles in a mono-particle thick layer, onto a substrate. Self-assembled multilayer films are formed by the absorption of subsequent monolayers of molecules or nanoparticles[18].

The act of self-assembly of molecules has been known for over a century and can be traced conceptually to the molecular organisation of simple surfactants. In 1891 Agnes Pockel developed techniques for handling surfactant monolayers[19] but it was Irving Langmuir and Katherine Blodgett who demonstrated that compressed monolayers of surfactants could be transferred, layer-by-layer, onto solid substrates to form ultrathin stable films, now known as Langmuir-Blodgett films[20]. Development by Sagiv in the 1980's then led onto the construction of self-assembling monolayers (SAMs)[21], which obviate the need for surfactant compression in a Langmuir balance, but require strong chemical interactions to

anchor the functionalised surfactant to the substrate surface. Since that time the construction of monolayers and self –assembled films has extended to include larger molecules and supramolecular assemblies, incorporating Fullerenes, polyelectrolytes, polystyrene microspheres, silylated glass beads, and surfactant coated metallic, semi-conducting, magnetic and ferroelectric nanoparticles[22].

1.2.2 Electrostatic Layer-by-Layer Deposition

The main deposition technique used to prepare nanocomposite films in this thesis is the electrostatic layer-by-layer deposition method based on non-covalent interactions, first introduced by Decher in 1991[3]. This method has increased in popularity over the past decade due to the ease of film preparation, low cost, fast preparation time and high diversity of nanocomposites that can be produced. Unlike Langmuir-Blodgett films little specialist equipment is required, and unlike the preparation of SAMs formation relies solely on the electrostatic interactions of component parts.

The formation of multilayered structures is achieved simplistically from solutions of polyions or other charged molecular or colloidal particulates. The basis for the preparation of layer-by-layer nanocomposite films is shown schematically in figure 1.2 below. The layers are built up sequentially by immersing a substrate such as silicon or glass slides with a negatively charged surface into a positively charged nanoparticle solution (Step (i)). A rinsing step follows to remove any loosely bound material followed by immersion into the negatively charged ion solution (Step (ii)). Layers of ions can then be built up in a cyclic procedure that can either be carried out manually or by an automated device.

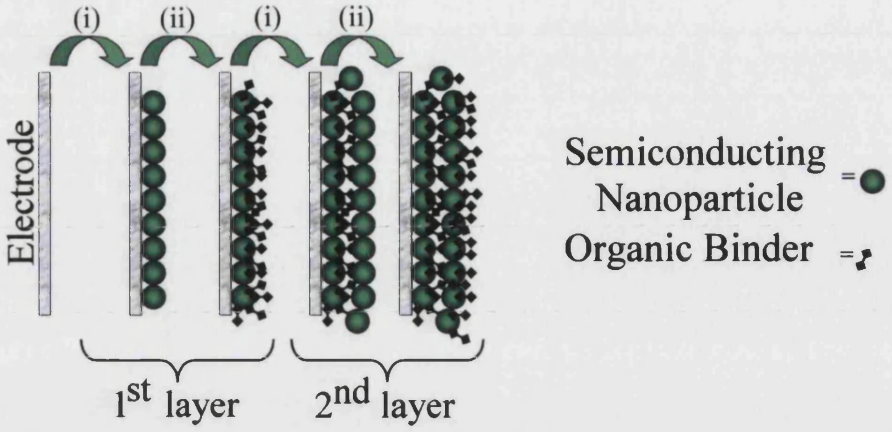

Figure 1.2 Layer-by-layer deposition process involving (i) immersion of substrate into the positively charged nanoparticle solution, followed by rinsing then (ii) immersion into the negatively charged ion solution.

Because the process only involves adsorption from solution in ordinary beakers there are, in principle, no restrictions with respect to substrate size and topology. Similarly there are no real restrictions on the type of ionic solution used as long as the principle of surface charge reversal is achieved so that another layer can be adsorbed on top. Typical adsorption times of charged molecules range from minutes in the case of polyelectrolytes to hours in the case of gold colloids[4]. Diversity in the structure, film morphology and surface properties of different multilayer films has been widely studied[18] and can be achieved by altering shielding and adsorption conditions. It has been shown that the electrostatic interactions between the ions in solution and the surface are key in determining the final structure of the film[23]. However secondary shorter range forces also play a role in determining the film thickness, final morphology, surface properties and even whether the films are stable. Secondary interactions include hydrophobicity, hydrogen bonding and dispersion forces in these systems.

1.3 Nanocomposite Thin Films as Substrates for Sensor Systems

Nanocomposite thin films deposited onto a conducting substrate are ideal for a wide range of analytical, sensor and catalytic applications due to their high surface area, porosity, inertness and diverse material composition. Already nanocomposite films

have been produced and their unique properties exploited for a wide range of applications[24].

Assembly of composites with an unlimited range of materials has included multilayer films incorporating enzymes with redox polymers or semiconducting particles. A sensor for hydrogen peroxide based on a horse radish peroxidase / TiO_2 composite utilises the high surface area and conductivity of the film[25]. Another widely studied sensor system for the detection of glucose in biological samples, incorporated glucose oxidase with a complimentary cationic redox-active polymeric species[26]. The breakdown of glucose into by-products is accompanied by a reduction/oxidation at the electrode which is monitored electrochemically. Sensors based on this system have been found to possess good time response and sensitivity.

The porosity of polyelectrolyte multilayer films has found applications as semi-permeable membranes, shown to be able to separate gases with relatively high selectivity. A poly(allyl amine)/ sulphonated polystyrene (PAH/SPS) membrane shows depressed permeability for O_2 and N_2 but H_2 permeates readily[27]. In solution Stanton et al[28] reported significant selectivity between Cl^-/SO_4^- in SPS/PAH films making these polyelectrolyte multilayer films interesting for water desalination and heavy metal ion separation techniques.

The electrostatic layer-by-layer assembly method, which allows a high level of control over film thickness and composition, has been applied to create a graded semiconductor composite film using various sizes of the highly luminescent CdTe nanoparticles[29]. Fine control over the composition of each layer meant that Kotov and co-workers could produce a composite whose particles displayed green, yellow, orange and red luminescence spectra respectively due to difference in particle size, which varied from 2nm (green) to 6nm (red).

Incorporating semi-conducting TiO_2 into nanocomposite films has found a wide range of applications including photocatalysis of organic pollutants as discussed in section 1.1.3. Another area for application of these films is the Dye-sensitized solar cell (DSSC), which uses a nanostructured TiO_2 film that has a light absorbing dye immobilised on to the surface. When illuminated the absorption of a photon by the

dye puts it into the excited state and an electron is injected from the dye into the TiO_2 film. The electron is transported through the film to a conducting substrate where the circuit is completed. The conductive properties of the TiO_2 film is therefore an important issue and much research has been carried out into the charge transport properties of these films[16]. More recently the inertness and high surface area of TiO_2 nanocomposites has been put to use for the study of fragile biological proteins, such as cytochrome *c*[30]. Probing these proteins using electrochemistry and under physiological conditions has allowed the study of these proteins and the important role they play during the respiratory cycle.

The above examples show just a small proportion of research carried out in the areas of nanocomposites, layer-by-layer assembly and semi-conducting particulate substrates. It was the aim of this project to expand and combine all of these properties into new nanocomposite film electrodes, the properties of which would be studied using a variety of techniques and tested as new and potentially useful substrates for sensory applications.

1.4 Voltammetric Techniques

Electrochemistry is the study of electron transfer reactions between electrodes and reactant molecules, whereby a species is either oxidised by loss of electrons to the electrode, or reduced by gain of electrons from the electrode. The diversity of electrode reactions that can be studied include electroactive species that are organic or inorganic, neutral or charged, a species in the electrolyte solution, a film on the electrode surface or even the electrode itself. Techniques used for the study of these reactions include linear sweep voltammetry, cyclic voltammetry and potential step voltammetry. There are many experimental set ups that can be used to carry out these measurements but the most commonly used is the three electrode cell. This involves placing the working electrode, reference electrode and counter electrode into a cell containing the redox system under investigation and an inert background electrolyte. The solution is purged of oxygen with either Argon or nitrogen and the experiment is controlled electronically using a potentiostat and personal computer.

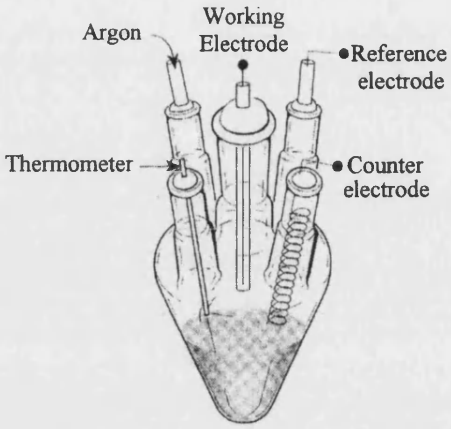

Figure 1.3 Schematic of a standard electrochemical cell.

1.4.1 Equilibrium Conditions

The simplest electrochemical measurement can be made when equilibrium is reached between a metallic electrode (m) and a redox active species in solution phase (aq). For a general one electron transfer process the following equation can be written:

$$O_{(aq)} + e^{-}{}_{(m)} \leftrightarrow R_{(aq)} \qquad (1.1)$$

Where the oxidised species O can be reduced at the electrode surface to the species R (or vice versa). As the reaction involves the transfer of an electron between two distinct phases and as the reaction moves towards equilibrium, a net charge separation occurs between the electrode and the solution. This charge separation creates a potential difference at the electrode/ solution interface.

The potential difference is fixed for a particular system providing no current is passed through the system and can be measured simply by placing into the solution a reference electrode and attaching it to the working electrode via a voltmeter. The potential difference is then measured relative to the standard reference electrode, which by convention has a potential difference of zero. Since no current is drawn through the cell, the equilibrium potential reached is dependent on the relative

concentrations of the species O and R. Nernst[31] showed that for a particular system the equilibrium potential, E_{eqm}, could be calculated from:

$$E_{eqm} = E^{\circ'} + \frac{RT}{nF}\ln\frac{[O]}{[R]} \qquad (1.2)$$

Where $E^{\circ'}$ is the standard electrode potential, R is the gas constant, T the temperature, n the moles of electrons, F the Faraday constant, and $[O]/[R]$ the concentration of the species at the electrode surface, which under equilibrium conditions is the same as the bulk.

1.4.2 Electrolysis

Electrochemical cells can be operated under conditions where a current flows and this is achieved by applying a potential that is different to E_{eqm}. The potential that must be applied to a system, above E_{eqm}, in order to make the electron transfer process favourable is called the overpotential, η. This overpotential induces the exchange of electrons between the electrode and molecules in solution. This can happen in either direction so that O is reduced to R:

$$O + e^- \rightarrow R \qquad (1.3)$$

Or so that R can be oxidised to O:

$$R \rightarrow O + e^- \qquad (1.4)$$

When electrolysis occurs, in addition to electron transfer at the electrode surface, ions must pass through the electrolyte solution between the cathode and anode (working and counter electrodes), and electrons through the wires externally connecting the electrodes. The current, i, passed through the external circuit is therefore a convenient measure of the rate of the cell reaction:

$$i = n A F j \qquad (1.5)$$

Where n = number of electrons, A = electrode area, F = Faraday constant, j = the flux of electroactive species reaching the electrode surface. Using Faraday's Law, the amount of charge, q, passed during a time period, t, can be used to indicate the total amount of chemical reaction that has taken place, to convert m moles of starting material, O, into product, R, involving the transfer of n electrons per molecule[32]:

$$q = \int_0^t i dt = mnF \qquad (1.6)$$

For every electrode reaction, in order to maintain a current, it is essential to supply reactant to the electrode surface, to remove product from the surface, as well as for electron transport to occur. The flux, j, from equation 1.5 relates to the concentration of the reactant at the electrode surface and also the heterogeneous rate constant, k_o, for the electrochemical reaction:

$$j = k_0[O]_0 \qquad (1.7)$$

Since the rate of reduction and hence current relies on all of these factors, the overall rate of reaction will be dependent on the slowest step. To understand the characteristics of an electrode reaction, we need to know about both electron transfer and mass transport.

1.4.3 Electron Transfer Kinetics

For the simple one electron transfer reaction:

$$O + e^- \underset{k_{ox}}{\overset{k_{red}}{\rightleftharpoons}} R \qquad (1.8)$$

Where electron transfer is the rate limiting factor, from equations 1.5 and 1.6 the current is given by:

$$i_c = FAk_{red}[O]_o \qquad (1.9)$$

$$i_a = F A k_{ox}[R]_o \qquad (1.10)$$

And the net current, i, is therefore:

$$i = F A (k_{ox}[R]_o - k_{red}[O]_o) \qquad (1.11)$$

At equilibrium (in the absence of any net current flow) the fluxes of material ($k_{red}[O]_o$ and $k_{ox}[R]_o$) to the electrode surface are balanced. Assuming electron transfer processes behave in a similar manner to chemical rate processes we can apply the transition state model, where O is reduced to R by overcoming an energy barrier:

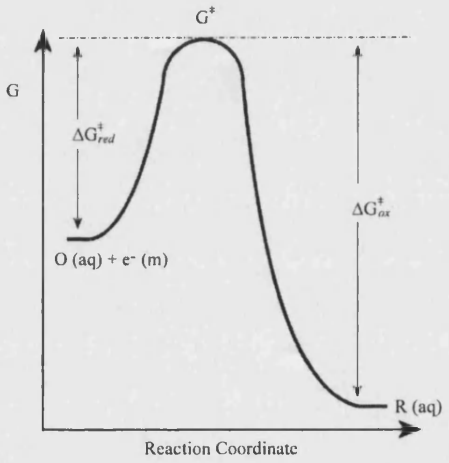

Figure 1.4. Free energy plot for a one electron reduction of $O_{(aq)}$[33].

Where electron transfer is the rate determining step, k_{red}, is predicted as:

$$k_{red} = A \exp\left(\frac{-\Delta G^{\ddagger}_{red}}{RT}\right) \qquad (1.12)$$

Where ΔG_{red} is the free energy of activation and A is a frequency factor to account for the number of collisions of the molecules with the electrode.

The application of transition state theory to electrode kinetics, based purely on classical concepts leads to the Butler-Volmer model of electrode kinetics. Widely

used in the electrochemical literature, it predicts how the observed current flowing at the working electrode varies as a function of the overpotential, η, and the transfer coefficient, α:

$$i = i_o\left(\frac{[R]_o}{[R]_{bulk}}\exp\left\{\frac{(1-\alpha)F\eta}{RT}\right\} - \frac{[O]_o}{[O]_{bulk}}\exp\left\{\frac{-\alpha F\eta}{RT}\right\}\right) \quad (1.13)$$

The first exponential term describes the anodic contribution to the current and the second term shows the cathodic contribution. The overpotential is the deviation from the equilibrium potential and the transfer coefficient reflects the transition state of the redox active species as it undergoes electron transfer. α can take a value between one and zero, depending on whether the transition state resembles either the product, R, or the reactant, O. For many reactions α is close to 0.5, suggesting that the transition state has intermediate properties.

If the solution under investigation is well stirred, the concentration of species at the surface will be the same as in the bulk and equation 1.13 can be simplified:

$$i = i_o\left(\exp\left\{\frac{(1-\alpha)F\eta}{RT}\right\} - \exp\left\{\frac{-\alpha F\eta}{RT}\right\}\right) \quad (1.14)$$

Where the standard exchange current, i_o, is proportional to the standard rate constant for the reaction:

$$i_o = FAk^o[R]^{\alpha}_{bulk}[O]^{1-\alpha}_{bulk} \quad (1.15)$$

The variation of the current with overpotential as predicted by the Butler-Volmer equation is shown below (figure 1.5). The solid curve shows the actual total current, which is the sum of the components i_c and i_a, shown as dashed traces. For larger negative overpotentials, the anodic component is negligible and the curve merges with that for i_c. For large positive overpotentials the curve merges with i_a. In going in either direction from E_{eqm}, the magnitude of the current rises rapidly because the

exponential factors dominate. However at high overpotentials the current levels off as it is limited by mass transfer rather than kinetics.

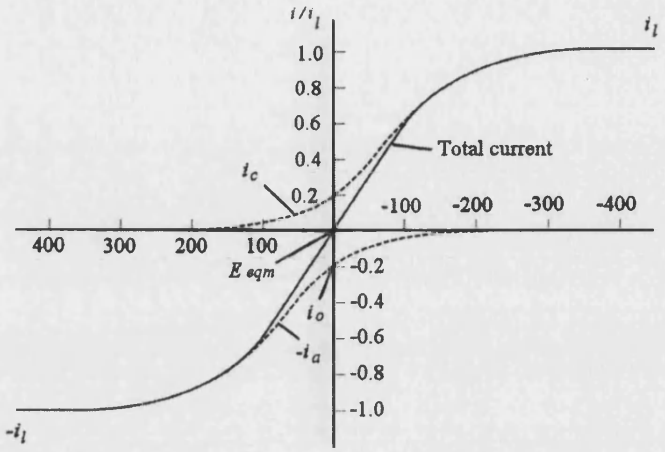

Figure 1.5 Plot showing the variation of current as a function of overpotential as predicted by the Butler-Volmer equation[31].

At low values of overpotential (close to E_{eqm}), both the anodic and cathodic current components are significant. However at high overpotential values, where the anodic reaction is driven, it is possible to omit the cathodic component from the Butler-Volmer equation to give:

$$\ln i = \ln i_o + \frac{(1-\alpha)F}{RT}\eta \quad (1.16)$$

Similarly, at negative overpotentials where the cathodic process is driven, it is possible to omit the anodic component:

$$\ln(-i) = \ln i_o - \frac{\alpha F}{RT}\eta \quad (1.17)$$

Equations 1.15 and 1.16 are known as the Tafel equations which are applied in plots of $\ln|i|$ vs. overpotential (figure 1.6). Analysis of the slope results in an estimate for the transfer coefficient and the extrapolated intercept of the y-axis gives an estimate for the standard exchange current.

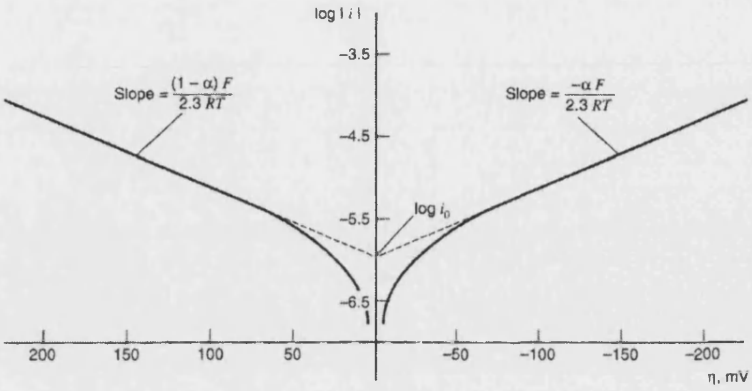

Figure 1.6 Tafel plot for the anodic and cathodic sections of a current-overpotential curve[31].

For overpotential values less than 10mV, close to E_{eqm}, the cathodic and anodic exponential terms in equation 1.14 can be written as Taylor expansions. Neglecting squared and higher terms results in equation 1.18, which shows a linear relationship between net current and overpotential in a narrow potential range close to E_{eqm}.

$$i = i_o \frac{nF}{RT}\eta \qquad (1.18)$$

1.4.4 Mass Transport

The simplest electrode reactions are those in which the rates of all associated chemical reactions are very rapid compared to those of mass transfer processes. Mass transfer is the movement of material from one location in solution to another and arises either from differences in electrical or chemical potential or from the movement of a volume element of solution. Modes of mass transport are:

- Migration – The movement of a charged species under the influence of an electric field.
- Diffusion – The movement of a species under the influence of a gradient of chemical potential (for example a concentration gradient).
- Convection – The movement of a species by stirring or hydrodynamic transport.

Electrochemical experiments are usually designed so that one or more of the contributions to mass transfer become negligible. Usually by adding a background electrolyte and performing experiments in unstirred solutions, contributions to mass transport come only from the diffusion of a species to the electrode surface.

Before the application of a potential to an electrochemical system the solution composition is constant, however during the course of a simple electron transfer process, a concentration gradient is induced at the electrode surface, forcing a flux of species O from the bulk solution. The diffusion of a species can be described by Fick's first law, which states that the flux, j, of species O, through a plane parallel to the electrode surface is given by:

$$j = -D_O \frac{\partial [O]}{\partial x} \qquad (1.19)$$

Where D_o is the diffusion coefficient and is characteristic of the diffusing species.

As the electrolysis reaction proceeds, a diffusion layer is established close to the electrode surface where $[O]_o$ does not equal $[O]_{bulk}$. Figure 1.7 illustrates how the diffusion layer thickness grows as electrolysis continues:

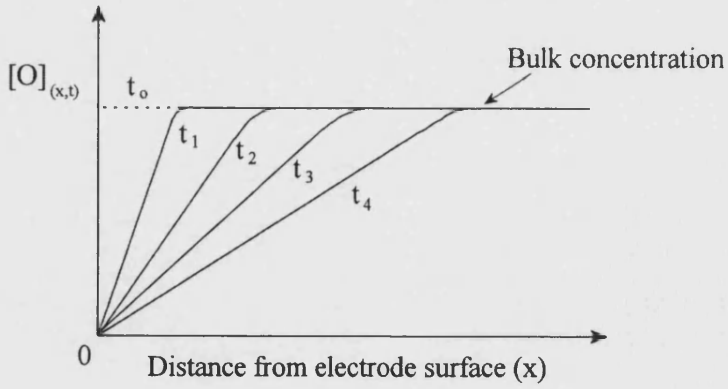

Figure 1.7 Diagram illustrating the growth of the diffusion layer thickness with time ($t_o \rightarrow t_4$)[33].

A degree of natural convection in the bulk of solution will limit the ability of the diffusion layer to expand and a constant or steady state is reached. Under steady state

conditions transport in the diffusion layer occurs by diffusion alone, whilst natural mixing will maintain $[O]_{bulk}$ outside the diffusion layer.

By combining Fick's first law of diffusion (equation 1.19) with Faraday's Law, the expression for the diffusion limited current is given by:

$$i_d = nFAD\left(\frac{\partial O}{\partial x}\right)_{x=0} \qquad (1.20)$$

Which shows the proportional relationship between current and concentration in voltammetry by equating the flux of O to the electrode surface with the flux of electrons.

1.4.5 Voltammetry

Linear sweep voltammetry and cyclic voltammetry are important tools in electrochemistry as they quickly and easily provide useful information about the system under investigation. The experiments are conducted usually in a three electrode cell in a stationary solution of electrolyte so that diffusion is the only method of transport for the active species to reach the electrode. Linear sweep voltammetry works simply by changing the potential of the working electrode from a set value of E_1 to E_2, usually from a situation where electron transfer does not occur to one where it is driven rapidly. As the change in potential is set over a specific time, then it is a measurement of the change in current over both a potential and time range. Cyclic voltammetry is an extension of linear sweep voltammetry so that once E_2 is reached, the direction of the sweep is reversed and the electrode potential scanned back to E_1.

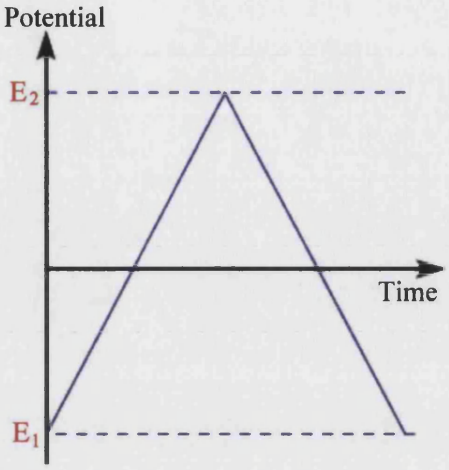

Figure 1.8 Variation of potential with time during a cyclic voltammetry experiment.

The basic shape of the current response for a cyclic voltammetry experiment is shown in figure 1.9.

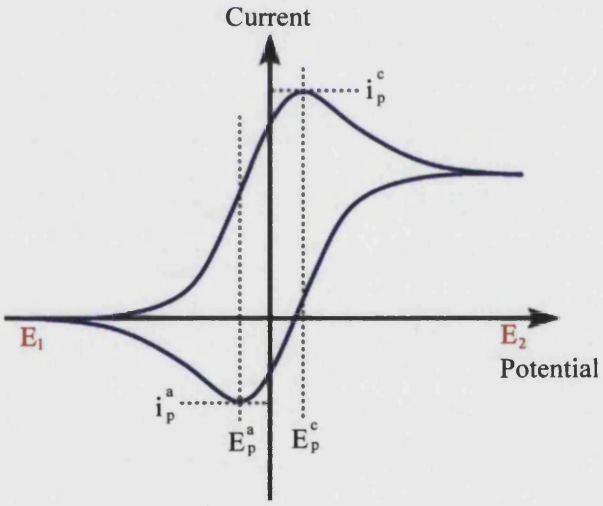

Figure 1.9 Basic cyclic voltammogram for reversible one electron reduction and oxidation[33].

At the start of the experiment the solution contains only the oxidised form of the redox couple *O* (see equation 1.3) and initially no current is passed since the potential applied is not great enough to induce electron transfer. As the redox potential for species *O* is reached, a current starts to pass which rises approximately exponentially with potential (time). As the species *O* is converted to *R* concentration gradients are set up for *O* and *R* and diffusion occurs down these gradients (see figure 1.7). At the peak current (i_p^c) the redox potential is sufficient to reduce any *O*

that reaches the electrode surface. After the peak current, the current detected is controlled by how much *O* can diffuse up to the electrode surface and so a fall in current is seen because as the experiment continues the depletion zone of *O* around the electrode becomes thicker and *O* has to diffuse further to reach the electrode.

Up to this point the voltammograms for linear sweep voltammetry and cyclic voltammetry will be identical, however for cyclic voltammetry we then reverse the direction of the potential sweep. Immediately after potential reversal, the oxidation current still flows even though the potential is now being swept in a negative direction. It is not until the potential is negative enough to reduce the species *R* back to species *O* that reduction currents are observed. After this point the current rapidly increases to the maximum peak current (i_p^a), after which the concentration of *R* is depleted at the electrode surface and the current once again decays due to diffusion control.

For a completely reversible system, the formal reduction potential, $E^{0'}$, is calculated from the cyclic voltammogram to be half way between the oxidation and reduction peak current potentials:

$$E^{0'} \approx \frac{E_p^c + E_p^a}{2} \qquad (1.21)$$

The separation between peak potentials (E_p^c and E_p^a) is determined by the number of electrons transferred in the electrode reaction (n) and for a reversible system is:

$$\Delta E_p = E_p^a - E_p^c = 57/n\ mV \text{ (at 298K)} \qquad (1.22)$$

Slow electron transfer (irreversibility) or uncompensated resistance (iR drop) will cause the separation (ΔE_p) to increase[31].

The values of i_p^a and i_p^c should also be identical for a reversible couple. Chemical irreversibility, in which a chemical reaction is coupled to the electrode process causes departures from unity for the ratio i_p^a / i_p^c.

In electrochemically reversible systems the electron transfer rates at all potentials are significantly greater than the rate of mass transport, and therefore Nernstian equilibrium is always maintained at the electrode surface. When the rate of electron transfer is insufficient to maintain this equilibrium then the shape of the voltammogram changes to that of an electrochemically irreversible system. The most marked feature of a cyclic voltammogram of a totally irreversible system is the total absence of a reverse peak. The terms 'reversible' and 'irreversible' refer to limiting cases according to whether the electrode kinetics are fast or slow relative to the mass transport conditions of the system of interest.

For planar diffusion the peak current for a reversible process may be calculated from the Randles-Sevčik equation[32]:

$$I_p = -(2.69\text{x}10^5)\, n^{3/2} c_o^{\infty} D^{1/2} v^{1/2} \text{ (at 298K)} \qquad (1.23)$$

Where I_p is the peak current density in A cm^{-2}, D is the diffusion coefficient in cm^2 s^{-1}, v is the scan rate in Vs^{-1}, n is the number of electrons transferred per molecule, and c_o^{∞} is the concentration of species O in bulk solution in mol cm^{-3}. Thus the peak current density for a reversible system is proportional to the concentration of electroactive species and to the square roots of scan rate and diffusion coefficient.

1.4.6 Cyclic Voltammetry at modified electrodes

Many of the electrodes investigated during this thesis contain an adsorbed redox species or are chemically modified, and as such the voltammetric characteristics for an immobilised redox species differ from those of diffusion controlled redox species. Figure 1.10 shows a typical cyclic voltammetric response for a reversible one electron transfer, where initially only species O is immobilised on the electrode surface:

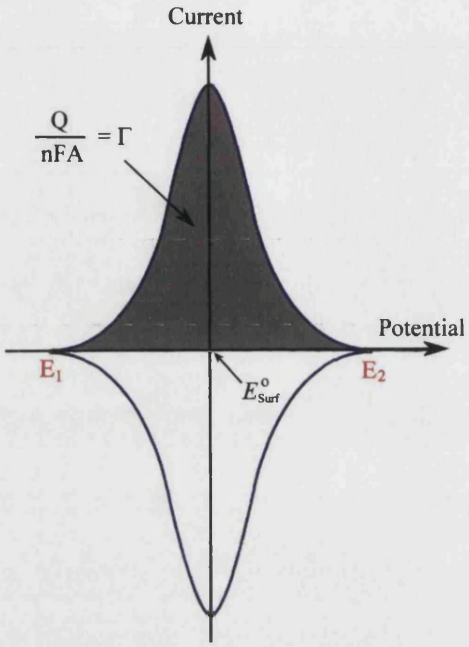

Figure 1.10 Schematic diagram showing a reversible cyclic voltammogram of an immobilised redox species, where E^{o}_{surf} is the reversible potential of the immobilised redox species[31].

In contrast to a voltammogram for a reaction in which both product and reactant are dissolved in solution, the peaks are sharp and symmetrical, the current rising exponentially from zero to a peak value and then falling back to zero, with little peak separation. The symmetrical peak arises because of the fixed amount of reactant available for reduction; only *O* immobilised on the electrode surface can be reduced. Since diffusion plays no role in the overall electrode process, for a reversible one electron transfer system, the analysis is straightforward. It can be shown that $E_p^{\,a} = E_p^{\,c}$ and that the peak current density, I_p, is given by:

$$I_p = \frac{n^2 F^2 \nu A \Gamma_{total}}{4RT} \qquad (1.24)$$

Where n is the number of electrons in the reaction, F is the Faraday constant, υ is the scan rate, A is the electrode area and Γ_{total} is the surface coverage in mol cm^{-2}.

The area under the cathodic peak corresponds to the charge associated with the reduction of the adsorbed layer of *O*, the integration of which gives the number of electrons transferred (and consequently the number of molecules adsorbed) and hence allows the direct calculation of the electrode coverage, where:

$$\frac{Area\ under\ peak}{v} = nFA\Gamma_{total} \qquad (1.25)$$

For non-Nernstian systems the shape of the voltammogram changes. For irreversible systems the forward peak ceases to be symmetric and there will be no reverse peak. For quasi-reversible reactions there will be a reverse peak but both peaks may be asymmetric and the peak potentials not coincident.

1.4.7 Electrochemical Impedance Spectroscopy (EIS)

Cyclic voltammetry and methods of studying electrode reactions by imposing potential sweeps, potential steps or current steps, typically drive the electrode to a condition far from equilibrium, where the observed response is usually a transient signal. Another approach is to perturb the cell with an alternating signal of small magnitude and to observe the way in which the system follows the perturbation at steady state. Initially this method was a way of measuring rate constants of reactions involving fast electron transfer, where the measurement was needed to be performed on a short timescale so that electrode kinetics rather than diffusion was the rate determining process. Now a whole range of ac techniques are employed in order to elucidate electrode reactions due to a) the ability to make high precision measurements (the indefinite steady state response can be averaged over a long time period), b) the response can be treated theoretically by simplification of linearised current-potential characteristics (see equation 1.18), c) measurements can be taken over a wide time (or frequency) range.

Electrochemical impedance spectroscopy (EIS) is a technique where the impedance of an electrochemical cell or electrode is measured and the data modelled using a theory that relies on the analogy between an electrochemical cell and networks of

resistors and capacitors that are thought to behave like the cell. Thus it is important to understand some of the basics of ac theory and electrical circuit terminology.

Electrical resistance is the ability of a circuit element to resist the flow of electrical current. Ohm's law defines resistance in terms of the ratio between voltage E and current I[31].

$$R \equiv \frac{E}{I} \qquad (1.26)$$

This relationship only applies to ideal resistors where:

- Ohms law is followed at all current and voltage levels
- Resistance is independent of frequency
- AC current and voltage signals through a resistor are in phase with each other

Non-ideal circuit elements exhibit much more complex behaviour than this so instead of resistance the concept of impedance is used. Impedance is also the ability of a circuit to resist the flow of electrical current but it is not limited by the above rules.

Electrochemical impedance is measured by applying an ac potential to an electrochemical cell and measuring the current through the cell. The measurement is usually performed at 'open circuit' potential so that no net current flows. When the ac signal is first impressed, a time dependent diffusion layer is created, but as no net current flows, a steady state is set up after a few cycles. The response to the applied ac potential will be an ac current. Usually electrical impedance is measured using a small excitation signal, to ensure that the cells response is linear (or pseudo-linear). For a linear system the current response to a sinusoidal potential will be a sinusoid at the same frequency but shifted in phase.

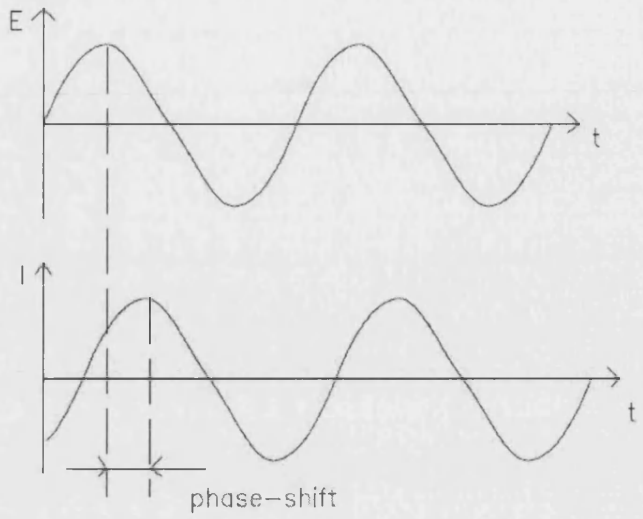

Figure 1.11 Diagram showing phase shift that occurs when an AC potential is applied to an electrochemical cell and an AC current is observed[34].

The excitation signal expressed as a function of time has the form:

$$E_t = E_o sin(\omega t) \qquad (1.27)$$

Where E_t is the potential at time t, E_o is the amplitude of the signal and ω is the radial frequency, which is related to frequency by:

$$\omega = 2\pi f \qquad (1.28)$$

In a linear system the response current I_t is shifted in phase ϕ and has a different amplitude I_o:

$$I_t = I_o \sin(\omega t + \phi) \qquad (1.29)$$

An expression analogous to Ohms law allows us to calculate the impedance, Z, as:

$$Z = \frac{E_t}{I_t} = \frac{E_o \sin(\omega t)}{I_o \sin(\omega t + \phi)} = Z_o \frac{\sin(\omega t)}{\sin(\omega t + \phi)} \qquad (1.30)$$

The impedance is therefore expressed in terms of Z_o and a phase shift ϕ. Impedance can be expressed graphically in the form of either of a Nyquist plot or a Bode plot

where the log of frequency is plotted on the x axis and the absolute values of impedance ($|Z| = Z_o$) and the phase shift on the y axis.

EIS data is commonly analysed by fitting to an equivalent electrical circuit model. Most of the circuit elements in the model are common electrical elements such as resistors, capacitors and inductors. Below is a table of the impedance of some standard circuit components[34]:

Table 1.1

Component	Current Vs Voltage	Impedance
Resistor	$E = iR$	$Z = R$
Inductor	$E = L\partial i / \partial t$	$Z = j\omega L$
Capacitor	$i = C\partial E / \partial t$	$Z = 1/j\omega C$

Very few electrochemical cells can be modelled using a single circuit element so EIS models usually consist of a number of elements in both serial and parallel combinations. When in series:

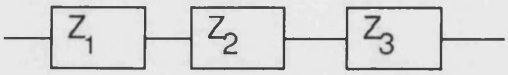

$$Z_{eq} = Z_1 + Z_2 + Z_3 \qquad (1.31)$$

When in parallel:

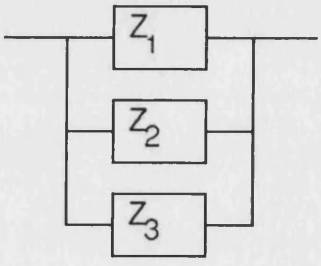

$$\frac{1}{Z_{eq}} = \frac{1}{Z_1 + Z_2 + Z_3} \qquad (1.32)$$

Some examples of common electrochemical components and their equivalent circuit elements are:

- Electrolyte resistor- where the electrolyte solution between the working electrode and reference electrode acts as a resistor.
- Double layer capacitance- where the electrical double layer on an interface between an electrode and the surrounding electrolyte acts as a capacitor.
- Polarisation resistance – when the potential of an electrode is forced away from its value at open circuit it becomes polarised and there is resistance.

Many common equivalent circuit models used to interpret simple EIS data are now included in the analysis package that comes with the EIS software. The analyst then has to find the model that best fits the data. Some prior knowledge of the nature of the electrochemical system is therefore useful and the fit will give quantitative data on the different elements of the system studied. A frequently used equivalent circuit is called the *Randles equivalent circuit*[31]:

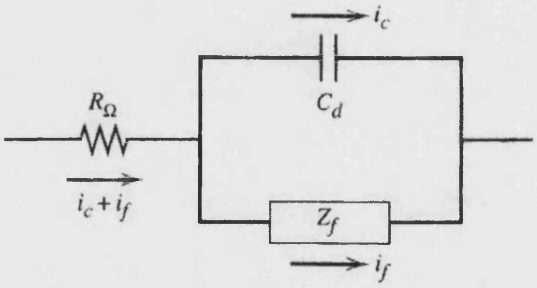

Where the solution resistance, R_Ω, is inserted as a series element (all the current must pass through this) and the double layer capacitance, C_d, and the general impedance of the faradic electron transfer process, Z_f, are in parallel. Here the parallel elements are introduced because the total current through the working interface is the sum of contributions from the faradic process, i_f, and the double layer charging, i_c.

1.4.8 Large-Amplitude AC Voltammetry

In ac voltammetry experiments, a three-electrode cell is used in the conventional manner, with a single sine wave of amplitude ΔE and frequency ω superimposed onto the potential so that:

$$E_t = E_{dc} + \Delta E sin(\omega t) \qquad (1.33)$$

As with cyclic voltammetry the potential is then swept between two points and the resulting current measured over time (potential). Commonly, as with impedance spectroscopy, only a small amplitude sine wave of maximum 5mV peak to peak is superimposed. This allows a simplification of the treatment for the resulting data (see section 1.4.3 and equation 1.18). By uncoupling the long term diffusion due to E_{dc} from the rapid diffusional fluctuations due to E_{ac}, the diffusion layer concentrations look like bulk values to the ac perturbation due to differences in the time scale. The current-overpotential relation is therefore virtually linear at low overpotentials and a simple model of electron transfer mechanisms can be applied (Butler-Volmer model of electrode kinetics).

In a linear system, excitation by a frequency ω, provides a current also of a frequency ω (and only of a frequency ω). When a perturbation larger than 5mV peak-to-peak is imposed on the E_{dc}, the system is no longer linear and the current-overpotential relation gives a distorted response that is not purely sinusoidal; but it is still periodic and contains a dc contribution as well as a supposition (Fourier synthesis) of signals at fundamental (at ω), second (at 2 ω), and higher harmonics[31]. These second order terms are exceptionally information rich as well as providing superior faradaic-to-background current ratios[35].

Large amplitude ac voltammetry is implemented by superimposing a periodic ac waveform of any amplitude onto a linear or triangular voltage. The dc potential is then swept at a constant rate and the data collected on a pc. Analysis of the data using the Fourier transform - inverse Fourier transform method enables the dc and ac components to be separated (see figure 1.12).

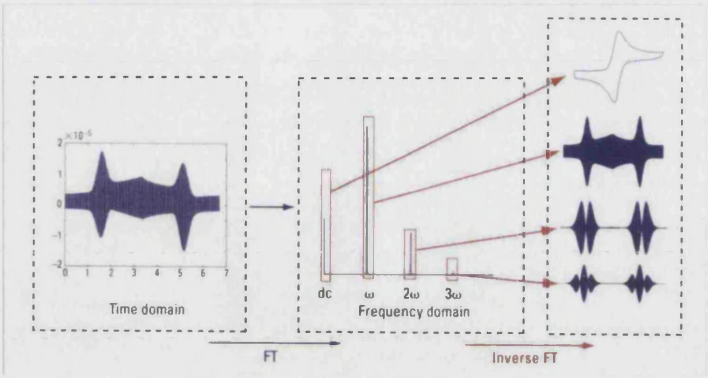

Figure 1.12 Schematic of FT-inverse FT data analysis. A) Time and B) frequency representations of data collected during an experiment. C) The separated dc and ac components represented in the time domain[35].

Once separated identification of intuitively obvious patterns of behaviour in the dc, fundamental and higher harmonic terms enables the estimation of E_o, R_u, C_{dl}, k_o and α in the following way, when data for two concentrations of reduced species is collected:

a) E_o from the dc cyclic component as R_u and k_o effects are minimised
b) C_{dl} from the fundamental harmonic because it has a high capacitance to faradaic current ratio
c) R_u, k_o, because the C_{dl} effect is minimised.

Methods of refining estimates are then implemented by computer simulation of results.

1.5 Surface and Structural Characterisation Techniques

1.5.1 Scanning Electron Microscopy (SEM)

Scanning Electron Microscopy (SEM) is a technique used to study the surface topology of a wide variety of samples. The technique has grown in popularity due to its ability to image samples in the 10nm range, allowing typically 1000 times more magnification than the best optical microscope[36]. Figure 1.13 shows a schematic of a typical SEM:

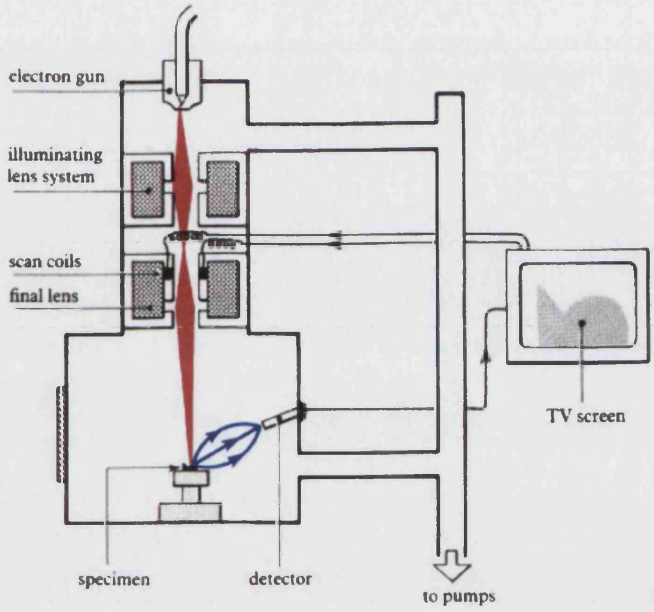

Figure 1.13 Schematic of a typical SEM

High energy electrons, typically 10KeV are produced at the electron gun. This is usually a tungsten filament and a large current is passed through it in order to heat the filament to the thermionic emission temperature of electrons (around 2700K). In a Field Emission Gun (FEGSEM) the tungsten filament is replaced by a single crystal tungsten wire sharpened to a point by electrolytic etching. The electrons are emitted by the FEG through a tunnelling effect[37], where a high electric field around the sharp tip sucks electrons out of the cathode, tunnelling them below the potential barrier. The FEG cathode in contrast to the tungsten filament is at room temperature and must be kept very clean by being kept under high vacuum.

Once the electrons are emitted they are accelerated towards the sample and focused into a minute beam that can be moved to any position on the sample. This is achieved by series of scan coils which carry the controlling current. They are held more positive than the electron gun and attract the electrons away from the filament. By changing the controlling current the electron beam can be controlled, allowing it to be moved to different parts of the sample.

When the electrons hit the sample surface there are several consequences that may occur[38]. The electrons may be elastically scattered from the sample with no energy

loss. The electrons may be absorbed by the sample and cause secondary, lower energy electrons to be emitted as well as X-rays. The electrons may be absorbed by the sample and give rise to the emission of visible light, known as cathodoluminescence, or cause electric currents within the sample. All of these effects can be used to gain information on the sample, but it is the secondary electrons that are used to produce an image of the sample. This is achieved by selectively attracting the lower energy electrons to a grid held at a low positive potential. Behind the grid is a disk covered in a scintillant which when struck by the electrons emit light. This is picked up by a photomultiplier tube and the image displayed in a TV screen. An image of the sample is built up by scanning the electron beam across the sample in exact synchrony with the scan to build up the image on the TV screen. The SEM does not contain lenses to magnify the image as in an optical microscope. Instead magnification results from the ratio of the area scanned to the area of the TV screen. Additional information can be gained from the sample by adding detectors to capture for example, the X-rays emitted from the sample which yields elemental information on the sample. A wide variety of samples can be imaged using the technique, although the nature of bombarding a sample with electrons means that it must be able to withstand conditions under high vacuum. Electrical conductivity is also needed in order to prevent artefacts caused by charging, although this can be suppressed by evaporating a thin conductive layer onto the sample.

1.5.2 Atomic Force Microscopy (AFM)

Atomic Force Microscopy (AFM) is a technique that allows the imaging of surfaces in atomic resolution, as well as measuring surface forces down to nano-Newton scales. Applications include the investigation of topologies of thin films, ceramics, composites, synthetic and biological membranes as well as investigating phenomena such as abrasion, adhesion, cleaning, corrosion and etching[34]. The first AFM was made by Binnig and Gerber in 1985 by gluing a shard of diamond onto gold foil and fixing it to a cantilever. The force between the tip and sample was measured by tracking the deflection of the cantilever, and features as small as 300Å could be detected.

Today the tips used are typically made from Si_3N_4 or Si but the principle is the same. An atomically sharp tip is scanned over a surface with feed back mechanisms to a computer that allow the tip to maintain either a constant force with the surface (to gain height information) or to maintain a constant height from the surface (to obtain force information). Figure 1.14 shows a schematic of a typical AFM:

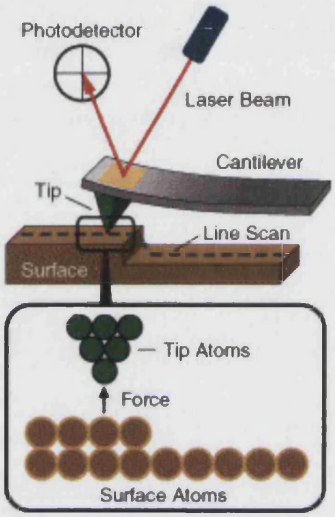

Figure 1.14 Schematic of a typical AFM

The AFM head is attached to the underside of a reflective cantilever, which has a diode laser focused onto it. As the tip scans the surface the cantilever moves up and down with the contour of the surface. This in turn moves the position of the laser beam which is picked up by a photodetector. Three dimensional topographical maps of the surface are then constructed by plotting local surface height versus the probe tip position. The primary purpose of the AFM is to quantitatively measure the surface roughness and this can be achieved with a 5nm lateral and 0.1nm vertical resolution.

1.5.3 The Quartz Crystal Microbalance (QCM)

The quartz crystal microbalance is a sensitive tool capable of detecting miniscule changes in weight on the nano-gram range. It can detect changes in mass equivalent to just a single monolayer of atoms and is around 100 times more sensitive than the best electronic fine balances[39]. The QCM measures mass by measuring a change in

frequency of a piezoelectric quartz crystal, when it is disturbed by the addition of a small mass.

The piezoelectric effect was first discovered by Pierre and Marie Curie[39], who in 1880 showed that when mechanical stress is applied to the surface of an acentric material (like rochelle salt, tourmaline or quartz which crystallize into non-centrosymmetric space groups), a corresponding electrical potential arises across the crystal, whose magnitude is proportional to the applied stress. This effect appears since a single crystal of an acentric material possesses a polar axis due to the dipoles associated with the arrangement of atoms in the crystalline lattice. Under mechanical stress, physical displacement of the atoms occur, so that a corresponding change in the net dipole moment takes place and as a result charge is generated in the crystal (see figure 1.15).

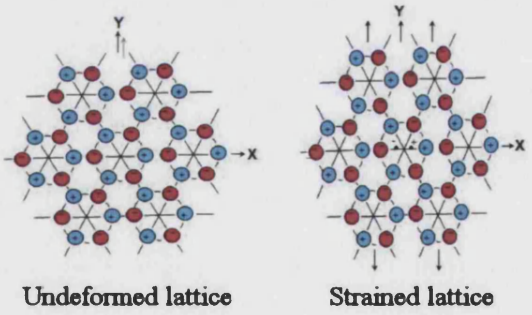

Figure 1.15 When a force deforms the lattice, the centre of gravity of the positive and negative charges in the crystal can be separated so as to produce surface charges.

Shortly after this discovery, the converse piezoelectric effect was experimentally verified, where the application of a voltage across the crystal gave a corresponding mechanical strain. The converse piezoelectric effect is the basis for the methodology behind the QCM.

Many types of crystals exhibit the piezoelectric effect, but the electrical, mechanical and chemical properties of quartz make it the most commonly used in analytical applications. The quartz plates (also known as wafers or blanks) are fabricated at a

precise orientation with respect to the crystallographic axes of the quartz material, which has important implications for the frequency-temperature characteristics of the resonator. The piezoelectric quartz crystal is sandwiched between a pair of (usually gold) electrodes, which are deposited by thermal evaporation (see figure 1.16).

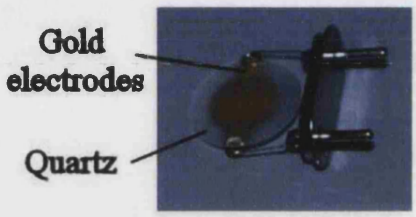

Figure 1.16 A quartz crystal resonator with gold electrode contacts

An alternating current is applied to the electrodes creating an alternating electric field across the crystal, which distorts the crystal lattice due to the piezoelectric effect. This mechanical oscillation of the quartz crystal results in a standing shear wave across the bulk of the quartz disk at a characteristic vibrational frequency (ie the crystals natural resonant frequency)(see figure 1.17).

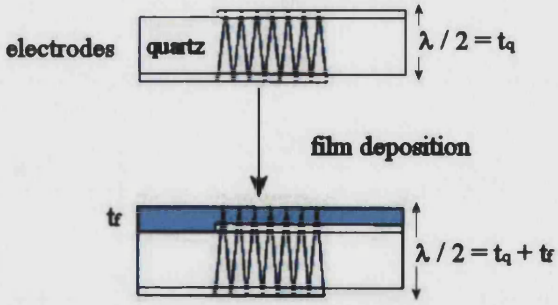

Figure 1.17 Schematic representation of a transverse shear wave in a quartz crystal resonator before and after film deposition. The acoustic wavelength is longer after film deposition due to the greater thickness, resulting in a lower resonant frequency[40].

If a rigid layer is evenly deposited on one or both of the electrodes the resonant frequency will decrease proportionally to the mass of the adsorbed layer according to the Sauerbray equation[41]:

$$\Delta F = \frac{-2f_o^2 \Delta m}{A\sqrt{\mu_q \rho_q}} = -c\Delta m \qquad (1.34)$$

Where ΔF = measured frequency shift in Hz, f_o^2 = the fundamental resonant frequency (squared) in Hz, Δm = mass change in g, A = piezoelectrically active area in cm^2, μ_q = shear modulus of quartz = 2.947 x 10^{11} g cm^{-2}, ρ_q = density of quartz = 2.648 g cm^{-3}, c = mass sensitivity constant (based on type of crystal used).

The Sauerbray equation is only strictly applicable to uniform, rigid, thin film deposits and as such QCM was for a while regarded as a gas phase detector. However work by Kanazawa et al[42] showed that the change in resonant frequency upon immersion into a liquid phase could be expressed approximately by:

$$\Delta F_{gas \rightarrow liquid} = -c_1\left(c_2\sqrt{\rho_{liquid}\eta_{liquid}} + h\rho_{liquid}\right) \qquad (1.35)$$

Where the frequency change $\Delta F_{gas \rightarrow liquid}$ is related to the density of the liquid ρ_{liquid}, the viscosity of the liquid η_{liquid}, the topographic factor h (related to the pore height), and frequency dependant sensitivity factors c_1 and c_2. This extension of measurements to liquid media has increased the uses of QCM for monitoring real-time mass changes to areas including thin film thickness monitoring[6], electrochemistry of interfacial processes at electrode surfaces, and the detection and monitoring of biological species such as virus', cells and proteins at electrode surfaces.

1.5.4 Simultaneous small-angle X-ray scattering and wide-angle X-ray scattering (SAXS/WAXS)

SAXS/WAXS or simultaneous small-angle X-ray scattering and wide-angle X-ray scattering is a technique where the elastic scattering of X-rays by a sample is recorded at both low angles (typically between 0.1° and 10°) and wide angles (up to 40°). In the small angular range, SAXS is capable of delivering information about the shape and size of macromolecules (between 5 and 25nm) and characteristic distances of partially ordered materials (up to 150nm) and pore sizes. SAXS is used

for the determination of the microscale or nanoscale structure of particle systems in terms of such parameters as averaged particle sizes, shapes, distribution, and surface-to-volume ratio. SAXS has been applied to a large number of areas including colloids, metals, polymers, proteins and pharmaceuticals. Wide-angle X-ray scattering (WAXS) is often used to determine the crystalline structure of polymers, where the diffraction pattern generated allows the calculation of the chemical or phase composition, texture, and crystallite size. WAXS is the same technique as SAXS only the distance from sample to the detector is shorter and thus diffraction maxima at larger angles are observed.

In SAXS/WAXS a monochromatic X-ray is emitted from an X-ray generator which then passes through a small beam shaping device before passing through the sample (see figure 1.18). Behind the sample the detector measures the elastically scattered X-rays with respect to the angle θ.

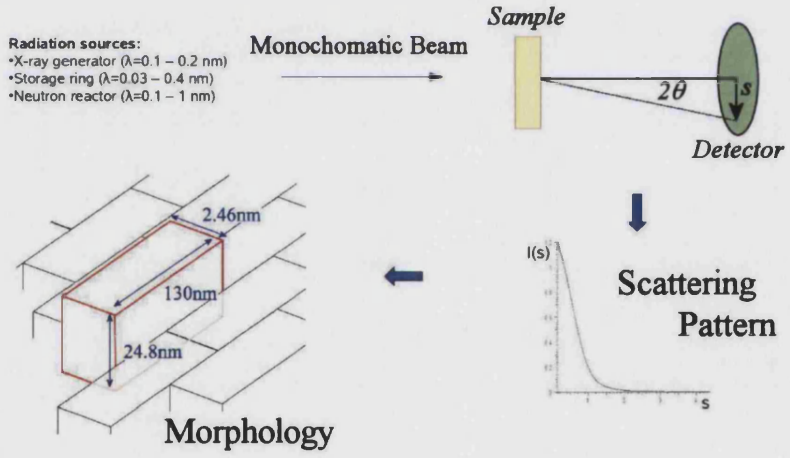

Figure 1.18 Schematic of SAXS/WAXS apparatus and data processing[43]

Data from SAXS/WAXS is interpreted using Bragg's Law, a relationship derived from the diffraction of X-rays as they pass through a crystalline solid. In 1913 William Lawrence Bragg and William Henry Bragg found that intense peaks of reflected radiation (known as Bragg peaks) are produced when X-rays of a certain specific wavelength and incident angle are passed through a crystalline solid. Bragg explained this result by modeling a crystal as a set of discrete parallel planes separated by a constant parameter, d. It was proposed that the incident X-ray

radiation would produce a Bragg peak if the reflection off the various planes interfered constructively. This gives the formula for Braggs law as[44]:

$$n\lambda = 2d\sin\theta \qquad (1.36)$$

Where n is an integer, λ is the wavelength of X-rays, d is the spacing between the planes, *and* θ is the angle between the incident X-ray and the scattering planes. Waves which satisfy this condition interfere constructively and result in a reflected wave of significant intensity.

In SAXS/WAXS measurements the position sensitive detector placed behind the sample measures the scattered intensity, usually in 2-dimensions. For a highly ordered sample a series of Debye rings are produced, which result from the constructive interference of X-rays. Most SAXS data however is much less straightforward and appears as a continuous function of scattering angle. For analysis, this 2-dimensional profile is reduced to a set of intensity versus angle data, using the description of Braggs law in reciprocal space, where the simple relationship between diffraction angle and Q-space is[45]:

$$Q = \frac{4\pi\sin\theta}{\lambda} \qquad (1.37)$$

Data is then interpreted by computer modeling to one of the many idealised systems developed over the years.

1.6 References

[1] K. Rajeshwar, N. R. de Tacconi and C. R. Chenthamarakshan, *Chem. Mater.*, 2001, **13**, 2765-2782.

[2] E. Roduner, *Chem. Soc. Rev.*, 2006, **35**, 583-592.

[3] G. Decher and J. D. Hong, *Makromol. Chem., Macromol. Symp.*, 1991, **46**, 321-327.

[4] G. Decher, *Science*, 1997, **277**, 1232-1237.

[5] G. Decher, M. Eckle, J. Schmitt and B. Struth, *Curr. Opin. Colloid Interface Sci.*, 1998, **3**, 32-39.

[6] K. J. McKenzie, F. Marken, X. Gao, S. C. Tsang and K. Y. Tam, *Electrochem. Commun.*, 2003, **5**, 286-291.

[7] K. J. McKenzie, P. M. King, F. Marken, C. E. Gardner and J. V. Macpherson, *J. Electroanal. Chem.*, 2005, **579**, 267-275.

[8] C. G. Siontorou and D. P. Nikolelis, *Analytica Chimica Acta*, 1997, **355**, 227-234.

[9] A. Bard, *Integrated Chemical Systems*, Wiley, New York, 1994.

[10] X. Ji, J. Zuppero, J. Gidwani and G. Somorjai, *Nano Lett.*, 2005, **5**, 753-756.

[11] W. T. Liu, *J. Biosci. Bioeng.*, 2006, **102**, 1-7.

[12] S. Roy Morrison, *Electrochemistry at Semiconductor and Oxidized Metal Electrodes*, Plenum Press, New York, 1980.

[13] A. L. Linsebigler, G. Q. Lu and J. T. Yates, *Chem. Rev.*, 1995, **95**, 735-758.

[14] B. Huber, A. Brodyanski, M. Scheib, A. Orendorz, C. Ziegler and H. Gnaser, *Thin Solid Films*, 2005, **472**, 114-124.

[15] E. A. Meulenkamp, *J. Phys. Chem. B*, 1999, **103**, 7831-7838.

[16] H. G. Agrell, G. Boschloo and A. Hagfeldt, *J. Phys. Chem. B*, 2004, **108**, 12388-12396.

[17] J. Bisquert, D. Cahen, G. Hodes, S. Ruhle and A. Zaban, *J. Phys. Chem. B*, 2004, **108**, 8106-8118.

[18] J. H. Fendler, *Chem. Mater.*, 1996, **8**, 1616-1624.

[19] A. Pockels, *Nature*, 1891, **43**, 437.

[20] K. Blodgett, *J. Am. Chem. Soc.*, 1934, **56**, 495.

[21] J. Sagiv, *J. Am. Chem. Soc.*, 1980, **102**, 92-98.

[22] F. C. Meldrum, Fendler, J.H., *Biomimetric Materials Chemistry*, VCH: New York, 1996.

[23] P. T. Hammond, *Curr. Opin. Colloid Interface Sci.*, 1999, **4**, 430-442.

[24] P. T. Hammond, *Adv. Mater.*, 2004, **16**, 1271-1293.

[25] Y. Zhang, P. L. He and N. F. Hu, *Electrochim. Acta*, 2004, **49**, 1981-1988.

[26] E. S. Forzani, M. Otero, M. A. Perez, M. L. Teijelo and E. J. Calvo, *Langmuir*, 2002, **18**, 4020-4029.

[27] J. M. Levasalmi and T. J. McCarthy, *Macromolecules*, 1997, **30**, 1752-1757.

[28] B. W. Stanton, J. J. Harris, M. D. Miller and M. L. Bruening, *Langmuir*, 2003, **19**, 7038-7042.

[29] A. A. Mamedov, A. Belov, M. Giersig, N. N. Mamedova and N. A. Kotov, *J. Am. Chem. Soc.*, 2001, **123**, 7738-7739.

[30] K. J. McKenzie and F. Marken, *Langmuir*, 2003, **19**, 4327-4331.

[31] A. J. Bard and L. R. Faulkner, *Electrochemical Methods: Fundamentals and Applications*, Wiley, New york, 1980.

[32] Southampton Electrochemistry Group, *Instrumental Methods in Electrochemistry*, Horwood Publishing, Chichester, 1985.

[33] A. C. Fisher, *Electrode Dynamics*, Oxford University Press, Oxford, 1996.

[34] H. Li, *www.chembio.uoguelph.ca/educmat/chm729/afm/introdn.htm*, 1997.

[35] A. M. Bond, N. W. Duffy, S. X. Guo, J. Zhang and D. Elton, *Anal. Chem.*, 2005, **77**, 186A-195A.

[36] A. R. Sampson, *Scanning Electron Microscopy*, website: www.sem.com/analytic/sem.htm, 1996.

[37] J. L. Labar, *www.mfa.kfki.hu/~labar/Introduction.pdf*, EMAS-2002, Szczyrk (Poland).

[38] P. Perkes, *URL: http://acept.la.asu.edu/PiN/rdg/elmicr/elmicr.shtml*, 1999.

[39] www.pharamaceutical-int.com/categories/qcm-technology/quartz-crystal-microbalance, Editon edn.

[40] D. A. Buttry and M. D. Ward, *Chem. Rev.*, 1992, **92**, 1355-1379.

[41] G. Sauerbrey, *Z. Phys.*, 1959, **155**, 206.

[42] K. K. Kanazawa and J. G. Gordon, *Anal. Chem.*, 1985, **57**, 1770-1771.

[43] M. Singh, in *www.physics.queensu.ca/~marsha/SAXSoverview.html*, Editon edn., 2002.

[44] O. Glatter and O. Kratky, *Small Angle X-ray Scattering* Academic Press, London, 1982.

[45]O. Glatter and O. Kratky, in *Small Angle X-ray Scattering*, Academic Press, London, Editon edn., 1982, p. 105.

2. Deposition and Characterisation of TiO_2 Nanoparticle Films

2.1 Introduction

TiO_2 forms the structural basis of the nanocomposite films studied in this thesis. The layer-by-layer deposition process builds up a highly porous film of TiO_2 particles with organic binder molecules acting as spacers. TiO_2 as a semiconductor can itself undergo electrochemical oxidation and reduction on a suitable conducting electrode. Before adsorption of complex organic redox systems into the TiO_2 films, it is therefore important to understand the properties of the TiO_2 singularly, as a nanoparticulate mono-layer, and also as a mesoporous film. The electrochemical properties of TiO_2 have been studied extensively usually in the form of thin meso- or microporous films at inert electrodes[1], at titanium surfaces[2] and also in the form of single crystals[3]. Recent work has included the study of TiO_2 nanoparticles formed into a monolayer on an inert boron doped diamond substrate[4], with results that showed features similar to those of polyoxometalate redox systems with surface site reduction of the Ti(IV) to Ti(III) followed by protonation. Boron-doped diamond is an ideal substrate for the study of TiO_2 due to its inert nature, wide accessible potential window and its low background current[5].

In this thesis two sizes of TiO_2 nanoparticles are used to prepare films: 6nm and 40nm in diameter. Due to differences in the dispersion of the particles into solution, the method used to form the 40nm particles films is modified and consequently the properties of the films made with these particles differ from those prepared with the 6nm particles. In this chapter both monolayer and multilayer films are studied on boron-doped diamond and ITO substrates and characterised electrochemically, using FEGSEM, AFM and impedance spectroscopy. Films prepared with 6nm diameter TiO_2 particles and phytate binder form a homogenous and highly porous composite on ITO. In contrast films prepared from the 40nm diameter TiO_2 particles form larger aggregates on the ITO substrate which on the microscopic scale do not completely cover the substrate. Both types of film however are homogenous with pores capable of immobilising redox active species.

2.2 Experimental

2.2.1 Chemical Reagents

TiO_2 nanoparticle sol (ca. 6nm diameter, anatase, 30-35% in aqueous HNO_3, pH 0-1, TKS-202) was obtained from Tayca Corp, Japan and diluted to a 3 %wt solution with deionised water. A suspension of 40nm TiO_2 nanoparticles was prepared from powder form (AMT-600, also Tayca Corp, Japan) in a 3%wt methanol solution by sonication (20 kHz Fisherbrand ultrasonic bath) for 30 minutes.

Phytic acid (*myo*-insitolhexakis(dihydrogen phosphate) dodecasoduim salt hydrate), 1,2,4,5-Benezenetetracarboxylic acid or pyromellitic acid (96%), perchloric acid (70% A.C.S reagent), $NaClO_4$, NaOH, H_3PO_4 (all Aldrich), methanol and ethanol (Fisher Scientific, HPLC grade) were obtained commercially and used without further purification. All solutions were prepared using deionised water with a resistivity of not less than 15 MΩ cm.

2.2.2 Instrumentation

Electrochemical experiments were conducted with a PGSTAT 30 Autolab system (Eco Chemie, Netherlands), controlled by a personal computer running the GPES software version 4.9. A conventional three-compartment electrochemical cell was used for cyclic voltammetry experiments, with a platinum gauze counter electrode of approximately $2cm^2$ area. The reference electrode was a saturated calomel electrode (SCE, Radiometer, Copenhagen). The potential of the SCE compared to the standard hydrogen electrode (SHE) is 0.242 V. Prior to conducting experiments the aqueous electrolyte solution was thoroughly de-aerated with argon (Pureshield, BOC). Experiments were conducted at 22 ± 2°C.

Electrochemical Impedance Spectroscopy measurements were made using a Solartron Analytical (Slough, Berkshire) SI 1260 impedance/ gain phase analyzer coupled with a SI 1287 electrochemical interface. The set up included using a standard three electrochemical cell, with a platinum gauze counter electrode and calomel reference electrode.

For Field Emission Gun Scanning Electron Microscopy (FEGSEM), a Leo 1530 system was used. Samples were prepared by scratching (to reveal a film cross section) and gold sputter coating prior to analysis.

Working electrodes were predominantly tin-doped indium oxide (ITO) coated glass (10mm x 60mm, resistivity 15 Ω^{-1}) obtained from Image Optics Components Ltd. The ITO electrodes are cleaned by washing with ethanol and water and then dried by a 30 minute heat treatment at 500°C in air (Elite tube furnace). After film deposition the surface area of the ITO was limited to approximately 1cm^2 using a silicon adhesive sealant (Silicoset 151, Ambersil). Contact between the ITO glass and the working electrode was improved by using copper tape. Other working electrodes included polycrystalline boron-doped diamond with a mirror finish polish (mineral acid treated, doping level ca. 10^{20} cm^{-3}, Windsor Scientific, Slough, UK), obtained in the form of plates (5mm × 5mm × 0.6mm) for electrochemical experiments (mounted with silver epoxy back contact in epoxy) and in the form of 3 mm diameter disks (for SEM imaging experiments). Gold, glassy carbon and platinum disk working electrodes were obtained from BAS (UK). Boron-doped diamond, gold and platinum disk electrodes were thoroughly cleaned between each deposition by polishing on a polishing pad (Buehler) with polycrystalline diamond suspension (1F μm metadi supreme, Buehler), rinsed and then polished on another polishing pad with distilled water.

2.2.3 Film Deposition Procedures

Directed assembly of multilayer films

The nanocomposite films investigated during this thesis were prepared using the layer-by-layer deposition strategy (see chapter section 1.2.1). Typically this consisted of six steps involving: (i) dip into a solution of nanoparticles for 1 min, eg 3%wt 6nm TiO_2 in H_2O, (ii) dip for 30s deionised water, (iii) dip for 30s deionised water, (iv) dip into 'binder' solution for 1 min, eg. 40 mM phytic acid, (v) dip for 30s deionised water, (vi) dip for 30s deionised water.

In order to improve reproducibility, the layer-by-layer dipping process was undertaken using a robotic dip coater (DSG Dip Carousel, Nima Technology, Coventry, UK). The dip-coater was controlled using a personal computer and run using Nima 524DC software. The dip-coater was programmed to prepare films of varied thickness by carrying out a preset number of dipping cycles. Each cycle consisted of six steps which consisted typically of (i) dip into a solution of nanoparticles for 1 min, eg. 3%wt 6nm TiO_2 in H_2O, (ii) dip for 30s deionised water, (iii) dip for 30s deionised water, (iv) dip into 'binder' solution for 1 min, eg 40 mM phytic acid, (v) dip for 30s deionised water, (vi) dip for 30s deionised water. The dipping speed for the robotic arm was preset to 70 mm/min and each solution pot contained a stirrer bar rotating at constant speed.

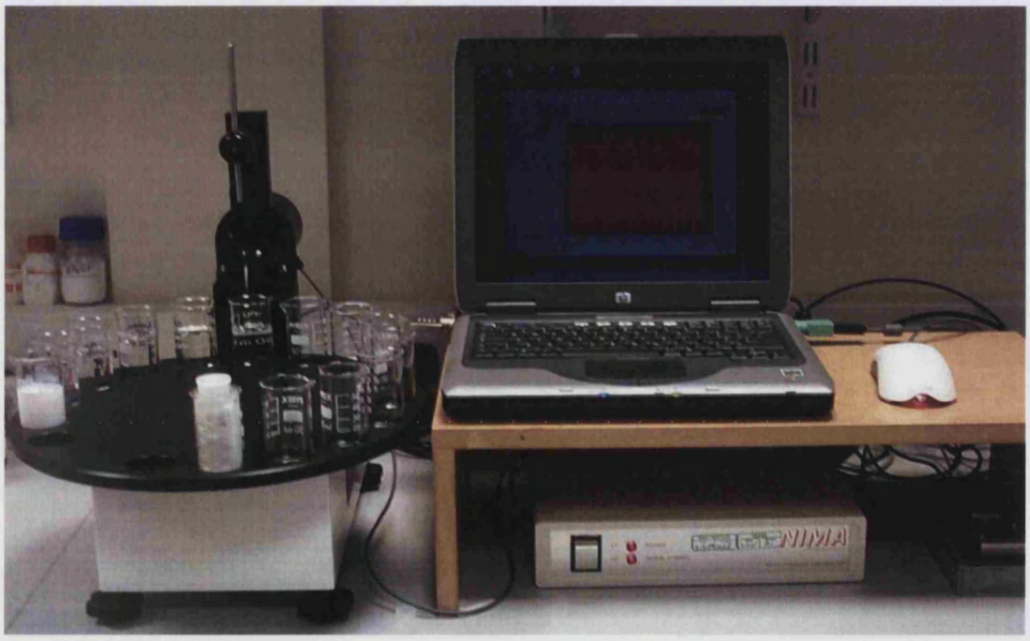

Figure 2.1 PC controlled robotic dip-coater and carousel, by Nima Technology.

For preparation of the purely inorganic metal-oxide nanoparticle films, heat treatment at 500°C in air (Elite tube furnace) was undertaken after the deposition.

Deposition of 40nm TiO_2 nanoparticulate films

40nm diameter TiO_2 particles were obtained in powder form. A stable suspension was made by dispersing the particles in methanol by sonication for 30 minutes. Deposition was carried out simply by dipping the ITO electrode into the TiO_2-methanol suspension and allowing evaporation to occur before another layer is added. Films were heat treated at 500°C in air for 30 minutes in order to improve stability.

Deposition of TiO_2 particles onto boron-doped diamond substrates

For work carried out on the boron-doped diamond electrodes, 20µl of the TiO_2 particle suspension was pipetted onto the surface. The deposit was then dried at 50°C in air in order to obtain a stable film.

2.3 Results and Discussion

2.3.1 Characterisation of TiO_2 films prepared with 6nm particles

Boron-doped diamond allows nanoparticulate oxides such as iron oxide and titanium dioxide to be adsorbed onto the surface in the form of a very thin layer. The inert and well defined surface of the boron-doped diamond allows the electrochemical properties of these nanoparticles to be studied. The positively charged nanoparticles readily adsorb onto the boron-doped diamond substrate, which after treatment with mineral acids leave an oxygen functionalised surface.

The voltammetric response from a boron-doped diamond electrode immersed in an aqueous 0.1M $NaClO_4$/ $HClO_4$ solution between +0.5V Vs SCE and -1.5V vs. SCE is featureless and consistent with a clean background (not shown). After deposition of the 6nm TiO_2 particles a reduction response is detected starting at a potential of -0.8V vs. SCE (figure 2.2i). The shape of this voltammetric response is characteristic of a TiO_2 thin film and has been explained in terms of the sequential filling of electronic states within the oxide[6]. For TiO_2 films more extended than a monolayer, this voltammetric response dominates the overall behaviour.

Scanning to more negative potentials, another peak feature is observed at approximately -1.2V vs. SCE (figure 2.2ii), and after reversal of the scan direction two peaks are also observed during oxidation. Previous reports for the redox response of a TiO_2 monolayer show the separate peaks to be characteristic of a monolayer nanoparticle deposit and were shown to be associated with different proton binding sites within the TiO_2 surface[4].

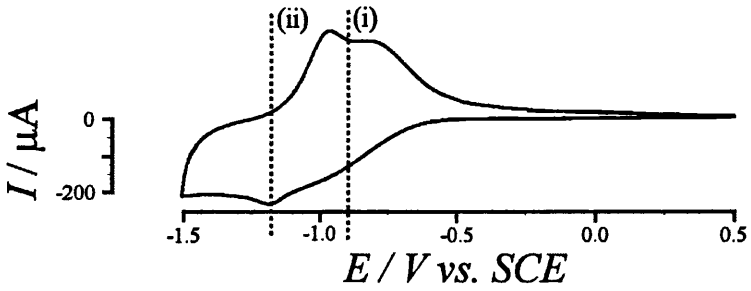

Figure 2.2 Cyclic voltammogram obtained in 0.1M $NaClO_4$ / 2mM $HClO_4$ for 20μl of 6nm TiO_2 nanoparticles deposited on boron-doped diamond electrode (scan rate $100mVs^{-1}$).

Mesoporous films of 6nm TiO_2 are formed using the layer-by-layer deposition method onto a glass substrate with a conducting layer, usually of tin-doped indium oxide (ITO). These substrates are more versatile than boron-doped diamond electrodes; they can be cut to any size required and are less costly. ITO has an overall negative charge allowing the TiO_2 particles to adsorb readily onto the surface. Using phytic acid as a binder, films of up to several microns in depth can be prepared. Figure 2.3 shows a SEM of a 5 layer TiO_2 phytate film on ITO. The film was scratched with a scalpel prior to imaging in order to gain depth information, and the ITO seen underneath is flat and featureless.

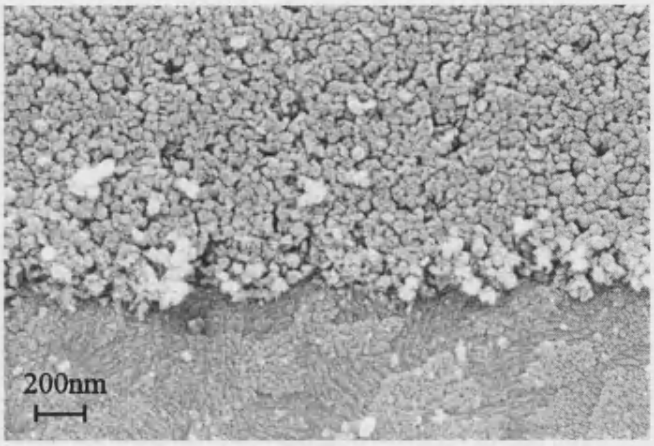

Figure 2.3 SEM of a 5 layer TiO_2 phytate film on ITO

The voltammetric response of the ITO immersed in aqueous 0.1M $NaClO_4$ between +0.5V vs. SCE and -1.0V vs. SCE is featureless and consistent with a clean background (not shown). Figure 2.4 shows the voltammetric response of a 10 layer TiO_2 phytate film on ITO immersed in aqueous 0.1M $NaClO_4$. A reduction response commences at approximately -0.6V vs. SCE and is explained by the filling of electronic states (the conduction band) within the oxide. This signal dominates the overall response and the second peak seen for the monolayer of TiO_2 is assumed to be hidden. Upon reversal of the scan direction an oxidation peak is observed consistent with electrons moving back from the oxide into the substrate electrode. The characteristic shape is determined by (i) capacitive charging of the oxide and (ii) a resistance mainly in the substrate (see below).

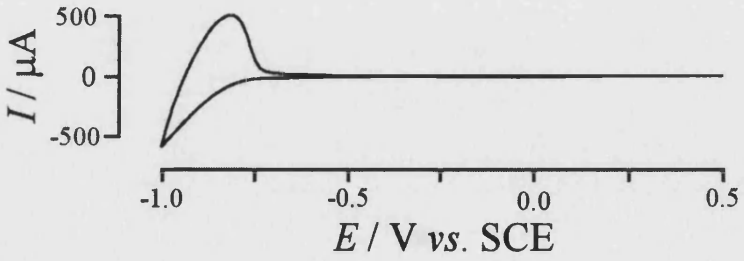

Figure 2.4 Cyclic voltammogram of a 10 layer 6nm TiO_2 phytate film on ITO immersed in 0.1M $NaClO_4$ (scan rate 100mV/s).

Electrochemical impedance measurements of a 10 layer 6nm TiO_2 phytate film on ITO allowed the fit of data to an electrical circuit model consisting simply of a

resistor and capacitor in series. The equivalent electrical circuit can be represented as below:

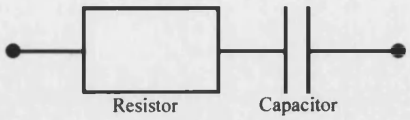

The electrochemical impedance measurements were carried out over a range of potentials starting in the "depletion" region positive of the flat band potential of TiO_2 at +0.5V vs. SCE and going down to the "accumulation" or conducting region of TiO_2 at -1.0V vs. SCE. Figure 2.5 shows (a) a complex plain and (b, c) Bode plots obtained for an impedance measurement along with an example of the fit obtained to the actual data using the resistor and capacitor in series model (the green line).

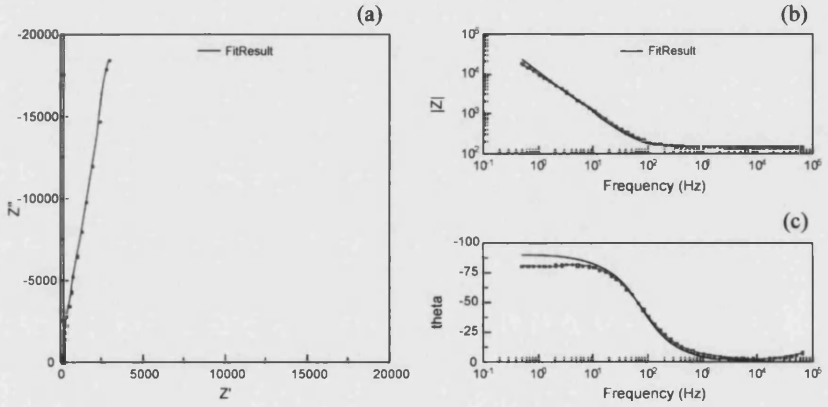

Figure 2.5 Impedance data obtained at +0.5V for a 10 layer TiO_2 phytate film displayed graphically as (a) a complex plain and (b) Bode plots along with the fit obtained (green line).

Potential	Resistance	Capacitance
+0.50V	147.6 Ω	14.0 μF
0.00V	147.1 Ω	20.1 μF
-0.25V	146.7 Ω	25.5 μF
-0.50V	145.4 Ω	31.8 μF
-0.75V	148.6 Ω	151.8 μF
-1.00V	142.1 Ω	8250.0 μF

Table 2.1 Summary of impedance data obtained for a 10 layer TiO_2 phytate film electrode immersed in 0.1M $NaClO_4$.

Table 2.1 shows the resulting values for the resistance and capacitance over a range of potentials. Over the range of potentials tested, the data shows that the resistance of the 10 layer TiO_2 phytate film remains constant. This feature is attributed to the resistance that would occur from the electrons simply crossing from the ITO surface into the film, which should remain constant over all potentials. Over the range of potentials tested, the capacitance of the 10 layer TiO_2 phytate electrode increases at more negative potentials and so can be attributed to the TiO_2 film present on the surface. The TiO_2 particles act as a capacitor, becoming charged up with electrons as the applied potential becomes more negative. This behaviour is consistent with the results obtained by voltammetry.

2.3.2 Characterisation of TiO_2 Films prepared with 40nm particles.

It has been shown that mesoporous films prepared with nanoparticles usually contain pores that are similar/relative in size to the particles that are used to prepare the films. Immobilisation of redox active molecules into these films therefore requires that the molecule is able to diffuse from a solution into these films. For relatively large molecules such as proteins within biological systems, a larger pore size would be necessary to allow diffusion of the molecule into the film. It was shown that hemoglobin could be immobilised in mesoporous TiO_2 films[7] with applications including a cyanide sensor[8] but due to the small pore size created from films prepared from the 6nm TiO_2 particles, the protein could only penetrate the upper layer of the film. Investigations into films prepared with larger particles could overcome this problem.

Dispersion of the 40nm particles into an aqueous solution did not form a time stable suspension from which layer-by-layer films could be produced, as with the 6nm TiO_2 particles. The films produced by this method were not homogenous and would be difficult to characterise electrochemically. However dispersion of the particles into methanol by sonication formed a relatively stable solution and films were prepared by simply dipping an ITO substrate into the solution and allowing evaporation to occur before another layer was applied. Although a variation from the layer-by-layer deposition method, the films formed were more homogenous and could be characterised more easily. Figure 2.6 shows a typical FEGSEM of a

substrate that has undergone 10 cycles of dipping and evaporation followed by annealing at 500°C for 30 minutes.

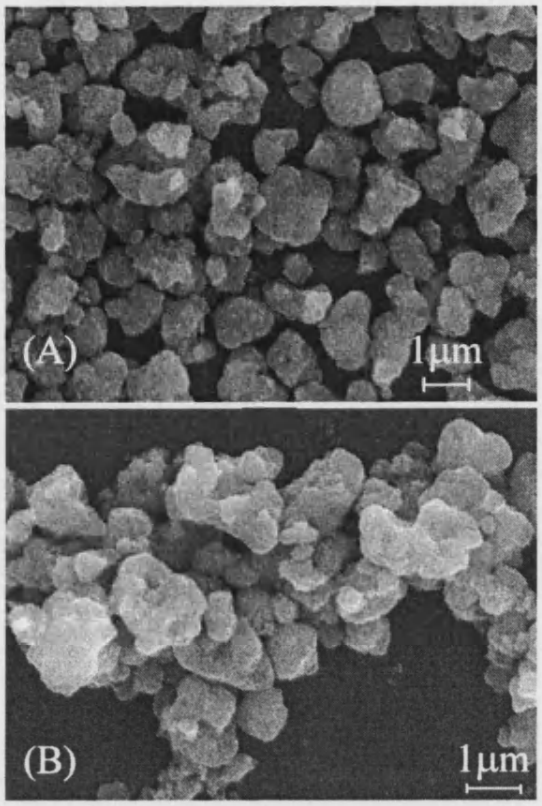

Figure 2.6 SEM of a "10 layer" 40nm TiO_2 film in the form of agglomerated particles on ITO

The sample was scratched with a scalpel prior to imaging and the ITO substrate beneath is flat and featureless. The 40nm particles form deposits ranging from 20μm to single particles. In contrast to the 6nm particle films there is not complete coverage of the ITO substrate on a microscopic scale; however the film formed is homogenous with pores that are capable of immobilising redox active centres. It is thought that the 40nm particles do not completely cover the substrate due to the different deposition mechanism.

The electrochemical response of the 40nm TiO_2 films on ITO is very similar to that of the 6nm particles and typical of a mesoporous TiO_2 film. Figure 2.7 shows a cyclic voltammogram of a 10 layer 40nm TiO_2 film on ITO immersed in aqueous in 0.1M $NaClO_4$. A reversible reduction response commences at approximately -0.6V vs. SCE that dominates the overall signal and is the typical response for TiO_2 films.

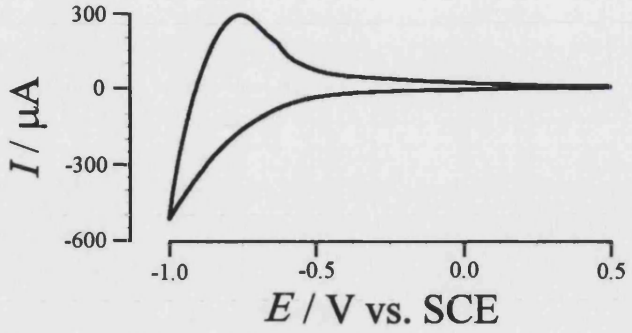

Figure 2.7 Cyclic voltammogram of a 10 layer 40nm TiO2 film on ITO run in aqueous 0.1M $NaClO_4$ ($100mVs^{-1}$)

Electrochemical impedance data was also taken for the 10 layer 40nm TiO_2 film on ITO immersed in aqueous 0.1M $NaClO_4$. The film gave similar behaviour to the 6nm TiO_2 film and again a simple circuit equivalent model of a resistor and capacitor in series was fitted to the data obtained. Figure 2.8 below shows (a) a complex plane and (b, c) bode plots for an impedance measurement along with the fit obtained using the model (green line):

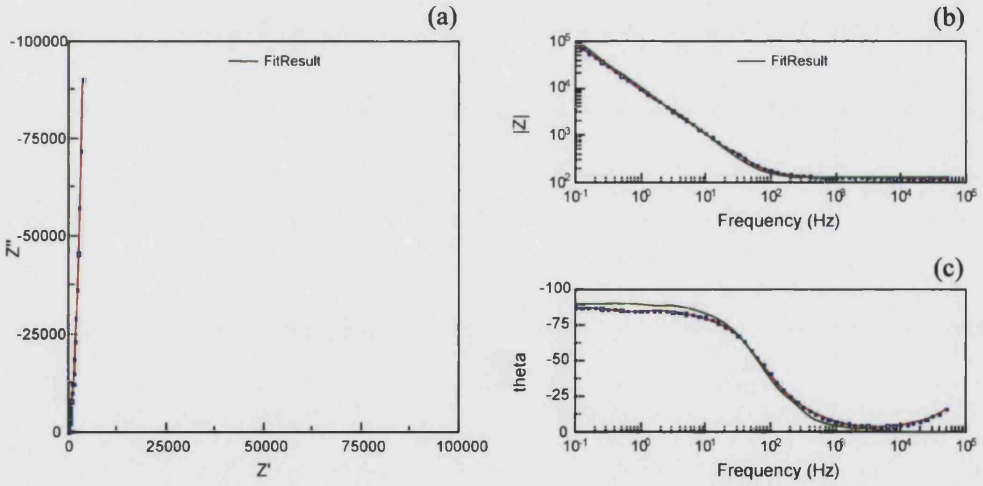

Figure 2.8 Impedance data obtained at +0.5V for a 10 layer 40nm TiO_2 film displayed graphically as (a) a complex plain and (b) Bode plots along with the fit obtained (green line).

Potential	Resistance	Capacitance
+0.50V	124.9 Ω	15.8 μF
0.00V	123.5 Ω	20.0 μF
-0.25V	123.1 Ω	23.6 μF
-0.50V	128.3 Ω	45.6 μF
-0.75V	121.9 Ω	122.7 μF
-1.00V	120.8 Ω	364.0 μF

Table 2.2 Summary of impedance data obtained for a 10 layer 40nm TiO_2 film electrode immersed in 0.1M $NaClO_4$.

Table 2.2 shows the resulting values for the resistance and capacitance over a range of potentials. Results are very similar to those obtained for the 6nm TiO_2 films; the resistance of the electrode stays consistent over the range of potentials and is attributed to the ITO conducting glass substrate. The capacitance of the electrode increases with more negative potential, consistent with the charging of the TiO_2 film. The value of capacitance at -1.0V vs. SCE is less than that for the 6nm TiO_2 films and attributed to the smaller surface area of the 10 layer 40nm TiO_2 film in comparison with the 10 layer 6nm film. Under conditions employed here (very thin films, conventional frequencies) no effect of electron transport within the mesoporous structure is observed. Electron conduction appears to be very fast.

2.4 Conclusion

TiO_2 nanoparticle films are electrochemically active and undergo reduction at potential negative of ca. -0.6 V vs. SCE. Charge transport is fast and possible via electron hopping from particle to particle. Voltammetric and impedance measurements give no direct information about the rate of the electron transport mainly due to the resistance of the ITO limiting the response time.

2.5 References

[1] I. Abayev, A. Zaban, F. Fabregat-Santiago and J. Bisquert, *Phys. Status Solidi A-Appl. Res.*, 2003, **196**, R4-R6.

[2] C. J. Boxley, H. S. White, C. E. Gardner and J. V. Macpherson, *J. Phys. Chem. B*, 2003, **107**, 9677-9680.

[3] H. Pelouchova, P. Janda, J. Weber and L. Kavan, *J. Electroanal. Chem.*, 2004, **566**, 73-83.

[4] F. Marken, A. Bhambra, D. Kim, R. Mortimer and S. Stott, *Electrochem. Commun.*, 2004.

[5] Y. V. Pleskov, *Russ. J. Electrochem.*, 2002, **38**, 1275-1291.

[6] F. Fabregat-Santiago, I. Mora-Sero, G. Garcia-Belmonte and J. Bisquert, *J. Phys. Chem. B*, 2003, **107**, 758-768.

[7] C. A. Paddon and F. Marken, *Electrochemistry Communications*, 2004, **6**, 1249-1253.

[8] C. G. Siontorou and D. P. Nikolelis, *Analytica Chimica Acta*, 1997, **355**, 227-234.

3. Layer-by-Layer Deposition of Open-Pore Mesoporous TiO_2 – Nafion® Film Electrodes

3.1 Introduction

The layer-by-layer deposition of mesoporous oxides is versatile, reproducible, and ideal for the formation of thin coatings on electrode surfaces[1]. The methodology initially developed by Decher[2] allows molecular binders[3], ionomeric binders[4], and other types of nanoparticles[5] to be incorporated into the growing film. In this chapter the effect of employing Nafion® ionomer as a binder for TiO_2 nanoparticles is explored.

Although layer-by-layer deposition is possible with small molecular binders, higher molecular weight ionomers such as Nafion® are known to produce a more stable film[6]. The thickness of a single layer of a film depends on factors such as the weight, size and concentration of the polyelectrolyte binder and of the charged species. Intermolecular forces, hydrophobic forces[7], and hydrogen bonding[8] all have been reported to have an effect on the structure of the deposited films.

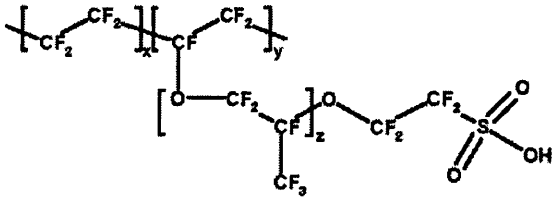

Figure 3.1. Chemical structure of Nafion® ionomer

Composites of Nafion® (a chemically inert fluorocarbon with sulfonic acid groups[9], see figure 3.1) and TiO_2 have been proposed for example for applications in proton-conducting membranes[10], in fuel cells[11], in photoelectrochemical devices[12], for photochemical degradation membranes[13], employed for dopamine sensing[14], and for nitric oxide sensing[15], and they have been produced with Langmuir-Schäfer techniques[16]. The combination of the chemically robust Nafion® binder with the

mesoporous structure formed by the TiO_2 nanoparticle backbone results in a very interesting and widely applicable thin film structure.

In this chapter TiO_2 nanocomposite films are constructed from a Nafion® ionomer binder and ca. 6 nm diameter TiO_2 nanoparticles. A simple dip coating approach allows films of variable thickness to be formed and investigated. Perhaps surprisingly, an open-pore structure is formed consisting primarily of the TiO_2 backbone and a thin film of Nafion® at the surface. Voltammetric measurements in aqueous solution suggest that the charge transport at potentials negative of ca. -0.7 V vs. SCE is dominated by electron conduction through the TiO_2 backbone whereas at more positive potentials diffusion of redox species and inter-molecular electron hopping dominate. The rate for charge transport in the positive potential range is very similar to that measured for conventional bulk Nafion® films.

3.2 Experimental

3.2.1 Chemical Reagents

Nafion® perfluorinated ion-exchange resin (5 wt%, in a mixture of lower aliphatic alcohols and H_2O), $NaClO_4$, KCl, 1,1'-diheptyl-4,4'-bipyridinium dibromide or diheptylviologen, $Ru(NH_3)_6Cl_3$, ferrocenylmethyl-trimethylammonium iodide (all Aldrich) were obtained commercially and used without further purification. TiO_2 sol (ca. 6 nm diameter, anatase, 30-35% in aqueous HNO_3, pH 0.5, TKS-202) was obtained from Tayca Corp, Japan. Solutions were prepared using filtered and deionized water with a resistivity of not less than 18 MΩ cm.

3.2.2 Instrumentation

Voltammetric experiments were performed with an microAutolab III system (Eco Chemie, Netherlands) in a standard three terminal electrochemical cell with a saturated calomel reference electrode, SCE, (Radiometer, Copenhagen) placed ca. 0.5 cm from the working electrode and a 2 cm × 2 cm platinum gauze counter electrode. The working electrodes were made from tin-doped indium oxide (ITO)

coated glass (10 mm × 60 mm, 15 Ω per square, Image Optics, Basildon, UK). The ITO electrode was rinsed with ethanol and water, heat treated in a furnace (Elite Thermal Systems Ltd.) for 1 h at 500 °C, and re-equilibrated to ambient conditions before use. Prior to voltammetric experiments solutions were de-aerated with argon (BOC). All experiments were conducted at a temperature of 22 +/- 2 °C.

Quartz crystal microbalance experiments were conducted with ITO-coated quartz crystals (Part no. QA-A-9M-ITOM, Advanced Measurement Technology, Wokingham, Berks). A quartz crystal oscillator circuit (Oxford Electrodes) connected to a frequency counter (Fluke, PM6680B) allowed the resonance frequency of the quartz crystal sensor to be monitored. The 9.1 MHz AT-cut quartz crystal microbalance system was calculated[17] to have a sensitivity factor of $\frac{\Delta m}{\Delta f}$ = -1.05 ng Hz^{-1} in air based on the expression $\frac{\Delta m}{\Delta f} = -\frac{A \times \sqrt{\mu_Q \rho_Q}}{2 f_0^2}$ with the area A = 0.2 cm^2, the resonance frequency $f_0 = 9.1 \times 10^6$ Hz, the density of quartz ρ_Q = 2.648 gcm^{-3}, and the shear modulus of quartz $\mu_Q = 2.947 \times 10^{11}$ g $cm^{-1}s^2$.

Field emission gun scanning electron microscopy (FEGSEM) images were obtained on a Leo 1530VP Field Emission Gun SEM system. A SAXS/WAXS (simultaneous small-angle X-ray scattering and wide-angle X-ray scattering) pattern of the TiO_2-Nafion® films was obtained on a SAXSess system using a PW3830 X-ray generator and the X-ray image plates were observed using a Perkin Elmer Cyclone Storage Phosphor System. A TiO_2-Nafion® film (50 deposition cycles on a microscopy cover plate) was produced and the patterns recorded in transmission mode with Cu Kα radiation (λ = 1.5406 Å) at 40 kV and 50 mA with an exposure time of 20 minutes. A background pattern from a clean cover plate was subtracted and the data corrected for slit smearing before fitting.

3.2.3. Layer-by-Layer Deposition of TiO_2–Nafion® Films

The deposition procedure consisted of a sequence of liquid immersion steps with (i) a TiO_2 sol (6 nm diameter, 3 wt% in nitric acid, pH ca. 2) for 60 seconds followed by rinsing with distilled water and methanol, (ii) dipping into Nafion® anionomer solution (ca. 0.5 wt% in methanol) for ~10 seconds followed by rinsing with methanol and distilled water. This completed a single layer deposition for the simple TiO_2-Nafion® film and the cycle was repeated to add more layers.

3.3 Results and Discussion

3.3.1 Layer-by-layer Formation of TiO_2 – Nafion® Nanocomposite Film Electrodes

Nafion® is an anionic polymer which is widely used as an ion-exchange membrane material[18] or as a protective semi-permeable coating[19]. Solutions of Nafion® in aliphatic alcohols are employed for the formation of thin films and in this chapter a dilute solution of Nafion® in methanol (0.5 wt%) is employed to act as a binder to grow thin films of a novel open pore TiO_2–Nafion® composite membrane. An aqueous TiO_2 sol provides the source of positively charged TiO_2 nanoparticles of nominal 6 nm diameter which are deposited with the Nafion® binder in a layer-by-layer deposition approach[20]. Tin-doped indium oxide (ITO) coated glass slides were employed as substrate (see section 3.2.2). Due to the positive surface charge of the TiO_2 sol particles, ITO coated glass slides immersed into the nanoparticle solution will readily adsorb a very thin nanoparticle coating. When this electrode is rinsed with water and methanol, and then immersed into a Nafion® solution, binding of the anionic polymer and a restructuring of the surface occur. "Clustering" of TiO_2 nanoparticles into aggregates is observed. The electrode is then rinsed and re-immersed into the TiO_2 sol to continue the deposition process. An FEGSEM image of a 2-layer TiO_2-Nafion® film is shown in Figure 3.2A. It can be seen that the contact with the Nafion® anionomer causes nanoparticles to "cluster" into aggregates of ca. 40 nm diameter.

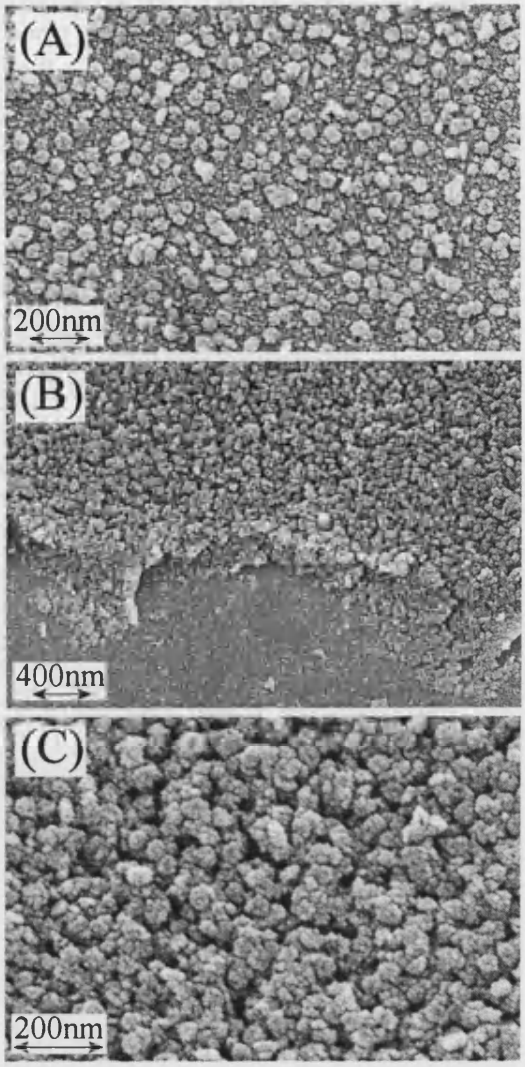

Figure 3.2 FEGSEM images of (A) a 2-layer TiO_2-Nafion® film and (B,C) a 15-layer TiO_2-Nafion® film (scratched with a scalpel) on ITO substrate.

When the deposition process is continued, more aggregates form and they assemble into a porous structure. Figure 3.2B and 3.2C show a 15-layer TiO_2-Nafion® film with pores of typically 10 to 30 nm diameter. These open pores create a hierarchical network and this can be beneficial by allowing gas and fluids to penetrate into the nanocomposite film. The thickness of the porous film is controlled by the number of deposition cycles employed. AFM images reveal the increase in thickness. An image of a 20-layer TiO_2-Nafion® film on an ITO substrate is shown in Figures 3.3A and 3.3B. The film was scratched to reveal the cross section. The 20-layer film showed a height of ca. 500 nm (see Figure 3.3C) which suggests a thickness of approximately 25 nm per deposition cycle which compares well with earlier studies employing other

types of binder molecules[21].

Quartz crystal microbalance measurements at an ITO-coated quartz crystal oscillator were employed to quantify the weight change during the deposition of consecutive layers of the TiO_2-Nafion® nanocomposite. A plot of the frequency of the ITO resonator against the number of layers deposited is shown in Figure 3.3D. This plot shows a linear build up of the TiO_2-Nafion® film with approximately 70 wt% contribution from TiO_2 and 30 wt% from Nafion®. These weight measurements were taken for dry films but may still contain a small contribution from adsorbed water. The Sauerbrey equation allows the average weight to be calculated for TiO_2 particles deposited in one layer, 2600 ng cm^{-2} (corresponding to 6×10^{12} TiO_2 particles using the density of the TiO_2 anatase particles 3.9 g cm^{-3}) and for Nafion® deposited in one layer, 1000 ng cm^{-2}. These values are in good agreement with an average thickness per layer of 25 nm calculated from the AFM measurements.

Further characterisation of the TiO_2-Nafion® nanocomposite film was obtained using the simultaneous small-angle X-ray scattering and wide-angle X-ray scattering (SAXS/WAXS) technique. Figure 3.3E shows the intensity of the scattered X-ray diffraction pattern for both TiO_2-Nafion® and pure (calcined) TiO_2 nanoparticle films. The experimental data can be fitted to a model (see red line) to determine the structure of the nanoparticle films.

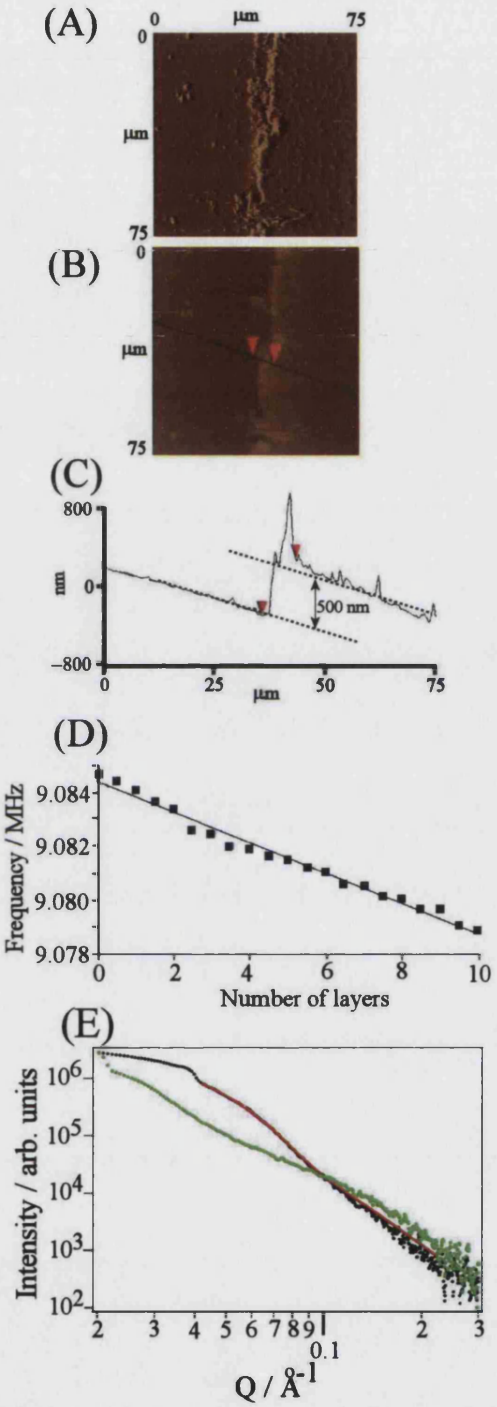

Figure 3.3 AFM image data showing a 20-layer deposit of TiO_2-Nafion® on an ITO surface: (A, B) topography, (C) cross section. The surface has been scratched prior to imaging. (D) Quartz crystal microbalance data obtained during deposition of consecutive TiO_2 and Nafion® layers onto an ITO coated quartz resonator. (E) SAXS/WAXS data: experimental data for TiO_2 film only (black), for a TiO_2-Nafion® film (green), and for a theoretical fit for polydisperse TiO_2 spheres (mean radius 38.81 Å, polydispersity 0.295) (red line).

The simulation model is that of isolated polydisperse spheres with a mean radius of 38.81 Å (assuming no interaction between each sphere) and is seen to give an excellent fit for the calcined TiO_2 film (treated at 500 °C in air for 30 minutes) between 0.04 and 0.1 $Å^{-1}$ indicating that there is no significant colloidal crystallinity. The small divergence between the fit and experimental data at greater values of Q may suggest possible interaction between spheres. A step in the intensity level is observed in the TiO_2-Nafion® and pure TiO_2 film at 0.04 $Å^{-1}$ and 0.08 $Å^{-1}$ respectively, which relates to the size of the particle or aggregate spheres. It is possible to establish that the TiO_2-Nafion® aggregates are on average almost double the size of pure TiO_2 nanoparticles. However, a more complex composite structure is present which is not easily modeled with conventional approaches. From FEGSEM image evidence (see Figure 3.2) a raspberry-type packing or hierarchical clustering seems to occur. The step in intensity level at 0.02 $Å^{-1}$ and 0.04 $Å^{-1}$ in the TiO_2-Nafion® and pure TiO_2 films, respectively, can be attributed to an artifact generated after the subtraction of the background scattering pattern.

3.3.2 Electrochemical Processes in TiO_2 – Nafion® Nanocomposite Film Electrodes

The voltammetric response observed for a clean ITO electrode immersed in aqueous 0.1 M KCl (used as an inert electrolyte) between +0.5 V vs. SCE and -1.0 V vs. SCE is featureless and consistent with a clean background (not shown). Figure 3.4 shows the voltammetric responses for a series of TiO_2-Nafion® films on ITO immersed in 0.1 M KCl. A reduction response commences at -0.7 V vs. SCE which is typical for a TiO_2 film and is explained by the filling of the conduction band within the oxide[22]. Upon reversal of the scan direction an oxidation peak is observed which is consistent with electrons moving back from the oxide to the ITO substrate. The basic shape of the voltammograms can be explained by capacitive charging of the oxide and a resistance, which is mainly due to the ITO film[23]. The three different electrodes were (i) 2, (ii) 10, and (iii) 20 layers of TiO_2-Nafion®. The increase of TiO_2 film thickness is demonstrated by the approximately proportional increase in the voltammetric response, which is associated with the reduction of Ti(IV).

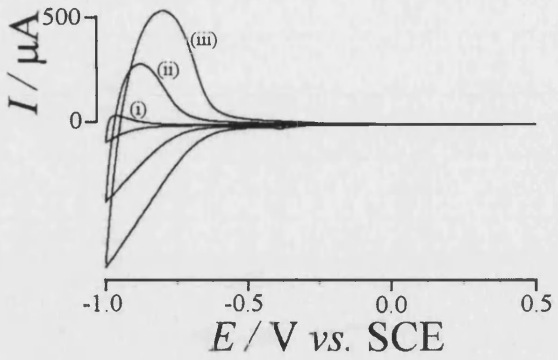

Figure 3.4 Cyclic voltammograms (scan rate 100 mVs^{-1}) for the reduction and oxidation of 6 nm TiO_2 nanoparticles bound by Nafion®, immobilized on ITO electrodes (area 1 cm^2) immersed in 0.1 M KCl. (i) 2 layers TiO_2, (ii) 10 layers TiO_2, (iii) 20 layers TiO_2.

In order to explore the reactivity of the TiO_2-Nafion® film in the presence of redox systems, three cationic redox systems with reversible one-electron characteristics have been chosen with reversible potentials close to and more positive away from the TiO_2 conduction band edge.

The 1,1'-diheptyl-4,4'-bipyridinium (or diheptylviologen) system exhibits a reversible redox process at -0.62 V vs. SCE (see Figure 3.5A) and a second reversible reduction step at more negative potentials (not shown)[24]. In order to obtain this response, a 5-layer TiO_2-Nafion® film was immersed into a solution of 1,1'-diheptyl-4,4'-bipyridinium dibromide (1 mM in ethanol) for one minute. The 1,1'-diheptyl-4,4'-bipyridinium was quickly immobilised into the Nafion® binder in the TiO_2-Nafion® film. The resulting electrode was then placed into aqueous 0.1 M KCl electrolyte and a cyclic voltammogram was recorded.

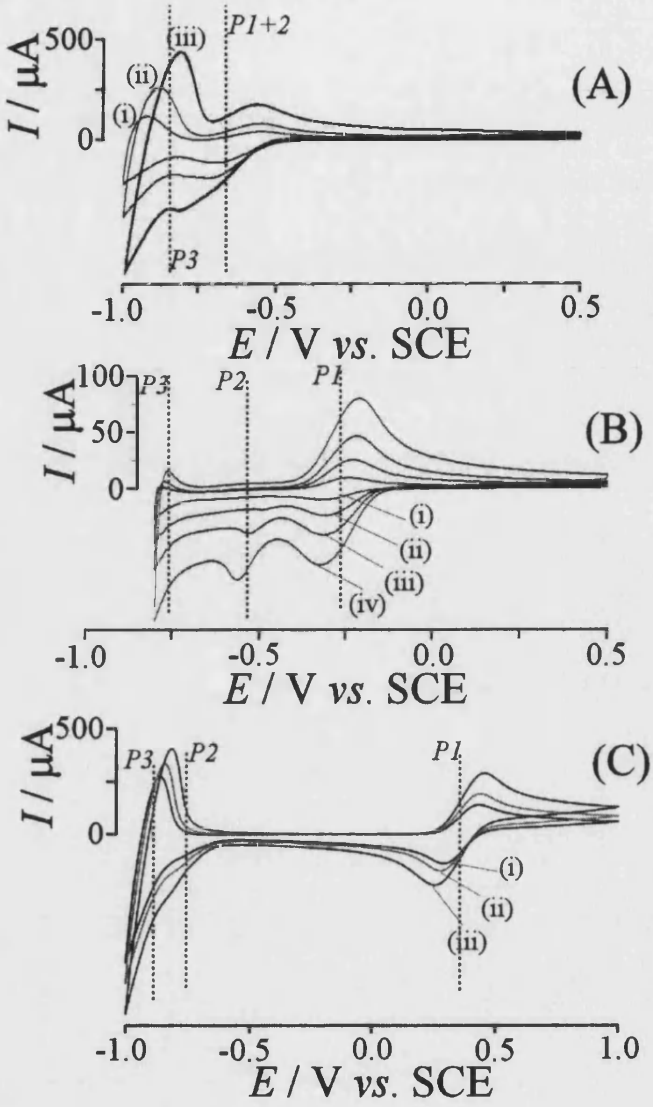

Figure 3.5. (A) Cyclic voltammograms (scan rates (i) 20, (ii) 50, (iii) 100 mVs^{-1}) for the reduction and oxidation of 1,1'-diheptyl-4,4'-bipyridinium in a 5-layer TiO_2-Nafion® film immobilized onto an ITO surface (area 1 cm^2). The electrode was first immersed into a 1 mM solution of 1,1'-diheptyl-4,4'-bipyridinium dibromide in ethanol for 1 minute, then rinsed with ethanol, and then the electrode was immersed in a 0.1 M KCl electrolyte. (B) Cyclic voltammograms (scan rates (i) 20, (ii) 50, (iii) 100, and (iv) 200 mVs^{-1}) for the reduction and oxidation of $Ru(NH_3)_6^{3+}$ in a 20-layer TiO_2-Nafion® film. The electrode was first immersed into 1 mM $Ru(NH_3)_6^{3+}$ in water, then rinsed with water, and then the electrode was immersed into a 0.1 M KCl electrolyte. (C) Cyclic voltammograms (scan rates (i) 20, (ii) 50, and (iii) 100 mVs^{-1}) for the reduction and oxidation of ferrocenylmethyl-trimethylammonium$^+$ in a 20-layer TiO_2-Nafion® film. The electrode was first immersed into 1 mM ferrocenylmethyl-trimethylammonium iodide in water, then rinsed with water, and then the electrode was immersed into a 0.1 M KCl electrolyte. Dashed lines indicate the

approximate potential for redox processes.

In Figure 3.5A, Process 1 (P1) denotes the reduction of 1,1'-diheptyl-4,4'-bipyridinium^{2+} to 1,1'-diheptyl-4,4'-bipyridinium^{+} by electrons directly from the ITO electrode surface (see equation 3.1). This particular mechanism operates solely at the ITO surface and requires molecular or charge diffusion within the Nafion® film. A second type of electron transfer is possible at more negative potentials, denoted Process 2 (see equation 3.2). TiO_2 at sufficiently negative potentials is conducting electrons and therefore direct electron transfer from TiO_2 becomes possible[25].

Process 1: $[Ox]^{n+}$(Nafion®) + e^-(ITO electrode) $\rightleftharpoons$ $[Red]^{(n-1)+}$(Nafion®) (3.1)

Process 2: $[Ox]^{n+}$(Nafion®) + $e^-(TiO_2)$ $\longrightarrow$ $[Red]^{(n-1)+}$(Nafion®) (3.2)

Process 3: $Ti(IV)(TiO_2)$ + e^-(ITO electrode) + H_2O $\rightleftharpoons$ $Ti(III)(TiO_2)$ + $H^+(TiO_2)$ + OH^- (3.3)

A third process observed at potentials negative of -0.7 V vs. SCE can be attributed to the conduction band filling of TiO_2 (see Figure 3.4) which is associated with proton uptake (see equation 3.3). Next, a 20-layer TiO_2-Nafion® film is immersed into a solution of $Ru(NH_3)_6^{3+}$ (1 mM in water) for one minute. The cationic $Ru(NH_3)_6^{3+}$ is immobilised into the Nafion® binder and after rinsing with water a reversible voltammetric response is observed at -0.25 V vs. SCE (see Figure 3.5B). This voltammetric signal occurs positive of the potential zone where TiO_2 is conducting and therefore can be attributed purely to Process 1 (equation 3.1). A new separate irreversible reduction peak at -0.5 V vs. SCE corresponds to Process 2, the $Ru(NH_3)_6^{3+}$ reduction via TiO_2 (equation 3.2).

Finally, a redox system with even more positive reversible potential was selected. Ferrocenylmethyl-trimethylammonium^{+} ($TMAFc^+$) is readily adsorbed into Nafion® and shows highly reversible electron transfer characteristics. A 20-layer TiO_2-Nafion® film was immersed into a solution of Ferrocenylmethyl-trimethylammonium iodide (1 mM in water) for one minute. The $TMAFc^+$ cation was immobilised into

the Nafion® anionomer binder. The resulting electrode was then immersed into aqueous 0.1 M KCl electrolyte and voltammograms recorded (see Figure 3.5C). A reversible response at 0.37 V vs. SCE corresponds to Process 1 (equation 3.1), the one electron oxidation/reduction of $TMAFc^+$ by electrons directly from the ITO surface. A second reduction response is observed at -0.75 V vs. SCE (see Process 3.2). The signal is irreversible and observed only immediately after scanning into the $TMAFc^+$ oxidation. It is interesting to note that the potential for Process 2 is dependent on the type of redox system and this may reflect (i) the rate of electron transfer from TiO_2 to the molecular redox system and (ii) the ability of the redox system to interact with the TiO_2 nanoparticle surface. More hydrophobic redox systems such as $TMAFc^+$ appear to interact less effectively with TiO_2 which may be responsible for the shift of Process 2 to more negative potentials.

Next, electron and charge transport within the mesoporous TiO_2-Nafion® film is investigated in more detail. By changing the film thickness and the potential scan rate quantitative insights into the charge transfer and diffusion within the nanocomposite films can be obtained.

3.3.3 Charge Diffusion in TiO_2 – Nafion® Nanocomposite Film Electrodes

By focusing on one particular redox system, ferrocenylmethyl-trimethylammonium$^+$, it is possible to further explore the effects of charge diffusion in the TiO_2-Nafion® composite material. Initially, a study of the adsorption characteristics of the ferrocenylmethyl-trimethylammonium cation ($TMAFc^+$) into the TiO_2-Nafion® films was undertaken. Figure 3.6 shows the experimental results indicating a reversible voltammetric response at a potential of +0.35 V vs. SCE with increasing peak area as a function of $TMAFc^+$ immobilization concentration. Essentially Langmuirian characteristics are observed and for $TMAFc^+$ a binding constant of 9000 mol^{-1} dm^3 can be extracted.

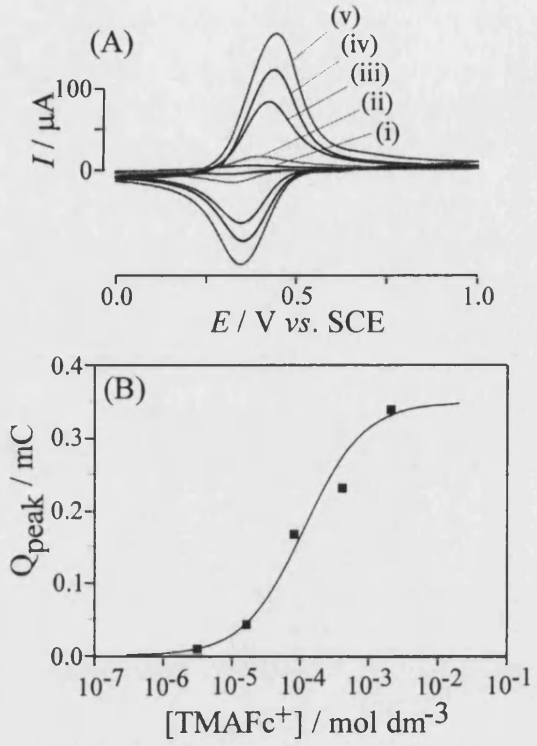

Figure 3.6 (A) Cyclic voltammograms (scan rate 0.1 V s^{-1}) for the oxidation and re-reduction of ferrocenylmethyl-trimethylammonium$^+$ immobilized into a 5-layer TiO_2-Nafion® film at an ITO electrode surface (area 1 cm^2) and immersed into aqueous 0.1 M $NaClO_4$. The ferrocenylmethyl-trimethylammonium$^+$ concentration during the immobilizations step was (i) 3.2 μM, (ii) 16 μM, (iii) 80 μM, (iv) 0.4 mM, and (v) 2 mM in water. (B) Plot of the ferrocenylmethyl-trimethylammonium$^+$ concentration in the immobilization solution versus the charge under the voltammetric signal. The line shows a Langmuir dependence with a binding constant of K = 9000 mol^{-1} dm^3.

The transport of charges in the porous TiO_2-Nafion® membrane is an interesting feature and must be connected to both (i) the mobility of an immobilized redox system such as $TMAFc^+$ and (ii) intermolecular electron hopping. In the positive potential range TiO_2 is clearly electrically insulating and charge transport along the pore walls within the mesoporous composite must be occurring. This was further confirmed by calcination of the TiO_2-Nafion® nanocomposite (this treatment at 500 °C in air fully removed all organic components and leaves a purely inorganic anatase film, see Figure 3.3E) followed by re-adsorption of Nafion® from the dip coating solution (this process took approximately 24h for a 20-layer film due to slow penetration of the anionomer back into the porous TiO_2). The resulting calcined film

is believed to have much better TiO_2 particle-particle contacts but otherwise very similar dimensions. However, the voltammetric features did not change significantly (see below) and therefore a contribution from the TiO_2 backbone to charge conductivity is highly unlikely.

In order to study the effect of the film thickness on the voltammetric features a sequence of experiments was undertaken using a 2 mM $TMAFc^+$ deposition solution and a 0.1 M $NaClO_4$ electrolyte solution (see Figure 3.7). The increase in film thickness clearly results in an increase of the voltammetric peak current.

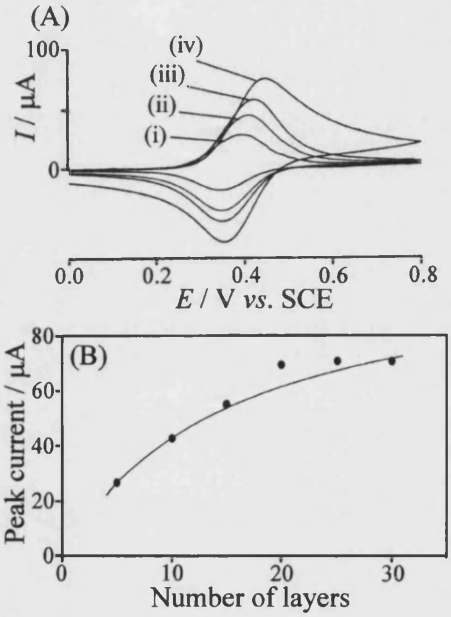

Figure 3.7. (A) Cyclic voltammograms (scan rate 0.02 V s^{-1}) for the oxidation and re-reduction of ferrocenylmethyl-trimethylammonium$^+$ immobilized into a (i) 5, (ii) 10, (iii) 15, and (iv) 30-layer TiO_2-Nafion® film at an ITO electrode surface (area 1 cm^2) and immersed into aqueous 0.1 M $NaClO_4$. The ferrocenylmethyl-trimethylammonium$^+$ concentration during the immobilizations step was 2 mM in water. (B) Plot of the peak current versus the number of deposition layers. The line corresponds to a fit employing equation 3.6 with a concentration of c = 0.1 M and an apparent diffusion coefficient of $D = 3.5 \times 10^{-14}$ m^2s^{-1}.

The relationship of the peak current with film thickness (see Figure 3.7B) is not proportional and at sufficiently thick films (ca. 1 μm) a stable peak current remains, completely independent of thickness. This transition in behaviour is consistent with a

diffusion layer thickness in the mesoporous film. Approximate expressions can be written to describe this effect. The peak current for complete electrolysis of the thin film at the electrode surface is given by equation 3.4[26].

$$I_{p,\text{thin film}} = \frac{n^2F^2}{4RT}vVc = \frac{n^2F^2}{4RT}vA\delta c \qquad (3.4)$$

In this equation, the peak current is related to the number of transferred electrons per molecule diffusing to the electrode surface, n, the Faraday constant, F, the gas constant, R, the absolute temperature, T, the scan rate, v, the electrode area, A, the film thickness, δ, and the concentration of redox active material, c. In contrast, for a thick film a diffusion-controlled peak current (assuming a homogeneous material) is expected (see equation 3.5[27]).

$$I_{p,\text{diffusion}} = 0.446nFAc\sqrt{\frac{nFvD}{RT}} \qquad (3.5)$$

In this equation the apparent diffusion coefficient is denoted by D. The transition of behaviour as a function of film thickness may be approximated by combining these two expressions in equation 3.6.

$$I_p = \frac{I_{p,\text{thin film}} \times I_{p,\text{diffusion}}}{I_{p,\text{diffusion}} + I_{p,\text{thin film}}} = \frac{n^2F^2vDAc\,\delta}{4RTD + 2.242\sqrt{RTDFnv}\,\delta} \qquad (3.6)$$

Analysis of the thickness dependent voltammetric peak current data (see Figure 3.7B and equation 3.6) suggests an approximate apparent diffusion coefficient of $D = 3.5 \times 10^{-14}$ m^2s^{-1} for $TMAFc^+$. This value is very similar to the apparent diffusion coefficients reported, for example, for $Ru(bipy)_3^{3+/2+}$ in pure Nafion®[28,29].

Next, the scan rate is systematically varied. In Figure 3.8 voltammetric data for the oxidation of $TMAFc^+$ immobilised in a 5-layer TiO_2-Nafion® film are shown. A plot of the logarithm of the peak current versus the logarithm of the scan rate is expected to result in two linear regions: (i) a linear region with slope 1 due to thin film

behaviour (see equation 3.4) and (ii) a region with slope ½ due to diffusion within the film (see equation 3.5).

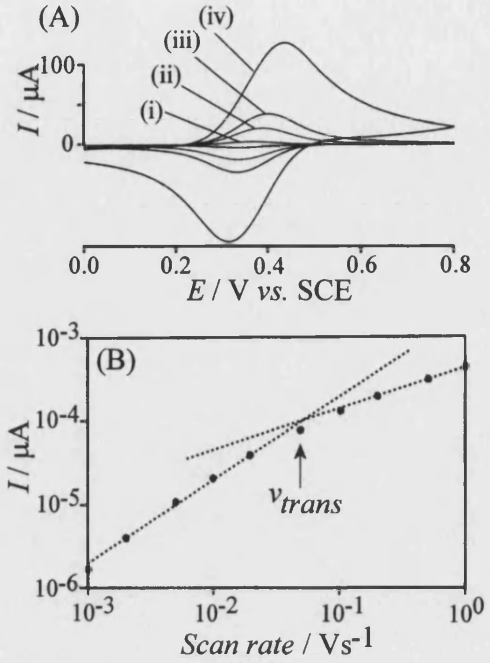

Figure 3.8. (A) Cyclic voltammograms (scan rate (i) 0.002, (ii) 0.01, (iii) 0.02, (iv) 0.1 V s^{-1}) for the oxidation and re-reduction of ferrocenylmethyl-trimethylammonium$^+$ immobilized into a 5-layer TiO_2-Nafion® film at an ITO electrode surface (area 1 cm^2) and immersed into aqueous 0.1 $NaClO_4$. The ferrocenylmethyl-trimethylammonium$^+$ concentration during the immobilizations step was 2 mM in water. (B) Plot of the peak current for the oxidation peak versus scan rate.

The plot in Figure 3.8B clearly shows a transition between thin film and diffusion characteristics at a transition scan rate of $v_{trans} \approx 0.05$ Vs^{-1}. By combining equations 3.4 and 3.5 an approximate expression for this transition can be obtained (equation 3.7).

$$D = \frac{n v_{trans} F}{RT}\left(\frac{\delta}{1.784}\right)^2 \quad (3.7)$$

For data in Figure 3.8B the apparent diffusion coefficient is calculated as $D \approx 1 \times 10^{-14}$ m^2s^{-1} in good agreement with the estimate obtained above. The thickness of the

film δ introduces a considerable error into this calculation and therefore the methodology based on thickness variation is probably more accurate.

3.4 Conclusion

It has been shown that well defined open-pore mesoporous structures are obtained by a layer-by-layer deposition of TiO_2 with Nafion® ionomer binder. TiO_2 particles of nominal 6 nm diameter tend to cluster into aggregates of ca. 20-40 nm size. The properties of the resulting films have been investigated and redox reactions for three cationic redox systems studied. At potentials sufficiently positive of the conduction band edge, charge propagation/diffusion within the films is entirely due to electron hopping and molecular diffusion and very similar in magnitude when compared to processes in conventional Nafion® membrane systems. The open structure of these films allows fast diffusional access into the porous structure and in future this kind of membrane could be beneficial as a sensor film or it could be employed as a host for proteins or enzymes.

3.5 References

[1] Stott S.J., Mortimer R.J., McKenzie K.J., Marken F., *Analyst*, **2005**, 130: 358

[2] Decher G., Schlenoff, *Multilayer thin films*, **2003**, Wiley-VCH, Weinheim

[3] McKenzie K.J., Marken F., Hyde M., Compton R.G., *New J Chem*, **2002**, 26: 625

[4] Murphy M.A., Wilcox G.D., Dahm R.H., Marken F., *Ind J Chem A*, **2005**, 44: 924

[5] Milsom E.V., Novak J., Oyama M., Marken F., *Electrochem Commun*, **2007**, 9: 436

[6] Correa-Duarte M.A., Gierig M., Kotov N.A., Liz-Marzan L.M., *Langmuir*, **1998**, 14: 6430

[7] Neivandt D.J., Gee M., Tripp C.P., Hair M.L., *Langmuir*, **1997**, 13: 2519

[8] Serizawa T., Yamamoto K., Akashi M., *Langmuir*, **1999,** 15: 4682

[9] Davis T.A., Genders J.D., Pletcher D., *Ion permeable membranes*, **1997**, The Electrochemical Consultancy, Romsey, UK

[10] Shao Z.G., Xu H., Li M., Hsing I.M., *Solid State Ionics*, **2006**, 177: 779

[11] Chalkova E., Fedkin M.V., Wesolowski D.J., Lvov S.N., *J Electrochem Soc*, **2005**, 152: A1742

[12] Park H., Choi W., *Langmuir*, **2006**, 22: 2906

[13] Park H., Choi W., *J Phys Chem B*, **2005**, 109: 11667

[14] Yuan S., Hu S., *Electrochim Acta*, **2004,** 49: 4287

[15] Wang Y., Li C., Hu S., *J Solid State Electrochem*, **2006**, 10: 383

[16] Bertoncello P., Notargiacomo A., Nicolini C., *Langmuir*, **2005**, 21: 172

[17] Ward M.D., in Rubinstein I (ed), *Physical Electrochemistry*, **1995,** Marcel Dekker, New York, p 297

[18] Buttry D.A., Anson F.C., *J Am Chem Soc*, **1982**, 104: 4824.

[19] Mortimer R.J., *J Electroanal Chem*, **1995**, 397: 79

[20] Farhat T.R., Hammond P.T., *Adv Func Mater*, **2006**, 16: 433

[21] McKenzie K.J., Marken F., *Langmuir*, **2003,** 19: 4327

[22] Marken F., Bhambra A.S., Kim D.H., Mortimer R.J., Stott S.J., *Electrochem Commun*, **2004,** 6: 1153

[23] Fabregat-Santiago F., Mora-Sero I., Garcia-Belmonte G., Bisquert J., *J Phys Chem B*, **2003**, 107: 758

[24] Mortimer R.J., Dillingham J.L., *J Electroanal Chem*, **1997**, 144: 1549

[25] Milsom E., Perrott H.R., Peter L.M., Marken F., *Langmuir*, **2005**, 21:9482

[26] Bard A.J., Faulkner L.R., *Electrochemical methods*, 2nd edition, **2001**, Wiley,

New York, p 591

[27] Scholz F., *Electroanalytical methods*, **2002,** Springer, Berlin, p 64

[28] Majda M. in Murray R., *Molecular design of electrode surfaces*, **1995**,Wiley, New York, p 200

[29] Buttry D.A., Anson F.C., *J Am Chem Soc*, **1983**, 105: 685

4. Electrochemical Characterisation of TiO_2 FAD Composite Films

4.1 Introduction

The study of mesoporous titania structures is of high importance for applications for example in sensors[1], photovoltaic cells[2,3,4], electrochromic devices[5], thin film coatings[6], and a wide range of other applications[7]. Recently it has been shown that thin films of titania can be formed in a layer-by-layer deposition process from an aqueous sol and with the help of a molecular binder. Typical binder systems for TiO_2 include polydentate anionic molecules such as phytic acid[8], hexametaphosphate and cyclohexane hexacarboxylic acid[9], or carboxymethyl-cyclodextrin derivatives[10]. It is shown here that a more complex and redox-active molecule such as flavin adenine dinucleotide (FAD, see Figure 4.1) can also be employed as a molecular binder. The resulting structures show electrochemical activity associated with the flavin group[11] and allow electron transfer and transport processes to be explored by voltammetry.

FAD is a naturally occurring redox system with flavin as the redox active structural unit (see Figure 4.1). Based on their ability to exchange electrons and to form covalently bound reaction intermediates, flavins and riboflavins are highly versatile chemical and biological building blocks with active roles in a variety of biological processes, e.g. in the respiratory chain and in catalytic flavoproteins[12]. The redox chemistry of flavin derivatives has been of high interest[13].

The Langmuirian adsorption and electrochemistry of FAD on various types of electrodes[14] and in particular onto TiO_2 electrodes[15] has been reported. Also, the immobilization by electropolymerisation of FAD derivatives is possible and has been demonstrated to give very stable and electrocatalytically active electrodes[16,17]. Recently, the self-assembly of FAD with ZnO into electrochemically active films has been reported[18]. The electrochemical properties of FAD and other flavin derivatives are of interest as mediator systems for example in sensors[19] and for the electrocatalytic oxidation of NADH[20]. The electrochemistry of FAD at anodized titanium electrodes was investigated under conditions of variable pH and in different electrolyte systems[21]. It was demonstrated that the effect of pH is consistent with

that expected for a two electron – two proton reduction process as indicated in Figure 4.1.

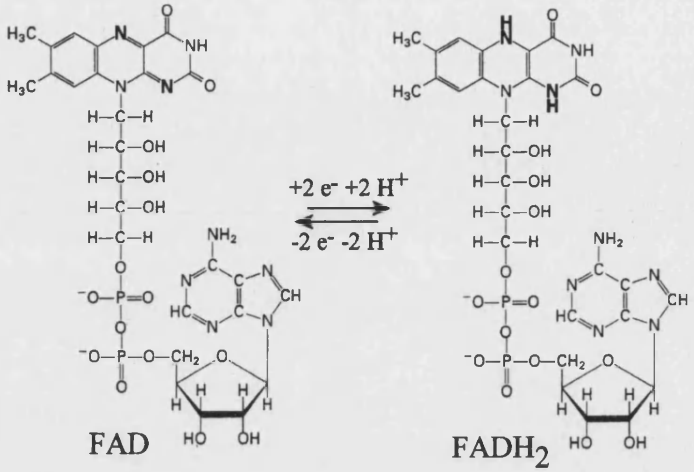

Figure 4.1 The molecular structure of flavin adenine dinucleotide (FAD) in the oxidized and in the reduced form. Binding to TiO_2 is most likely via the diphosphate group.

In this chapter a novel layer-by-layer film of TiO_2 FAD is formed by alternating exposure of an electrode surface to aqueous solutions containing (i) TiO_2 nanoparticles of ca. 6 nm diameter and (ii) FAD. Mesoporous films are grown with variable thickness and the electrochemical characteristics of FAD within the membrane are explored. Spacer layers of TiO_2 phytate are introduced between electrode surface and TiO_2 FAD and it is demonstrated that diffusion of electrons through the TiO_2 structure is facile. Finally, the comparison of the electrochemical characteristics of a calcined (binder-less) TiO_2 structure and a layer-by-layer grown TiO_2 structure strongly suggest that electronic changes occur during calcination which affect the availability, mobility, or interfacial transfer of electrons within the mesoporous structure.

4.2 Experimental

4.2.1 Chemical Reagents

1,2,4,5-Benezenetetracarboxylic acid or pyromellitic acid (96%), phytic acid (*myo*-inositolhexakis(dihydrogen phosphate) dodecasodium salt hydrate), perchloric acid

(70% A.C.S reagent), phosphoric acid (85% wt% in water A.C.S reagent), $K_4Fe(CN)_6$, NaOH, KCl (all Aldrich), FAD (flavin adenine dinucleotide, Sigma) were obtained commercially and used without further purification. TiO_2 sol (ca. 6 nm diameter, anatase, 30-35% in aqueous HNO_3, pH 0-1, TKS-202) was obtained from Tayca Corp, Japan. Solutions were prepared using deionized water with a resistivity of not less than 18 MΩ cm.

4.2.2 Instrumentation

Voltammetric experiments were performed with an Autolab PGSTAT20 system (Eco Chemie, Netherlands) in a standard three terminal electrochemical cell with a saturated calomel reference electrode, SCE, (Radiometer, Copenhagen) placed ca. 0.5 cm from the working electrode and a 2 cm × 2 cm platinum gauze counter electrode. The working electrodes were made from tin-doped indium oxide (ITO) coated glass (10 mm × 60 mm, 15 Ω per square, Image Optics, Basildon, UK). The ITO electrode was rinsed with ethanol, heat treated in the furnace for 1 h at 500 °C, and re-equilibrated to ambient conditions prior to use. Atomic force microscopy (AFM) images were obtained with a Digital Instruments Nanoscope IIIa MultiMode Scanning Probe Microscope in the AFM contact mode. Field emission gun scanning electron microscopy (FEGSEM) images were obtained on a Leo 1530VP Field Emission Gun SEM system. Samples were gold coated (ca. 3 nm) in a sputter coating unit prior to imaging. Layer-by-layer deposits were prepared using a robotic dip coater (DSG Dip Carousel, Nima Technology, Coventry, UK). Prior to voltammetric experiments solutions were de-aerated with argon (BOC). All experiments were conducted at a temperature of 22 +/- 2 °C.

4.2.3 Layer-by-layer Formation of TiO_2 membrane films

The deposition procedure consisted of a sequence of dipping steps with (i) a TiO_2 sol (6 nm diameter, 3%wt in nitric acid, pH 2) for 60 seconds, (ii) distilled water for 30 seconds, (iii) distilled water for 30 seconds, (iv) binder solution for 60 seconds, (v) distilled water for 30 seconds, and (vi) distilled water for 30 seconds. This completed a single layer deposition and the cycle was repeated for each layer formed. Binder

solutions employed in this study were 2 mM FAD in distilled water, 40 mM phytate (adjusted with $HClO_4$ to pH 3), or 40 mM pyromellitate (adjusted with $HClO_4$ to pH 3).

Typical atomic force microscopy (AFM) images of films formed after 1 layer and after 10 layer deposition of TiO_2 FAD are shown in Figure 4.2. The electrode surface was scratched with a scalpel prior to imaging in order to expose the bare electrode and to allow film thickness information to be obtained. It can be seen that a single layer deposit has a thickness of approximately 30 nm (Figure 4.2A) whereas a 10 layer deposit has a thickness of approximately 300 nm (Figure 4.2B). This is entirely consistent with earlier reports describing the layer-by-layer deposition of TiO_2 phytate films[22]. Experiments conducted with pyromellitic acid as the binder also result in the deposition of films of ca. 30 nm thickness per layer. Figure 4.2C shows an FEGSEM image for a 1-layer TiO_2 FAD film confirming homogeneity.

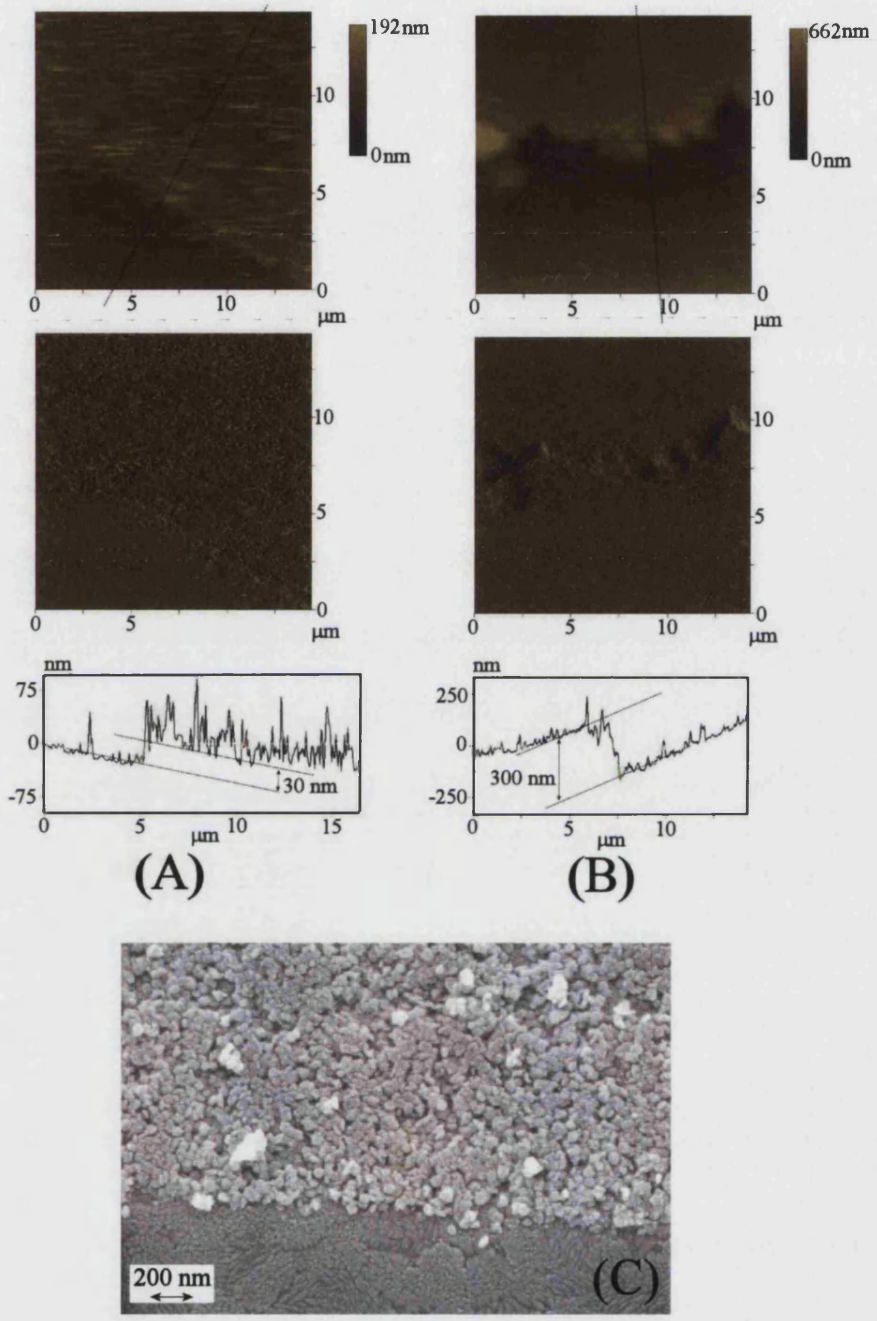

Figure 4.2 AFM data showing (A) a 1 layer deposit of TiO_2 FAD on ITO and (B) a 10 layer deposit of TiO_2 FAD on ITO. The surface has been scratched with a scalpel prior to imaging. The difference in film thickness is consistent with a deposition of ca. 30 nm TiO_2 particles per layer. (C) FEGSEM images for a 1 layer TiO_2 FAD film on ITO. The film deposit has been scratched with a scalpel prior to imaging. Individual particles of ca. 6 nm diameter can be seen to form agglomerates in a mesoporous structure.

4.3 Results and Discussion

4.3.1 Electrochemical Reactivity of TiO_2 FAD Films

In solution, FAD is reduced to $FADH_2$ (see Figure 4.1) via a semiquinone intermediate[23] and the mechanism for the overall process is both pH and electrode material dependent. Figure 4.3 shows typical cyclic voltammograms for the reduction of 1 mM FAD in 0.1 M KCl (stabilized with 2 mM phosphate buffer at pH 7) obtained at a bare ITO electrode. A complex and quasi-reversible reduction – oxidation response is observed with a reversible potential of -0.46 V vs. SCE. By adjusting the pH over a range from 6 to 8 a gradual shift of this voltammetric response with approximately 59 mV per pH unit is observed consistent with the Nernst equation for either a one electron – one proton or a two electron – two proton process.

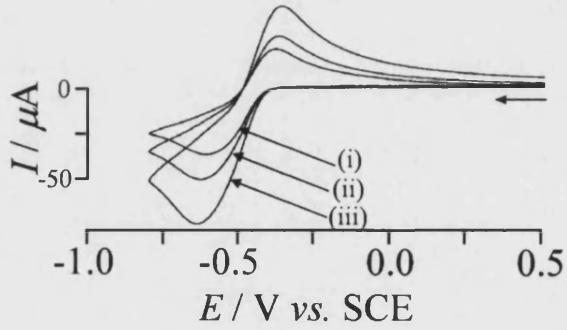

Figure 4.3 Cyclic voltammograms (scan rates (i) 0.02 V s^{-1}, (ii) 0.05 V s^{-1}, and (iii) 0.1 Vs^{-1}) for the reduction of 1 mM FAD in aqueous 0.1 M KCl (containing 2 mM phosphate buffer pH 7) at a 10mm × 5mm ITO electrode.

Figure 4.4 shows typical voltammograms obtained with a TiO_2 FAD modified ITO electrode. In figure 4.4A cyclic voltammograms (10 consecutive cycles, scan rate 100 mVs^{-1}) obtained for a one layer TiO_2 FAD film immersed in aqueous 0.1 M KCl are shown. A reversible reduction is observed with a midpoint potential of -0.45 V vs. SCE. This reversible reduction is consistent with the reduction of FAD observed in solution and is here tentatively assigned to a 2 electron – 2 proton process[21] (see Figure 4.1). The formation of the semiquinone intermediate cannot be ruled out.

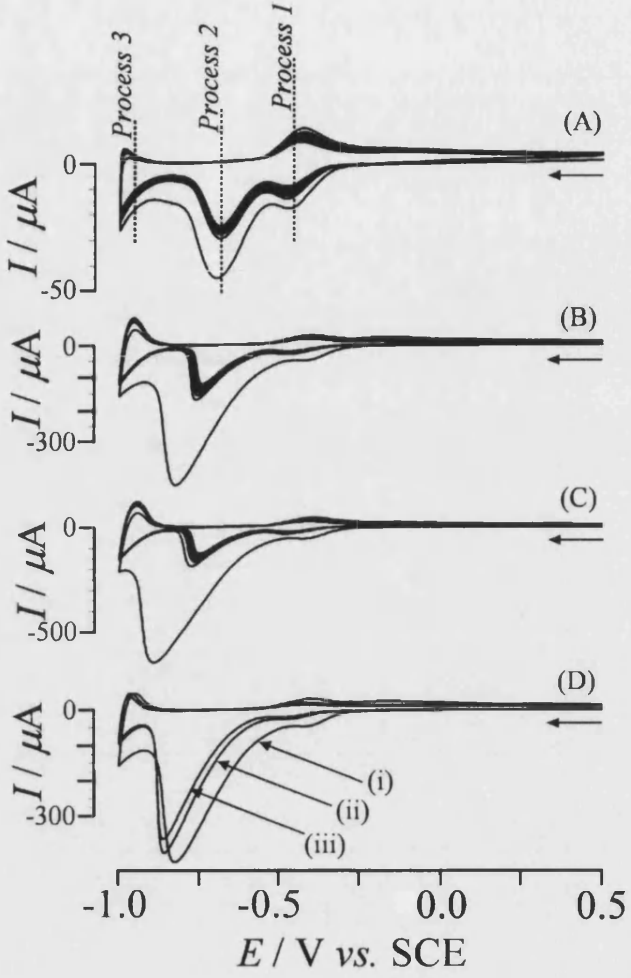

Figure 4.4 Cyclic voltammograms (scan rate 0.1 Vs^{-1}) showing the current data for the first ten potential cycles for a 10mm × 10mm ITO electrode modified with (A) 1 layer, (B) 5 layers, and (C) 8 layers of TiO_2 FAD and immersed in aqueous 0.1 M KCl solution. The repeatability of the voltammetric response for a 5 layer TiO_2 FAD electrode is shown in (D) with (i) the voltammetric response in the initial potential cycle, (ii) the initial potential cycle after a 5 minute wait with a potential of +0.5V vs. SCE applied, and (iii) after a further 5 minute wait with a potential of +0.5V vs. SCE applied. The gradual shift of the voltammetric response is believed to be due to a gradual loss of protons from the mesoporous structure.

The voltammetric signal for the surface immobilized FAD (Process 1) may be described by equation 4.1 and assumes electron transfer from ITO directly to FAD which is immobilized on the TiO_2 surface. This mechanism (probably enhanced by additional hopping conduction[24] extending across the first TiO_2 particle layer) operates only in the vicinity of the ITO electrode surface (see below). A model for this kind of conduction process at microparticle surfaces has been suggested and

treated by Schröder et al[25]. Experiments at a bare ITO electrode in the absence of TiO_2 suggest that strong adsorption of FAD occurs only at the surface of the TiO_2 particles and not at the ITO substrate.

Process 1: $FAD(TiO_2) + 2\ e^-(\text{ITO electrode}) + 2\ H^+(aq) \rightarrow FADH_2(TiO_2)$ (4.1)

A second reduction response is detected with a peak potential of -0.66 V vs. SCE (see Figure 4.4A) and this voltammetric signal appears to be essentially irreversible. By increasing the number of TiO_2 FAD layers this voltammetric response increases considerably and is consistent with the reduction of FAD immobilized in the bulk of the mesoporous TiO_2 film (see Figure 4.4A-C). This process is tentatively assigned to the FAD reduction with TiO_2 providing a conduit for electrons (equation 4.2).

Process 2: $FAD(TiO_2) + 2\ e^-(TiO_2) + 2\ H^+(aq) \rightarrow FADH_2(TiO_2)$ (4.2)

The irreversibility of the electrochemical FAD reduction may be regarded as an electronic effect based on the semi-conducting nature of TiO_2. Scanning the potential to more positive potentials does not allow the oxidation $FADH_2$ to be observed since this requires electron injection into the conduction band of TiO_2, which under these conditions appears to be kinetically slow. It is interesting to note that scanning the potential to positive potentials after formation of $FADH_2$ at the TiO_2 surface results in a considerable electrochemical potential gradient within the membrane close to the electrode surface. That is, FAD (close to the electrode surface) and $FADH_2$ (within the mesoporous TiO_2 film) are both present in close distance.

Scanning the potential to more negative potentials gives rise to a further cathodic process. This process is consistent with the reduction of Ti(IV) sites in the TiO_2 nanoparticles[26] and therefore corresponds to reversible conduction band filling accompanied by proton insertion[27] (equation 4.3). The magnitude of the voltammetric response associated with Process 3 scales with the number of TiO_2 layers deposited.

Process 3: $Ti(IV)(TiO_2) + e^-(ITO\ electrode) + H^+(aq) \rightarrow Ti(III)(TiO_2) + H^+(TiO_2)$ (4.3)

The irreversible nature of Process 2 is dramatic and it can be seen for example in Figure 4.4C that the reduction peak current associated with Process 2 is reduced in the second and consecutive potential cycles. After the initial reduction, the electrochemically accessible amount of FAD is exhausted. Experimentally, it was observed that a waiting time of ca. 5 minutes between experiments is required to fully recover the reduction response for Process 2. Figure 4.4D shows that with a 5 minute waiting time between experiments the voltammetric signal becomes fully repeatable and the electrode modified with TiO_2 FAD is stable. A minor shift in the peak position can be attributed to a small change in the concentration of protons within the membrane induced by processes at the TiO_2 surface. This kind of effect has been observed before for similar pH dependent redox systems immobilized in mesoporous TiO_2 films, and the shift in reversible potential may be regarded as a probe into the local pH at the solid | liquid interface[28]. There is no obvious effect of room light or darkness on the voltammetric data. It seems very likely that the re-oxidation is coupled to either slow exchange via very low concentrations of 'free' FAD in the pore solution or, perhaps most likely, traces of oxygen in the solution and/or slow hydrogen evolution at the TiO_2 surface[26], which would also explain the gradual shift of the voltammetric response in Figure 4.4D.

The effect of scan rate and convection/stirring in the electrochemical cell are consistent with a strongly bound FAD redox system at the surface of the TiO_2 membrane. Over a range of scan rates from 0.01 Vs^{-1} to 0.5 V s^{-1} voltammetric peaks for both Process 1 and Process 2 increase linearly with scan rate. Agitation of the solution during voltammetric experiments does not affect the shape of the current response. It is interesting to compare earlier reports of the electrochemical reduction of FAD immobilized on TiO_2 surfaces which seem to agree mainly with the characteristics of electrochemical responses observed for Process 1[20]. The observation of Process 2 can be explained based on the electronic properties of the TiO_2 FAD assembly. Figure 4.5 summarises the differences of Process 1 (occurring

in direct contact with the ITO electrode and via electron hopping) and Process 2 (occurring via electron transport within the TiO_2 structure).

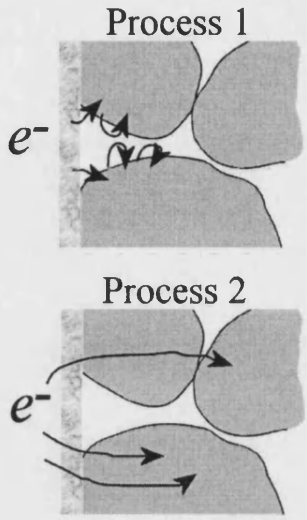

Figure 4.5 Schematic representation of the ITO electrode | TiO_2 film interface with two distinct redox processes indicated. Process 1 shows interfacial electron hopping due to FAD adsorbed onto the TiO_2 surface in the vicinity of the ITO electrode. Process 2 shows the diffusion of electrons into the TiO_2 structure which is followed by reduction of FAD adsorbed on the TiO_2 surface throughout the film.

4.3.2 Electrochemical Reactivity of Mixed TiO_2 Phytate - TiO_2 FAD Films

Next, mesoporous TiO_2 films were formed by first depositing layers of TiO_2 phytate[8] followed then by layers of TiO_2 FAD. With phytic acid as a binder, TiO_2 phytate films with typically 30 nm thickness per layer are produced. In contrast to the TiO_2 FAD films, the TiO_2 phytate films have no adsorbed redox centres and therefore contribute only to the electrochemical reduction of Ti(IV) (Process 3)[29]. Electrodes produced by modifying an ITO substrate with TiO_2 phytate film show no affinity towards FAD adsorption due to the complete coverage of the surface with the polydentate phytic acid binder. TiO_2 phytate is therefore expected to act as a 'spacer' layer between the ITO surface and the TiO_2 FAD film.

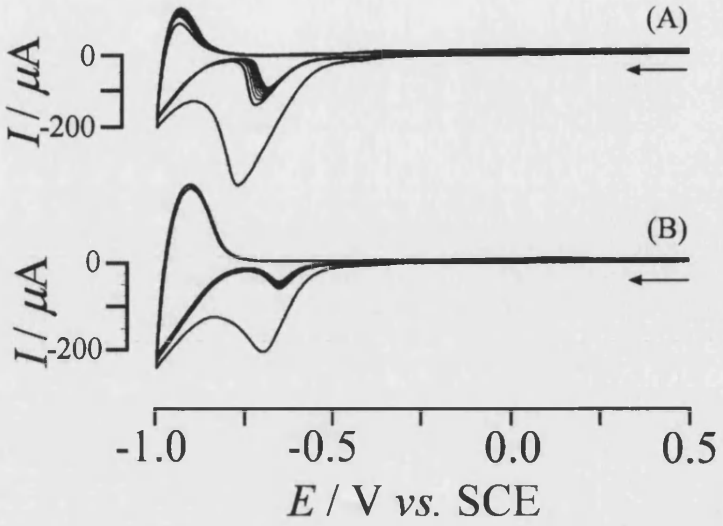

Figure 4.6 Cyclic voltammograms (scan rate 0.1 Vs^{-1}) for the reduction of immobilized FAD at layered 10mm × 10mm ITO electrodes modified with (A) 1 layer TiO_2 phytate followed by 5 layers of TiO_2 FAD and (B) 5 layers of TiO_2 phytate followed by 5 layers of TiO_2 FAD immersed in aqueous 0.1 M KCl (scans 1-10 shown).

Initially an electrode with 1 layer of TiO_2 phytate and 5 layers of TiO_2 FAD was used. In Figure 4.6 it is shown that for this type of electrode the voltammetric response associated with Process 2 is still observed, but the voltammetric response for Process 1 is almost entirely suppressed (compare Figure 4.4B). Two important conclusions from this observation are (i) the interpretation of Process 1 as occurring in direct contact with the electrode (see Figure 4.5) is correct and (ii) conduction of electrons through the TiO_2 phytate spacer film (at sufficiently negative potentials) is facile. The peak current for the reduction of FAD immobilized within the membrane is only slightly smaller compared to the peak current observed for a simple 5 layer TiO_2 FAD film (see Figure 4.4B).

Increasing the thickness of the TiO_2 phytate spacer layer has a further consequence. In Figure 4.6B voltammograms obtained with a 5 layer TiO_2 phytate – 5 layer TiO_2 FAD film are shown. It can be seen that the response for the TiO_2 based Ti(IV/III) reduction (Process 3) is further increased and the response for the FAD reduction (Process 2) is still observed. However, in the second and consecutive scans the peak current for the reduction peak at -0.66 V vs. SCE is reduced and the time it takes for the electrode to 'recover' after reduction of the immobilized FAD is increased.

Clearly, the 5 layer TiO_2 phytate film is adding a longer diffusion path and therefore, slows down the transport of electrons during both the reduction and the re-oxidation.

It is possible to exploit this effect of the spacer layer on the peak current for Process 2 to obtain an order-of-magnitude estimate for the diffusion coefficient for the electrons in the TiO_2 phytate film. The reduction in the peak current for Process 2 (in Figure 4.6) may be interpreted as a transport effect in which electrons have to travel through the TiO_2 phytate spacer film (see Figure 4.5). For a very thick film the transport of electrons through this film will dominate the voltammetric response. In this case, a simple approximation for transport across a membrane can be employed (equation 4.4). The following expressions (equations 4.5 and 4.6) approximately describe the effect of the membrane on the peak current $I_{peak,0}$ (equation 4.4) and allow an estimate for the diffusion coefficient of the electrons, $D_{electron}$, to be obtained. This estimate may be regarded as an upper limit due to the effects of film thickness imperfections.

$$I_{membrane} = \frac{FAD_{electron}c_{electron}}{\delta} \qquad (4.4)$$

$$\frac{1}{I_{peak}} = \frac{1}{I_{peak,0}} + \frac{1}{I_{membrane}} \qquad (4.5)$$

$$I_{peak} = \left(\frac{1}{I_{peak,0}} + \frac{\delta}{FAD_{electron}c_{electron}} \right)^{-1} \qquad (4.6)$$

In these expressions, $I_{membrane}$ is the transport limited current across a membrane of thickness δ, I_{peak} is the observed peak current, $I_{peak,0}$ is the peak current observed in the absence of the TiO_2 phytate spacer layer, F is Faraday's constant, A is the area of the electrode, and $D_{electron}$ $c_{electron}$ denote the diffusion coefficient and concentration of electrons in the TiO_2 phytate film in the potential range investigated. The parameter δ describes the thickness of the TiO_2 phytate spacer layer as shown in Figure 4.7A. This equation allows an approximate value for the product $D_{electron} \times c_{electron} = 8 \times 10^{-12}$ mol m^{-1} s^{-1} to be obtained from the experimental peak currents (see Figures 4.4B and 4.6B).

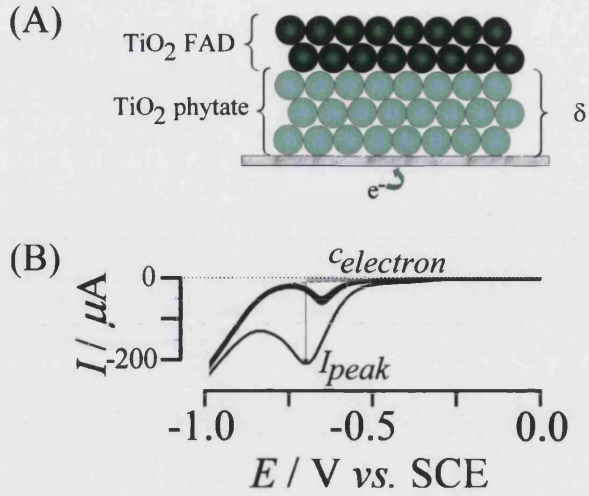

Figure 4.7 (A) Schematic representation of a layered structure with a TiO_2 phytate film and a TiO_2 FAD film subsequently deposited onto an ITO substrate electrode. The parameter δ describes the thickness of the TiO_2 phytate film. (B) Plot showing the determination of the peak current, I_{peak}, and of the concentration of electrons, $c_{electron}$.

A rough estimate for the concentration of electrons, $c_{electron}$, can be obtained from the analysis of the voltammetric signal for Process 3 in Figure 4.6B. The shape of the voltammetric response is approximately exponential and often attributed to the presence of 'trap states'[27]. By fitting an exponential curve into the cathodic part of the response for Process 3 and integration (see gray area in Figure 4.7B), the number of mobile electrons, $c_{electron}$, in the mesoporous membrane can be obtained as roughly 1-10 mM (or roughly one electron per particle). Therefore an upper limit for the diffusion coefficient can be estimated from the $D_{electron} \times c_{electron}$ value as $D_{electron} = 10^{-6}$ m^2s^{-1}. This approximate value is not inconsistent with earlier estimates of $D_{electron}$ for other types of TiO_2 structures[30] and only slightly higher than values determined for mesoporous TiO_2 in organic solvents[31]. For more accurate measurements of $D_{electron}$ a wider range of membrane thicknesses, different scan rates, and a more quantitative data analysis approach will be required.

4.3.3 Redox Mediator Currents within the Mesoporous TiO_2 FAD Membrane

The reduction of FAD immobilized on the TiO_2 surface creates a high concentration of $FADH_2$ which cannot immediately be directly re-oxidised electrochemically. The

presence of $FADH_2$ very close to the electrode surface creates a gradient of electrochemical potential within the TiO_2 membrane and it can be shown that traces of redox active materials are sufficient to 'shuttle' electrons across the nanometre wide potential gap. Experiments have been conducted with small concentrations of $Fe(CN)_6^{4-}$ added to the aqueous 0.1 M KCl electrolyte solution and a dramatic effect has been observed. Figure 4.8A shows voltammograms obtained for the reduction of a 5 layer TiO_2 FAD electrode immersed in aqueous 0.1 M KCl containing 1 μM $Fe(CN)_6^{4-}$. The oxidation of $Fe(CN)_6^{4-}$ occurs at a reversible potential of 0.18 V vs. SCE and the oxidation process is detected as a 'quasi steady state' current (Process 4). The effect increases with $Fe(CN)_6^{4-}$ concentration and levels off with more than 6 μM $Fe(CN)_6^{4-}$ present in the electrolyte solution (see Figure 4.8B).

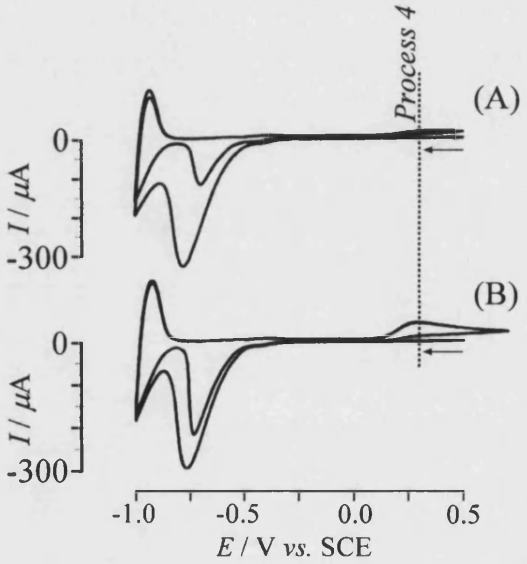

Figure 4.8 Cyclic voltammograms (scan rate 0.1 V s^{-1}) for the reduction of FAD immobilized within a 5 layer TiO_2 FAD film at a 10mm × 10mm ITO electrode immersed in aqueous 0.1 M KCl containing (A) 1 μM and (B) 6 μM $Fe(CN)_6^{4-}$. The new voltammetric response, Process 4, is consistent with a strongly amplified current signal for the oxidation of $Fe(CN)_6^{4-}$.

The effect of the indirect oxidation on the reduction response for the immobilized FAD (Process 2) can be clearly seen and the process is described by equation 4.7.

Process 4a: $Fe(CN)_6^{4-}(aq) \rightarrow Fe(CN)_6^{3-}(aq) + e^-(ITO\ electrode)$ (4.7a)

Process 4b: 2 $Fe(CN)_6^{3-}(aq)$ + $FADH_2(TiO_2)$ → 2 $Fe(CN)_6^{4-}(aq)$ + $FAD(TiO_2)$ + 2 $H^+(aq)$ (4.7b)

The current obtained during oxidation of the $Fe(CN)_6^{4-}$ mediator is orders of magnitudes higher than that expected for the simple diffusion controlled oxidation at this concentration. It is revealing to employ a simple thin layer cell model to estimate the diffusion length $\delta = \frac{nFD_{eff}Ac}{I_{lim}}$ as a function of the number of transferred electrons per mediator molecule, n = 1, Faraday's constant, F = 96487 $Cmol^{-1}$, the diffusion coefficient for the mediator, $D_{Fe(CN)_6^{4-}} = 0.65 \times 10^{-9}$ m^2s^{-1}[32], the effective diffusion coefficient D_{eff}, which is approximately related to the volume fraction of impenetrable spheres, $\phi_S \approx 0.5$, with $D_{eff} = D\frac{2(1-\phi_S)}{(2+\phi_S)}$ [33], the geometric electrode area, $A = 10^{-4}$ m^2, the concentration of mediator, $c = 1 \times 10^{-6}$ M, and the diffusion limited current, $I_{lim} = 20 \times 10^{-6}$ A (see Figure 4.8A). The resulting estimate for the diffusion length of δ = ca. 125 nm is in very good agreement with the physical dimension of the film deposit and this further supports the proposed 'shuttle' mechanism.

4.3.4 Electrochemical Reactivity of Calcined TiO_2 FAD Films

The layer-by-layer deposition allows organic-inorganic composite films to be grown where individual TiO_2 particles are separated by a molecular binder, here FAD or phytic acid. It is interesting to explore the effect of this 'binder' on the electronic properties of the film deposit. A pure TiO_2 film was prepared by multi-layer deposition of TiO_2 pyromellitate (or TiO_2 1,2,4,5-benzenetetracarboxylate). Films formed with pyromellitic acid as a binder also form layer-by-layer films with about 30 nm thickness per layer (see experimental). The resulting film was calcined in air at 500°C to give a pure TiO_2 (anatase) film without organic binder. The film was then immersed in 2 mM FAD solution in distilled water to allow FAD adsorption onto the mesoporous membrane. Figure 4.9 shows typical data from cyclic voltammetry experiments of (i) a 1 layer, (ii) a 3 layer, and (iii) a 10 layer film and the reduction of FAD (Process 1) is clearly detected at a potential of -0.45 V vs.

SCE. However, in this case the increase in the voltammetric signal with film thickness suggests that all FAD throughout the membrane is reduced and not just material in the vicinity of the electrode surface. Even more striking is that the re-oxidation of $FADH_2$ within the film appears to be still kinetically slow but more facile. It is likely that Process 1 and Process 2 have merged. Process 3 is detected as before, although the shape is broader and the onset appears to be at a more positive potential.

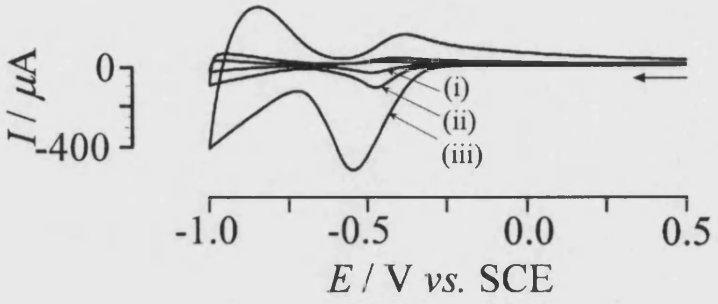

Figure 4.9 Cyclic voltammograms (scan rate 0.1 V s^{-1}) for the reduction of FAD immobilized within a TiO_2 membrane formed by depositing (i) 1 layer, (ii) 3 layers, and (iii) 10 layers of TiO_2 pyromellitate (calcined at 500°C in air followed by impregnation with FAD). The calcination process changes the electronic properties compared to those observed for the wet-assembled membranes.

The shift of the reduction Process 2 towards more positive potentials seems to imply a faster electron transfer rate constant from TiO_2 to the adsorbed FAD, which could be explained by a higher concentration of electrons $c_{electron}$ (and holes c_{holes}) within the mesoporous structure. This would also allow the more facile re-oxidation of $FADH_2$ to be explained and it agrees with the broader shape of the response for Process 3. It is likely that the potential dependent concentration of electrons, $c_{electron}$, possibly also their mobility, $D_{electron}$, or changes in the surface dipole of the TiO_2 | aqueous electrolyte interface have been affected by the calcination process, e.g. by the removal of the binder between individual particles. However, more work will be required to confirm this speculation and to provide a more quantitative mechanistic description for redox processes in these mesoporous TiO_2 films.

4.4 Conclusions

It has been shown that films of TiO_2 FAD can be deposited layer-by-layer in a simple dip coating approach. The immobilized FAD is electrochemically active throughout the film and is readily reduced electrochemically. The re-oxidation is kinetically inhibited. The re-oxidation may occur chemically or a trace amount of a solution phase redox mediator such as $Fe(CN)_6^{4-}$ can be employed to electrochemically oxidize $FADH_2$ back to FAD. An electronic difference has been observed for TiO_2 films which are self-assembled with an organic binder molecule and films of pure TiO_2 formed after calcination of TiO_2 pyromellitate.

4.5 References

[1] See for example Varghese, O.K.; Grimes, C.A. *J. Nanosci. Nanotechnol.*, **2003**, *3*, 277.

[2] Peter, L.M.; Duffy, N.W.; Wang, R.L.; Wijayantha, K.G.U. *J. Electroanal. Chem.*, **2002**, *524*, 127.

[3] Durrant, J.R.; Haque, S.A.; Palomares, E. *Coord. Chem. Rev.*, **2004**, *248*, 1247.

[4] Bisquert, J.; Cahen, D.; Hodes, G.; Ruhle, S.; Zaban, A. *J. Phys. Chem. B*, **2004**, *108*, 8106.

[5] Cummins, D.; Boschloo, G.; Ryan, M.; Corr, D.; Rao, S.N.; Fitzmaurice, D. *J. Phys. Chem. B*, **2000**, *104*, 11449.

[6] See for example Yu, J.C.; Yu, J.G.; Tang, H.Y.; Zhang, L.Z. *J. Mater. Chem.*, **2002**, *12*, 81.

[7] Fujishima, A.; Hashimoto, K.; Watanabe, T. *TiO_2 Photocatalysis*, BKC Inc., Tokyo, 1999.

[8] McKenzie, K.J.; Marken, F. *Langmuir*, **2003**, *19*, 4327.

[9] McKenzie, K.J. Ph.D. Thesis, Loughborough University, Loughborough 2004.

[10] Stott, S.J.; Mortimer, R.J.; McKenzie, K.J.; Marken, F. *The Analyst*, **2005**, *130*, 358.

[11] Dryhurst, G. *Electrochemistry of biological molecules*, Academic Press, New York, 1977.

[12] Massey, V. *Biochem. Soc. Trans.*, **2000**, *28*, 283.

[13] See for example Testa, B. *Biochemistry of Redox reactions*, Academic Press, London, 1995.

[14] For a review see Dryhurst, G. *Electrochemistry of Biological Molecules*, Academic Press, New York, 1977, 365.

[15] Shinohara, H.; Grätzel, M.; Vlachopoulos, N.; Aizawa, M. *Bioelectrochem. Bioenergetics*, **1991**, *26*, 307.

[16] Ivanova, Y.N.; Karyakin, A.A. *Electrochem. Commun.*, **2004**, *6*, 120.

[17] Karyakin, A.A.; Ivanova, Y.N.; Revunova, K.V.; Karyakin, E.E. *Anal. Chem.*, **2004**, *76*, 2004.

[18] Lin, K.C.; Chen, S.M., *J. Electroanal. Chem.*, **2005**, *578*, 213.

[19] See for example Yang, Y.H.; Yang, M.H.; Wang, H.; Tang, L.; Shen, G.L.; Yu, R.Q. *Anal. Chim. Acta,* **2004**, *509*, 151.

[20] Kubota, L.T.; Gorton, L.; Roddick-Lanzilotta, A.; McQuillan, A.J. *Bioelectrochem. Bioenergetics*, **1998**, *47*, 39.

[21] Garjonyte, R.; Malinauskas, A.; Gorton, L. *Bioelectrochem.*, **2003**, *61*, 39.

[22] McKenzie, K.J.; Marken, F.; Gao, X.; Tsang, S.C.; Tam, K.Y. *Electrochem. Commun.* **2003**, *5*, 286.

[23] Cabe, M.; Smith, E.T., *Anal. Chim. Acta*, **2005**, *537*, 299.

[24] Bond, A.M.; Colton, R.; Daniels, F.; Fernando, D.R.; Marken, F.; Nagaosa, Y.; Vansteveninck, R.F.M.; Walters, J.N., *J. Am. Chem. Soc.*, **1993**, *115*, 9556.

[25] Schröder, U.; Oldham, K.B.; Myland, J.C.; Mahon, P.J.; Scholz, F., *J. Solid State Electrochem.*, **2000**, *4*, 314.

[26] Marken, F.; Bhambra, A.S.; Kim, D.H.; Mortimer, R.J.; Stott, S.J. *Electrochem. Commun.*, **2004**, *6*, 1153.

[27] Fabregat-Santiago, F.; Mora-Sero, I.; Garcia-Belmonte, G.; Bisquert, J. *J. Phys. Chem. B*, **2003**, *107*, 758.

[28]Paddon, C.A.; Marken, F. *Electrochem. Commun.* **2004**, *6*, 1249.

[29] McKenzie, K.J.; Marken, F.; Oyama, M.; Gardner, C.E.; Macpherson, J.V. *Electroanalysis*, **2004**, *16*, 89.

[30] See for example Cass, M.J.; Qiu, F.L.; Walker, A.B.; Fisher, A.C.; Peter, L.M. *J. Phys. Chem. B*, **2003**, *107*, 113.

[31] Greijer Agrell, H.; Boschloo, G.; Hagfeldt, A. *J. Phys. Chem. B*, **2004**, *108*, 12388.

[32] Adams, R.N. *Electrochemistry at solid electrodes*, Marcel Dekker, New York, 1969.

[33] Cussler, E.L. *Diffusion*, Cambridge University Press, Cambridge, 1997.

5. Electrocatalytic Co-oxidation of Water and Nitric Oxide at TiO_2-Au Nanocomposite Film Electrodes

5.1 Introduction

The formation of TiO_2–gold nanocomposites[1] or cermets[2] has been reported previously based on sol-gel methods[3], sol adsorption processes[4], sputter coating[5], and with TiO_2 nanotube materials[6]. The resulting nanocomposite materials are of considerable interest due to optical effects and in heterogeneous catalysis where the TiO_2-gold nanocomposite allows low temperature oxidation of carbon monoxide[7,8], mild hydrogenation processes[9], and a range of photocatalytic reactions[10].

Metal nanoparticle arrays at electrode and sensor surfaces are of considerable interest[11]. Gold nanoparticles have been employed in nanostructured assemblies[12] and attached to electrode surfaces for example by seed growth methods[13]. Gold nanoparticle systems have been applied in electrocatalysis for example for the determination of arsenic(III)[14], have been incorporated into biosensor devices[15], and have found a wide range of applications in assemblies for catalysis[16]. A deposition and size tuning approach for gold nanoparticles on mercapto-modified surfaces has been developed[17]. Charge transfer and tunnelling effects have been investigated at gold nanoparticle decorated electrode surfaces[18]. In this chapter a simple method for the formation of structured TiO_2-Au composite films is developed.

Nitric oxide, NO, is an important short lived intermediate in many biological systems [19] and the in situ detection of low level NO in complex matrices remains a challenge. Monitoring of NO with electrochemical sensors has been achieved at carbon nanostructure electrodes[20], with nickel phthalocyanine complexes[21], iron porphyrinato complexes[22,23], nickel porphyrinato complexes[24], with proteins such as cytochrome *c*[25] or hemoglobin[26,27,28] immobilised at electrode surfaces. The mechanism of the reduction and oxidation of NO has been studied at platinum and a range of other metal surfaces[29]. For the oxidation of NO on gold in 0.1 M H_2SO_4, poor reproducibility and a complex mechanism have been reported[34]. Weak

interaction of NO with the gold surface is believed to lead to the first one-electron transfer process which is followed by hydrolysis of NO^+ to nitrite. In a second redox step the nitrite intermediate is oxidised in a two-electron process to nitrate.

The oxidation of nitric oxide has been reported at gold and gold nanoparticle electrodes[30] as well as at gold-Nafion® composite films[31]. Gold has been demonstrated to act as an electrocatalyst (when compared to tin-doped indium oxide (ITO) electrode surfaces) and gold nanoparticle assemblies have been employed as a very sensitive nitric oxide sensor in muscle cells. Recently a TiO_2-Nafion film immobilised at glassy carbon has been reported as a nitric oxide sensor electrode[32].

In this chapter a simple and versatile procedure for the formation of layered TiO_2–gold nanocomposites is reported. The resulting films are characterised and tested for the oxidation of nitric oxide in phosphate buffer solution at pH 7. A surprisingly high ("amplified") anodic current for the oxidation of nitric oxide is observed and attributed to a simultaneous oxygen evolution process catalysed by the gold nanoparticle surface in the presence of NO. A gold surface based mechanism for this electrocatalytic co-oxidation process is suggested.

5.2 Experimental

5.2.1. Chemical Reagents

Chemical reagents such as Nafion® perfluorinated ion-exchange resin (5%wt., in a mixture of lower aliphatic alcohols and H_2O), poly(diallyldimethylammonium chloride) (35%wt in H_2O), phosphoric acid (85% wt% solution in water A.C.S reagent), NaOH, KCl, nitric oxide (all Aldrich), ethanol (Fisher Scientific), tris(2,2-bipyridyl)ruthenium(II) chloride ($Ru(bipy)_3Cl_2$, Ventron, Germany) and gold colloid (20nm diameter, ca. 0.01 % in HAuCl, Sigma-Aldrich) were obtained commercially and used without further purification. TiO_2 sol (ca. 6 nm diameter, anatase, 30-35% in aqueous HNO_3, pH 0.5, TKS-202) was obtained from Tayca Corp, Japan. Solutions were prepared using deionized water with a resistivity of not less than 18 MΩ cm.

5.2.2 Instrumentation

Voltammetric experiments were performed with an Autolab PGSTAT20 system (Eco Chemie, Netherlands) in a standard three terminal electrochemical cell with a saturated calomel reference electrode, SCE, (Radiometer, Copenhagen) placed ca. 0.5 cm from the working electrode and a 2 cm × 2 cm platinum gauze counter electrode. The working electrodes were made from tin-doped indium oxide (ITO) coated glass (10 mm × 60 mm, 15 Ω per square, Image Optics, Basildon, UK). The ITO electrode was rinsed with ethanol, heat treated in a furnace (Elite Thermal Systems Ltd.) for 1 h at 500 °C, and re-equilibrated to ambient conditions prior to use. Field emission gun scanning electron microscopy (FEGSEM) images were obtained on a Leo 1530VP Field Emission Gun SEM system. Prior to voltammetric experiments solutions were de-aerated with argon (BOC). All experiments were conducted at a temperature of 22 +/- 2 °C.

5.2.3. Layer-by-Layer Formation of TiO_2 – Gold Composite Films

A layer-by-layer deposition strategy was chosen in order to prepare structured thin layer systems. Two types of electrodes were prepared with (i) only mesoporous TiO_2 and (ii) a TiO_2 – Au composite film (Figure 5.1 summarises the process).

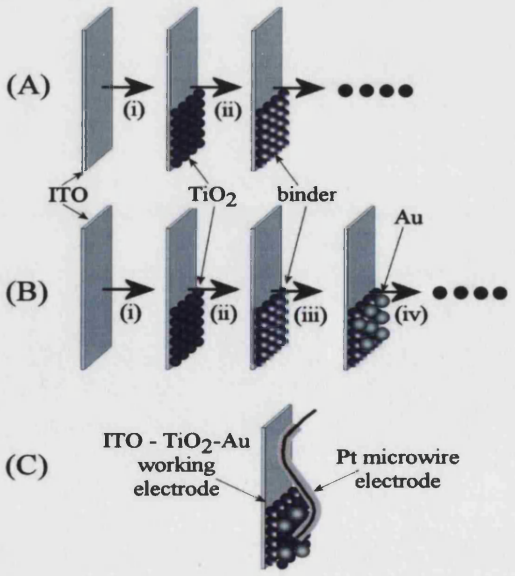

Figure 5.1 Schematic representation of (A) the layer-by-layer formation of TiO_2-Nafion® films with (i) immersion in 3wt% TiO_2 sol followed by rinsing and (ii) immersion in 3wt%

Nafion® in methanol followed by rinsing with methanol and with water. (B) Layer-by-layer formation of a TiO_2-Au structure with (i) and (ii) as above, (iii) immersion in aqueous 0.3w% PDDACl followed by rinsing and immersion into 20 nm Au sol (0.01%) and rinsing, and (iv) immersion into 0.3wt% PDDACl followed by rinsing and immersion into 0.5wt% Nafion in methanol. This four-step cycle may be repeated to create TiO_2-Au multi-layer films. (C) A two-electrode arrangement with a ITO-TiO_2-Au generator electrode in close vicinity to a 50 μm diameter platinum wire (Teflon coated) collector electrode.

The deposition procedure for the mesoporous TiO_2 electrode consisted of a sequence of liquid immersion steps with (i) a TiO_2 sol (6 nm diameter, 3%wt in nitric acid, pH ca. 2) for 60 seconds followed by rinsing with distilled water and drying in air, (ii) dipping into Nafion® anionomer solution (ca. 0.5 wt% in methanol) for ~10 seconds followed by rinsing with distilled water. This completed a single layer deposition for the simple TiO_2-Nafion film and the cycle was repeated to add more layers. After deposition of the required number of layers the electrodes were calcined at 500°C in air for 1 hour to leave a purely inorganic mesoporous anatase film.

The deposition of the TiO_2–Au nanocomposite film involved the same sequence of dipping steps as mentioned above with additional steps (iii) dipping into poly(diallyldimethylammonium chloride) solution (ca. 0.3 wt% in H_2O) for ~10 seconds followed by rinsing with distilled water, (iv) soaking in the 20nm gold colloid for 30 minutes followed by rinsing with distilled water and drying in air. Before the next layer of the TiO_2 – Au nanocomposite can be added, the electrode is dipped once again into the poly(diallyldimethylammonium chloride)(PDDAC) solution for ~10 seconds, rinsed with water and then dipped into Nafion solution for ~10 seconds and rinsed with water. This completes a single layer TiO_2-Au deposition. The deposition steps are repeated to increase the thickness of the film. After the deposition of the required number of layers the electrodes are calcined in air at 500°C for 1 hour. A typical SEM image of a TiO_2-Au nanocomposite film is shown in Figure 5.2. The thickness of the film is approximately 30 to 50 nm per layer after calcination. Well-spaced gold nanoparticles are embedded into the TiO_2 matrix and most exhibit a 20 nm diameter. Some particles appear to have an increased diameter due to merging of two closely spaced particles under high temperature conditions. However, most particles in the TiO_2 matrix appear to avoid

sintering or coalescence which is also confirmed by the red colour of the calcined TiO_2-Au nanocomposite film.

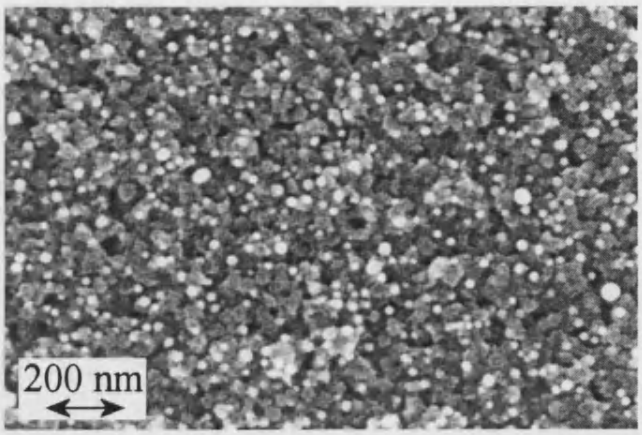

Figure 5.2 FEGSEM image of the surface of a calcined TiO_2-Au film deposit. Bright particles correspond to Au nanoparticles distributed evenly throughout the structure.

5.2.4. Nitric Oxide Solution Preparation and Detection Procedure

A nitric oxide saturated solution (ca. 1.8 mM in NO[33]) was prepared by bubbling pure NO gas through 10 mL deoxygenated deionised water for 30 minutes. All parts of the apparatus were thoroughly degassed with argon prior to use and during the procedure a constant flow of argon was kept over the solution, as NO rapidly reacts with O_2. The resulting solution of NO was used as a stock solution and aliquots transferred into the reaction cell (under argon) via glass syringe. NO determination experiments were conducted in a 30 mL electrochemical cell.

5.3 Results and Discussion

5.3.1. Formation and Electrochemical Characterisation of Mesoporous TiO_2-Au Thin Film Electrodes

Thin films of TiO_2 are readily deposited onto tin-doped indium oxide (ITO) substrates employing a layer-by-layer procedure[34]. The binding of the positively charged 6 nm diameter TiO_2 nanoparticles onto ITO is believed to be governed by an

electrostatic interaction[35] and a Nafion® anionomer is employed here to allow continuous deposition in a layer-by-layer manner (see experimental section 5.2.3). When followed by electrochemistry, the layer-by-layer growth of the TiO_2-Nafion film can be readily observed based on the characteristic reduction of Ti(IV) observed at ca. -0.6 V vs. SCE (see Figure 5.3A). Shown here is the voltammetric response for the calcined film (see experimental section 5.2.3) free of organic material and immersed in de-aerated 0.1 M KCl.

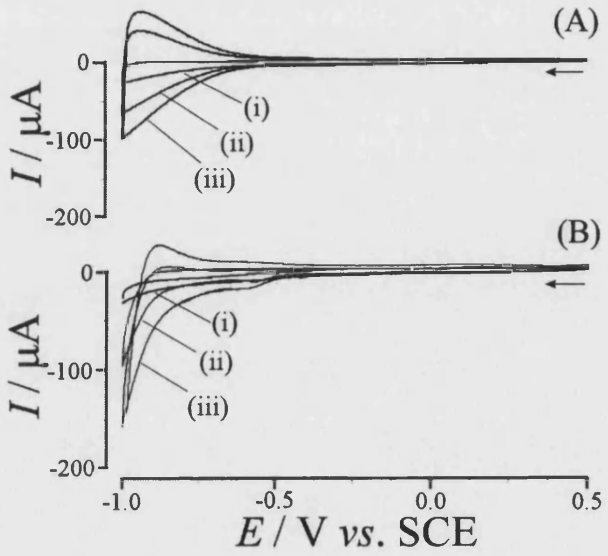

Figure 5.3. (A) Cyclic voltammograms (scan rate 100 mVs^{-1}) for the reduction and re-oxidation of a 1, 3, and 5 layer TiO_2 deposit (prepared with a Nafion binder and calcined at 500 °C in air) on an ITO electrode immersed in aqueous 0.1 M KCl. (B) Cyclic voltammograms for a 1, 3, and 5 layer TiO_2- Au nanocomposite electrode obtained under the same conditions.

Each layer of TiO_2 adds to the signal, and measurements by AFM (not shown) confirm an average increase of film thickness by about 25 nm per deposition cycle. It is interesting to introduce further components into this kind of layered nanostructure and in particular catalytic metal centres are of interest. The deposition procedure was further developed and the Nafion® layer was followed by the deposition of a cationomer, PDDAC (see experimental section 5.2.3). This cationomer layer then allows gold nanoparticles (nominal 20 nm diameter) to be adsorbed onto the surface. The cycle is completed by additional layers of PDDAC and a layer of Nafion. Repeating this sequence allows a well-defined nanocomposite, TiO_2-Au, to be deposited in variable thickness. Typical voltammetric responses for this kind of film

after calcination are shown in Figure 5.3B. It can be observed that the reduction of Ti(IV) still occurs, but it occurs as a much more irreversible process due to more facile hydrogen evolution on gold.

In order to directly observe the voltammetric response for the gold nanoparticles immobilised in this structure, experiments were conducted in 0.1 M phosphate buffer at pH 7. Under these conditions, a characteristic oxidation and re-reduction response for the gold nanoparticles is obtained (see Figure 5.4A). Each TiO_2-Au deposition cycle adds to the gold response which implies at least partial conductivity through the TiO_2-Au composite film. From the SEM image (see Figure 5.2) it can be seen that the distribution of Au nanoparticles is homogeneous but sparse and some particles may well be out of tunnelling range. A plot of the charge under the cathodic gold response versus the number of layers is shown in Figure 5.4B. It can be seen that an increase in the gold signal even occurs for 10 layer deposits (curve i) but the expected trend estimated based on the SEM image (curve ii) clearly indicates that more gold is present. The additional gold is observed electrochemically when a suitable redox shuttle, e.g. $Ru(bipy)_3^{3+/2+}$ is employed (see Figure 5.4C). A very low concentration of $Ru(bipy)_3^{2+}$ allows the remaining gold surface to be oxidised indirectly and determined. The additional current increases with the number of TiO_2-Au layers.

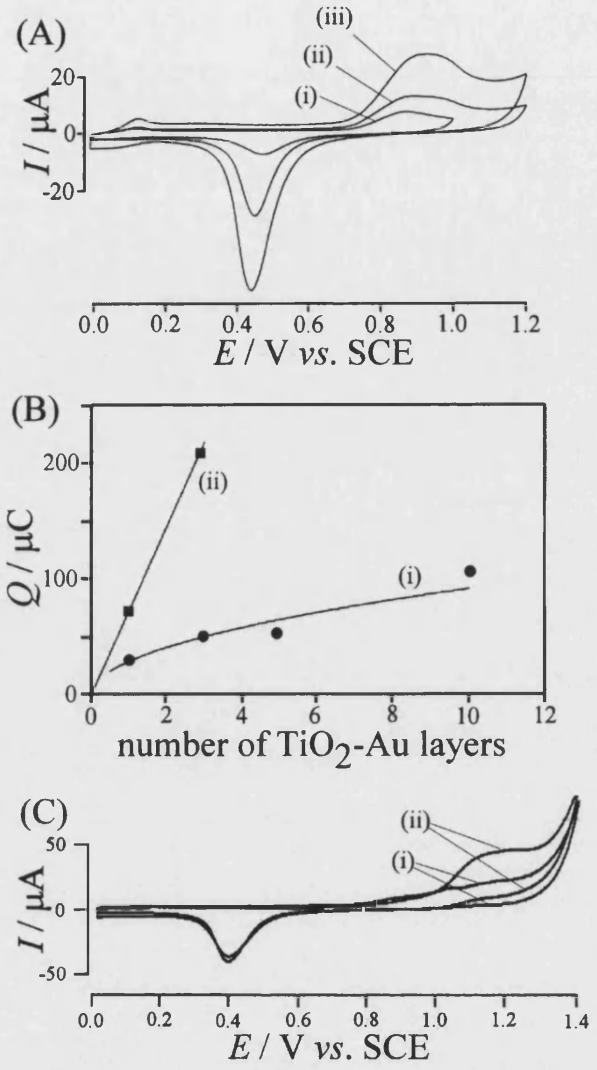

Figure 5.4. (A) Cyclic voltammograms (scan rate 100 mVs^{-1}) for the oxidation and re-reduction of a (i) 1, (ii) 3, and (iii) 10 layer TiO_2-Au film deposit (1 cm^2) immersed in aqueous 0.1 M phosphate buffer pH 7. (B) Plot of the charge under the characteristic gold reduction peak versus the number of TiO_2-Au layers (i) and a plot of the expected charge estimated based FEGSEM images (ii) (see Figure 5.2). (C) Cyclic voltammograms (scan rate 100 mVs^{-1}) for the oxidation and re-reduction of a 5 layer TiO_2-Au electrode immersed in 0.1 M phosphate buffer pH 7 (i) in the absence and (ii) in the presence of 6 μM $Ru(bipy)_3^{2+}$.

The real surface area of the gold nanoparticles directly connected to the electrode surface can be obtained by comparison of the voltammetric response with those obtained at a 1.6 mm diameter gold disk electrode in 0.1 M phosphate buffer (charge ca. 1200 μC cm^{-2}). Based on this value the 10 layer TiO_2-Au nanocomposite electrode exhibits an active gold surface of below 0.1 cm^2, a tenth of the geometric surface area.

5.3.2. The Electrocatalytic Oxidation of NO and Nitrite at Mesoporous TiO_2 – Au Nano-composite Thin Film Electrodes

The novel TiO_2-Au nanocomposite film electrode has a well-defined structure and is reconditioned after use simply by calcination at 500 °C in air. In order to explore the electrochemical reactivity of these film electrodes, the oxidation of nitric oxide and nitrite are investigated as important chemical, environmental[36], and biological analytes[37]. Nitric oxide as well as nitrite are known to undergo facile oxidation on gold surfaces[34] and in particular on gold nanostructures[35].

Figure 5.5 shows cyclic voltammetry data for the oxidation of 60 μM NO at a 1.6 mm diameter gold disc electrode (curve ii) and at a 10 layer TiO_2-Au nanocomposite electrode (curve iv). The peak currents expected for these processes can be predicted based on the Randles-Sevcik expression (assuming a reversible electron transfer process at a uniformly accessible planar electrode[38]; equation 5.1).

$$I_p = 0.446nFAc\sqrt{\frac{nFvD}{RT}} \qquad (5.1)$$

In this equation the anodic peak current, I_p, is related to the number of electrons transferred per molecule diffusing to the electrode surface, n (here n = 3 for the oxidation of NO to NO_3^-), the Faraday constant, F, the electrode area, A, the concentration, c (here 0.06 mM) , the scan rate, v, the diffusion coefficient, D (the literature value is 1.9×10^{-9} m^2s^{-1} at 293 K[39]), the gas constant, R, and the absolute temperature, T = 295 K. For a 1.6 mm diameter gold disk electrode and for a 1 cm^2 TiO_2-Au electrode the predicted peak currents are 2.3 μA and 116 μA, respectively. The observed peak current at a 1.6 mm diameter is approximately 14 μA (estimated by subtracting curve i from curve ii in Figure 5.5) and therefore approximately 6 fold increased when compared to the expected current. The current observed at the 10-layer TiO_2-Au electrode, 670 μA, is apparently increased by a similar factor. However, the ratio of the gold surface signal to the nitric oxide oxidation signal is much more dramatic for the TiO_2-Au nanostructure and therefore an enhanced

oxidation response is obtained in spite of a much reduced (one order of magnitude) gold surface area.

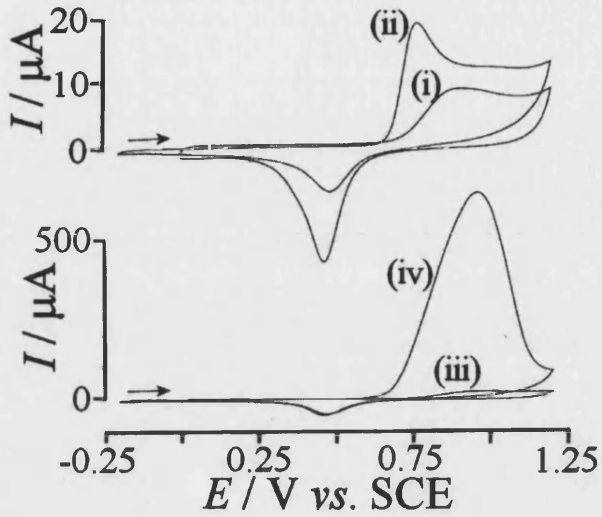

Figure 5.5. Cyclic voltammograms (scan rate 100 mVs^{-1}) obtained at (i, ii) a 1.6 mm diameter gold disc electrode and (iii, iv) a 1 cm^2 10 layer TiO_2-Au electrode immersed in aqueous 0.1 M phosphate buffer solution. Voltammograms (i) and (iii) have been obtained in the absence of NO and (ii) and (iv) in the presence of 60 μM NO.

In order to further study this NO oxidation response, the oxidation of nitrite was considered. Figure 5.6A shows a set of voltammograms obtained at a 10 layer TiO_2-Au electrode immersed in 0.1 M phosphate buffer solution at pH 7. The addition of nitrite clearly results in a well-defined anodic current response. The peak current for this oxidation response (see Figure 5.6A) is only slightly lower compared to that expected for the 2 electron process described by equation 5.2 (based on equation 5.1, assuming a diffusion coefficient of ca. $D(NO_2^-) = 1.8 \times 10^{-9}$ m^2s^{-1}[40]).

$$NO_2^-(aq) + H_2O \rightleftharpoons NO_3^-(aq) + 2\,H^+(aq) + 2\,e^- \qquad (5.2)$$

The peak current for the nitrite oxidation (2 electron transfer) at the 10 layer TiO_2-Au electrode is approximately one order of magnitude smaller when compared to the anodic peak current for the same concentration NO oxidation (nominally 3 electron) and therefore an additional process must be occurring. Figure 5.6B shows that this enhanced peak current is sensitive to the amount of gold present and that the increase in peak current is consistent with the increase in active gold nanoparticle surface

(compare Figure 5.4A). Figure 5.6C and 5.6D demonstrate that the peak current is directly proportional to the concentration of NO in the aqueous phosphate buffer solution. In order to explain the unusually high anodic currents observed for the NO oxidation an additional oxidation process has to be proposed and it is plausible that oxygen evolution occurs as part of the process (equation 5.3 to 5.7).

$$NO(aq) \rightleftharpoons NO(Au) \quad (5.3)$$

$$NO(Au) \rightleftharpoons NO^{+}(Au) + e^{-} \quad (5.4)$$

$$NO^{+}(Au) \rightleftharpoons NO^{+}(aq) \quad (5.5)$$

$$NO^{+}(aq) + H_2O \longrightarrow NO_2^{-}(aq) + 2\ H^{+}(aq) \quad (5.6)$$

$$2\ NO^{+}(Au) + 2\ OH^{-}(Au) \rightleftharpoons 2\ NO(Au) + O_2(aq) + 2\ H^{+}(aq) + 2e^{-} \quad (5.7)$$

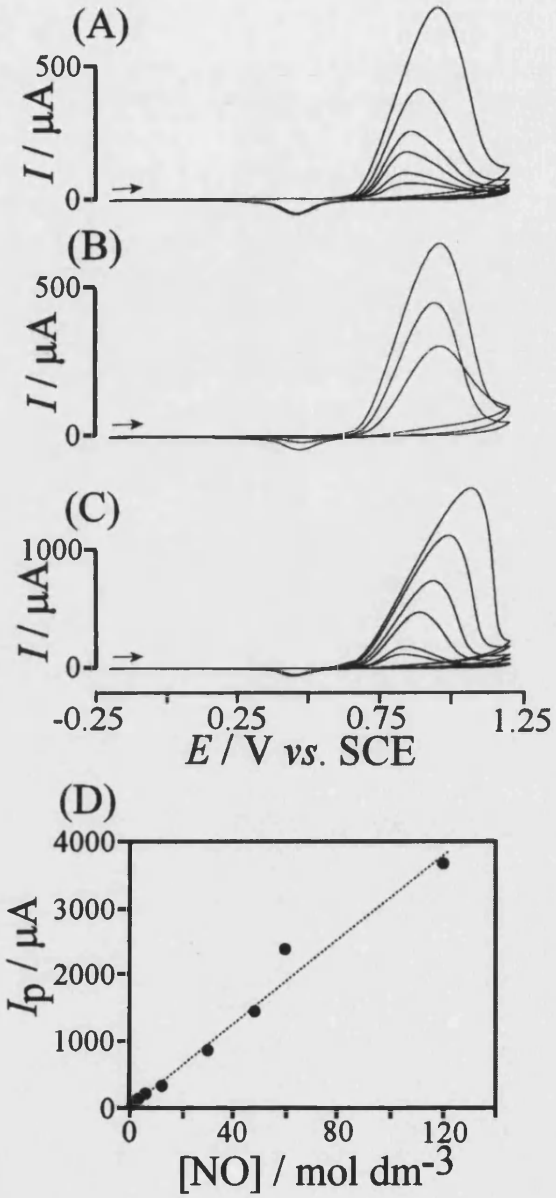

Figure 5.6. (A) Cyclic voltammograms (100 mVs^{-1}) obtained at a 10 layer TiO_2-Au electrode immersed in aqueous 0.1 M phosphate buffer pH 7 with addition of nitrite (60, 120, 240, 360, 600, 1200 μM). (B) Cyclic voltammograms (scan rate 100 mVs^{-1}) for the oxidation of 60 μM NO in 0.1 M phosphate buffer pH 7 at a 1, 3, and 10 layer TiO_2-Au electrode. (C) Cyclic voltammograms (100 mVs^{-1}) obtained at a 10 layer TiO_2-Au electrode immersed in aqueous 0.1 M phosphate buffer pH 7 with addition of NO (6, 12, 30, 48, 60, 120 μM). (D) Plot of the peak current obtained at a 10 layer TiO_2-Au electrode versus NO concentration.

5.3.3. The Electrocatalytic Co-Oxidation of NO and water at Mesoporous TiO_2 – Au Nano-composite Thin Film Electrodes

Next, a generator-collector experiment was carried out with the TiO_2-Au generator and a 50 μm diameter platinum microelectrode (coated in Teflon) acting as the collector. The platinum electrode is placed in close vicinity of the 10 layer TiO_2-Au electrode and cyclic voltammograms are recorded in the presence of 60 μM NO (see figure 5.1C). The potential of the platinum collector electrode is -0.5 V vs. SCE and a strong reduction response is observed during the anodic NO oxidation process (see Figure 5.7A).

In order to identify the collector response the experiment was repeated with a potential bias from -0.5 to +0.1 V vs. SCE (see Figure 5.7D) and from data in figure 5.7D it can be seen that a pseudo-voltammogram for the reduction of oxygen (in the potential range 0.0 to -0.4 V vs. SCE) and for the reduction of protons (at potentials negative of -0.4 V vs. SCE) is obtained. The analysis of the peak currents is shown in Figure 5.7C. Anodic peak currents obtained at the TiO_2-Au electrode do not scale with scan rate or with the square root of scan rate but the cathodic peak current observed at the platinum collector electrode appears to change linearly with scan rate.

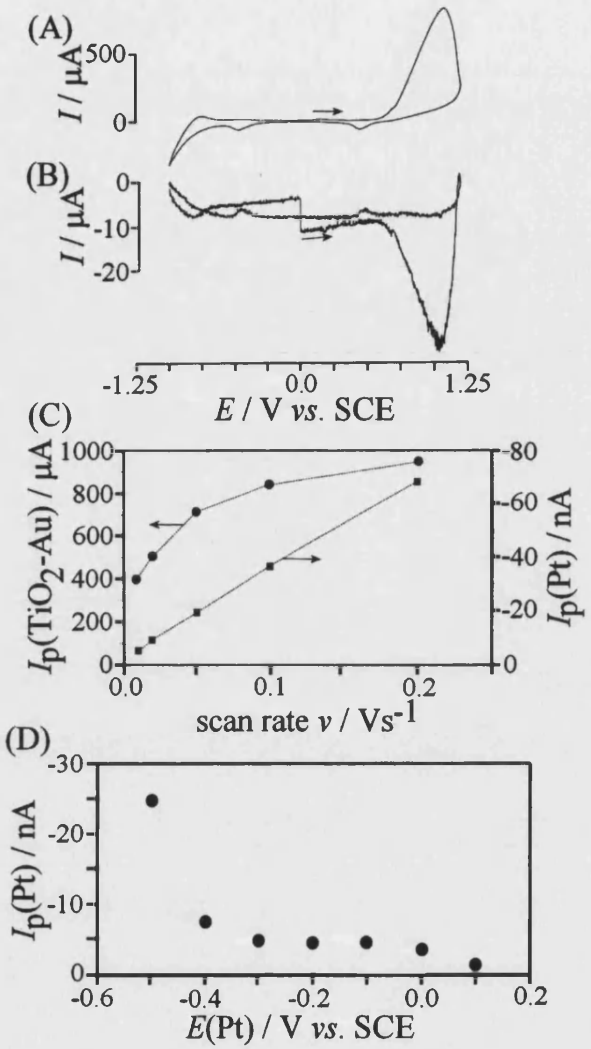

Figure 5.7. (A) Cyclic voltammogram (scan rate 100 mVs^{-1}) for the oxidation of 60 μM NO in 0.1 M phosphate buffer pH 7 at a 10 layer TiO_2-Au generator electrode. (B) Current detected at a 50 μm diameter Pt (coated in Teflon) electrode in the vicinity of the TiO_2-Au electrode (see Figure 1C) with a constant potential bias of -0.5 V vs. SCE. (C) Plot of the peak current at the TiO_2-Au generator electrode (left axis) and at the Pt collector electrode (right axis) versus scan rate. (D) Plot of the peak current observed at the Pt collector electrode as a function of potential bias.

A further important insight into why the current at the TiO_2-Au anode is relatively high is obtained in a further experiment. The phosphate buffer concentration was varied from 0.2 M, 0.1 M, 0.05 M, to 0.02 M and in the presence of 12 μM NO a dramatic change in voltammetric response was observed (data not shown). With a lower buffer concentration the peak currents are smaller and this implies that the formation of protons (as observed at the collector electrode) causes a localised

decrease in pH. The high local acid concentration then inhibits the electrode process. Additional experiments conducted with only gold particles immobilised on ITO in the absence of TiO_2 gave similar current peaks which clearly suggests that here TiO_2 acts only as an inert matrix. Experiments in the absence of phosphate buffer (in 0.1 M $NaClO_4$) also allowed similar currents for the oxidation of NO on gold nanoparticles to be observed which indicates that phosphate anions are not directly involved in this process.

In order to further resolve the mechanistic details for this electrode process additional experimental work (e.g. employing spectroelectrochemical methods) will be required. However, the observation of the amplified anodic response for NO in a physiologically relevant environment could be of considerable value and this type of novel electrode may find application in sensor systems.

5.4 Conclusions

Electrostatic deposition of layered thin films of TiO_2 with a Nafion® polyelectrolyte binder was demonstrated and the incorporation of gold nanoparticles was achieved with a complementary poly-(diallyldimethylammonium chloride) polyelectrolyte binder. After calcination mesoporous inorganic films were obtained. Although only a part of the gold deposit was directly electrically connected to the electrode, electronic conduction via gold nanoparticles was demonstrated even in a potential range where TiO_2 is electrically insulating. In spite of a relatively low real gold electrode area, a strong catalytic effect for the amplified oxidation of nitric oxide was observed and the process responsible identified as the co-oxidation of water.

5.5 References

[1] M. Chen, Y. Cai, Z. Yan, D.W. Goodman, *J. Am. Chem. Soc.*, 2006,**128**, 6341.

[2] X. Quelin, M. Lemal, S.L. Gomez, A. Bourdon, *Eur. Phys. J.* D, 2004, **30**, 217.

[3] X.H. Liu, Y.B. Fu, Y. Xie, Y. Deng, Z.J. Zhong, X. Liang, *Chin. J. Catal.*, 2006, **27,** 532.

[4] L. Armelao, D. Barreca, G. Bottaro, A. Gasparotto, S. Gross, C. Maragno, E. Tondello, *Coord. Chem. Rev.*, 2006, **250**, 1294.

[5] S. Liberman, X. Quelin, J. Sztern, Y. Dumont, A. Etcheberry, A. Bourdon, P. Gadenne, *Eur. Phys. J.-Appl. Phys.*, 2000, **11,** 91.

[6] B.L. Zhu, Z.M. Sui, S.R. Wang, X. Chen, S.M. Zhang, S.H. Wu, W.P. Huang, *Mater. Res. Bull.,* 2006, **41,** 1097.

[7] A.M. Venezia, F.L. Liotta, G. Pantaleo, A. Beck, A. Horvath, O. Geszti, A. Kocsonya, L. Guczi, *Appl. Catal. A-Gen.*, 2006, **310**, 114.

[8] S.H. Overbury, V. Schwartz, D.R. Mullim, W.F. Yan, S. Dai, *J. Catal.,* 2006, **241,** 56.

[9] A. Corma, P. Serna, *Science*, 2006, **313**, 332.

[10] P.K. He, M. Zhang, D.M. Yang, J.J. Yang, *Surf. Rev. Lett.,*2006, **13,** 51.

[11] A.N. Shipway, E. Katz, I. Willner, *Chem. Phys. Chem.*, **1**, 18.

[12] M.C. Daniel, D. Astruc. *Chem. Rev.*, 2004, **104,** 293.

[13] J.D. Zhang, M. Kambayashi, M. Oyama, *Electrochem. Commun.*, 2004, **6**, 683.

[14] X.A. Dai, R.G. Compton, *Anal. Sci.*, 2006, **22,** 567.

[15] S. Bharathi, M. Nogami, *Analyst,* 2001, **126**, 1919.

[16] M.C. Daniel, D. Astruc, *Chem. Rev.*, 2004, **104**, 293.

[17] W.L. Cheng, S.J. Dong, E.K. Wang, *Langmuir,* 2002, **18,** 9947.

[18] J.J. Zhao, C.R. Bradbury, S. Huclova, I. Potapova, M. Carrara, D.J. Fermin, *J. Phys. Chem. B,* 2005, **109**, 22985.

[19] A. Butler, R. Nicholson, *NO, life, death, and nitric oxide*, The Royal Society of Chemistry, Cambridge, 2003.

[20] F.H. Wu, G.C. Zhao, X.W. Wei, *Electrochem. Commun.*, 2002, **4,** 690.

[21] S.C. Chang, N. Pereira-Rodrigues, J.R. Henderson, A. Cole, F. Bedioui, C.J. McNeil, *Biosens. & Bioelectron.*, 2005, **21,** 917.

[22] J.N. Younathan, K.S. Wood, T.J. Meyer, *Inorg. Chem.*, 1992, **31,** 3280.

[23] J.P. Lei, H.X. Ju, O. Ikeda, *J. Electroanal. Chem.*, 2004, **567**, 331.

[24] S. Trevin, F. Bedioui, J. Devynck, *J. Electroanal. Chem.*,1996, **408**, 261.

[25] G.C. Zhao, Z.Z. Yin, X.W. Wei, *Front. Biosci.*, 2005, **10**, 2005.

[26] J.T. Pang, C.H. Fan, X.J. Liu, T. Chen, G.X. Li, *Biosens. & Bioelectron.*, 2003, 19, 441.

[27] C.H. Fan, G.X. Li, J.Q. Zhu, D.X. Zhu, *Anal. Chim. Acta*, 2000, **423**, 95.

[28] E. Topoglidis, C.J. Campbell, A.E.G. Cass, J.R. Durrant, *Electroanalysis,*2006, **18**, 882.

[29] A.C.A. de Vooys, G.L. Beltramo, B. van Riet, J.A.R. van Veen, M.T.M. Koper, *Electrochim. Acta,* 2004, **49**, 1307.

[30] A.M. Yu, Z.J. Liang, J.H. Cho, F. Caruso, *Nanoletters,* 2003, **3**, 1203.

[31] M. Zhu, M. Liu, G.Y. Shi, F. Xu, X.Y. Ye, J.S. Chen, L.T. Jin, J.Y. Jin, *Anal. Chim. Acta,* 2002, **455**, 199.

[32] Y.Z. Wang, C.Y. Li, S.S. Hu, *J. Solid State Electrochem.*, 2006, **10,** 383.

[33] A. Butler, R. Nicholson, *NO, life, death, and nitric oxide*, The Royal Society of Chemistry, Cambridge, 2003, p.63.

[34] K.J. McKenzie, P.M. King, F. Marken, C.E. Gardner, J.V. Macpherson, *J. Electroanal. Chem.*, 2005, **579**, 267.

[35] G. Decher, J.B. Schlenoff, *Multilayer Thin Films*, Wiley-VCH, Weinheim, 2003.

[36] D.J. McKenney, C.F. Drury, *Global Change Biol.*, 1997, **3**, 317.

[37] K.M. Miranda, *Coord. Chem. Rev.*, 2005, **249**, 433.

[38] F. Scholz, *Electroanalytical Methods*, Springer, Berlin, 2002, p.64.

[39] I.G. Zacharia, W.M. Deen, *Ann. Biomed. Engineer.*, 2005, 33, 214.

[40] R. Mills, V.M.M. Lobo, *Self-diffusion in electrolyte solutions*, Elsevier, Amsterdam, 1989.

6. Mesoporous TiO_2 Films: Electrochemical Evidence for Heme-Protein Absorption, Denaturation and Demetallation

6.1 Introduction

The incorporation of biological redox systems into mesoporous films has generated interest due to the possibility of direct electron exchange that can be achieved between the redox sites in the proteins and the mesoporous host electrode. Direct electrochemistry of redox proteins or enzymes can provide biomimetic models for fundamental studies as well as a basis for designing devices without the need for soluble electron transfer mediators[1]. There has been a wide range of approaches for the immobilisation of biological redox systems including adsorption[2], binding into 2D or 3D lipid structures[3], covalent binding[4], cast deposition of composites[5], trapping in porous matrices[6], or electrostatic binding into mesoporous films[7].

Hemoglobin or methemoglobin immobilized at electrode surfaces have often been employed as model redox systems and electrocatalysts. In studies by Rusling et al.[8,9] immobilization and electron transfer to hemoglobin was demonstrated. Siontorou et al.[10] have demonstrated the adsorption of hemoglobin into a self-assembled bilayer lipid membrane in order to produce a cyanide ion minisensor. The electrochemical properties of hemoglobin have also been investigated in clay films[11], in SiO_2[12], SnO_2[13], TiO_2 nanoparticle assemblies[14] and in DNA[15] or surfactant assemblies[16].

Hemoglobin is a protein molecule made up of four subunits[17]; each subunit containing a heme group surrounded by a polypeptide chain. The heme groups are the redox active centre consisting of an iron atom surrounded by a porphyrin ring, which is able to reversibly bind to an oxygen molecule[18]. However it is the protein element which surrounds the heme unit that controls the redox potential of the heme group and allows the oxygen binding to be reversible.

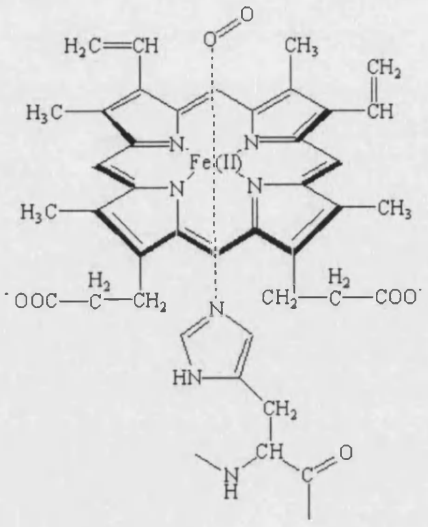

Figure 6.1 Diagram of a heme unit with oxygen bound in the 6th position.

Under unbound conditions the iron is in its +2 configuration but is easily oxidised to the +3 state, where a molecule can bind to the iron in the sixth position in the porphyrin ring (see figure 6.1). Although intended for oxygen binding, CO_2, CN^- and H_2O (methemoglobin) also bind strongly, forming the basis for sensor applications.

Previously the adsorption of hemoglobin[19] and cytochrome *c*[20,21] into mesoporous TiO_2 phytate thin films have been studied. The cytochrome *c* redox protein (diameter ca. 3.4 nm) adsorbed homogenously into the mesoporous TiO_2 film. However, the small pore sizes created from the 6 nm nanoparticle agglomerates of TiO_2 allowed the much larger hemoglobin protein (diameter ca. 6 nm) to adsorb only into the outer layer of the film[17]. It was observed that as the thickness of the film increased, a transition occurred from the hemoglobin being an electronically coupled protein to electronically insulated protein. Here the adsorption of methemoglobin is investigated by using TiO_2 films prepared with bigger 40 nm diameter particles. The larger particle size should allow adsorption of the protein into larger pores throughout the film. Previously, adsorption of hemoglobin into TiO_2-phytate hosts was carried out from a phosphate buffer solution and here initially immobilization was carried out under the same conditions. The films were probed electrochemically and perhaps surprisingly it was found that in the presence of phosphate protein denaturation and even heme demetallation are dominant processes.

6.2 Experimental

6.2.1 Reagents

Chemical reagents such as perchloric acid (70% A.C.S reagent), KCl, KOH, phosphoric acid (85% wt% solution in water, A.C.S reagent), glacial acetic acid, sodium acetate trihydrate, and EDTA were obtained commercially (Aldrich) and used without further purification. A suspension of 40 nm diameter TiO_2 (anatase) nanoparticles was prepared from a powdered form (AMT-600, Tayca Corp, Japan) 3%wt in dry methanol (Fisher Scientific, HPLC grade) by sonication (20 kHz Fisherbrand ultrasonic bath) for at least 30 minutes. Suspensions of TiO_2 in methanol were stable for several hours but underwent slow sedimentation (accelerated in the presence of water). Hemoglobin (Hb, bovine methemoglobin, H2625, from Sigma) was used without further purification. Unless stated otherwise, a 1 mg mL^{-1} Hb solution was prepared in aqueous 0.1 M phosphate buffer at pH 5.5. All solutions were prepared using deionised water with a resistivity of at least 15 MΩ cm (Elga, High Wycombe, UK).

6.2.2 Instrumentation

Electrochemical experiments were conducted with a PGSTAT 30 Autolab system (Eco Chemie, Netherlands) in a conical three-electrode cell. The counter electrode was platinum gauze and the reference electrode was a saturated calomel electrode (SCE, Radiometer). The working electrodes were prepared from tin-doped indium oxide (ITO) coated glass (10 mm x 60 mm, resistivity 15 Ω per square, Image Optics Components Ltd.). ITO electrodes were cleaned prior to film deposition by rinsing in ethanol followed by deionised water and furnace treated (Elite tube furnace) at 500°C in air for 60 minutes. For Scanning Electron Microscopy (SEM), a JEOL JSM6310 system was used. UV/Vis spectra of solution and solid samples were obtained with a Helios γ spectrometer (Thermo Electron Corp.). The temperature during all measurements was maintained at 22 ± 2 °C.

6.2.3 Procedures and Electrode Design

A suspension of the nominal 40 nm TiO_2 particles was achieved by preparing a 3 % wt solution in methanol and sonicating (see chapter section 2.2.3). A clean ITO electrode was then dipped into the white suspension for 1 minute, retracted, and the methanol was allowed to evaporate leaving behind a well-defined and uniform layer of TiO_2. The deposition process was repeated in order to build up several layers of TiO_2 particles. In this manner the required number of 'layers' of the 40 nm TiO_2 particles could be adjusted to allow variation in film thickness. The resulting film was then calcined in air at 500°C for 1 hour to improve adhesion and to remove impurities. Methemoglobin adsorption involved equilibrating the TiO_2 modified electrode in a solution of methemoglobin (1 mg mL^{-1}) prepared in aqueous 0.1 M phosphate buffer at pH 5.5, followed by rinsing in distilled water.

6.3 Results and Discussion

6.3.1. Deposition and Characterisation of Nanoparticulate TiO_2 Film Electrodes

TiO_2 nanoparticles (anatase, ca. 40 nm diameter) were deposited from a suspension (3 wt.% TiO_2) in dry methanol. After immersion and solvent evaporation, tin-doped indium oxide (ITO) electrodes are coated with a thin and uniform layer of TiO_2 which increases in thickness during each new deposition step. Once deposited, the TiO_2 nanoparticles are not re-suspended in methanol and remain permanently immobilized at the electrode surface. After formation of the multi-layer TiO_2 film at the electrode surface, a calcination step (ca. 1 h at 500°C in air) was employed to further improve adhesion. The characteristic electrochemical reduction response of the immobilized TiO_2 nanoparticles immersed in aqueous 0.1 M KCl is shown in Figure 6.2.

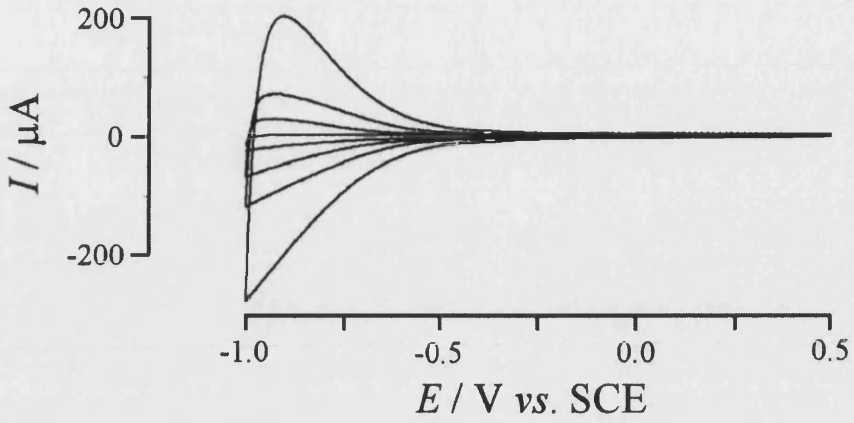

Figure 6.2 Cyclic voltammograms (scan rate 0.1 Vs^{-1}) obtained for a 1 cm^2 ITO electrode coated with a 1, 3, 5, and 10 layer films of ca. 40 nm diameter TiO_2 particles (followed by calcination) immersed in aqueous 0.1 M KCl.

The characteristic reduction process is predominantly capacitive in nature[22] and associated with the reversible formation of Ti(III) within the porous TiO_2 film[23]. From the increase in the charge under the reduction response it can be seen that the growth of the TiO_2 film is approximately proportional to the number of deposition cycles. In order to characterize the topography of the nanoparticle deposit, SEM images were obtained. Figure 6.3 shows that rather than a thin homogeneous film, a patterned film deposit of aggregates of ca. 1 μm diameter is formed. Each of the aggregates consists of smaller TiO_2 particles with ca. 40 nm diameter.

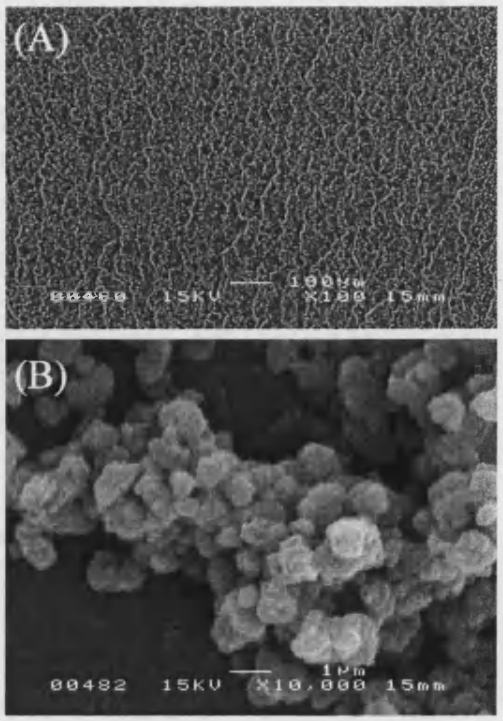

Figure 6.3 Scanning electron microscopy image (SEM) of a 10 layer deposit of TiO_2 nanoparticles (calcined) at an ITO electrode surface. Due to the deposition conditions, the nature of the "layer" is highly non-uniform.

6.3.2 Attempted Immobilization of Methemoglobin in 40nm TiO_2 Film Electrodes

TiO_2 thin film electrodes were exposed for one hour to a solution of 1 mg mL^{-1} hemoglobin in aqueous 0.1 M phosphate buffer solution (pH 5.5). Under these conditions phosphate anions immediately adsorb onto the TiO_2 surface to give a negative surface charge[24]. The positively charged protein hemoglobin (the isoelectric point is approximately 7.4[25,26]) should then be attracted into the porous oxide and thereby accumulated at the electrode surface. Figure 6.4 shows typical cyclic voltammograms obtained with this kind of electrode.

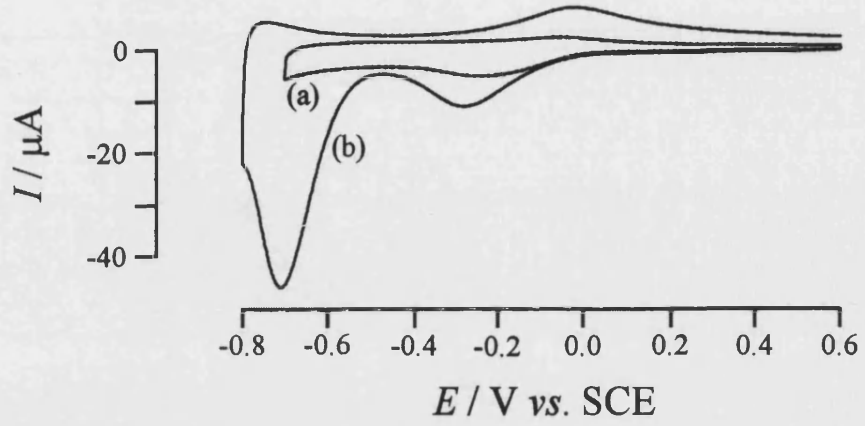

Figure 6.4 Cyclic voltammograms (scan rate 0.1 Vs^{-1}) obtained for the reduction of adsorbed methemoglobin on (a) a bare ITO electrode and (b) an ITO electrode covered with 1 layer of 40 nm diameter TiO_2 nanoparticles immersed in aqueous 0.1 M KCl. Prior to this experiment, electrodes were immersed in 1 mg mL^{-1} methemoglobin in 0.1 M phosphate buffer pH 5.5 for 1 hour.

A bare ITO electrode (see Figure 6.4a) shows only a very weak and reversible response observed at E_{mid} = -0.16 V vs. SCE. In contrast, a single layer of TiO_2 nanoparticles substantially increases this current response (see Figure 6.4b) and an additional second reduction peak is also observed at a potential of ca. -0.7 V vs. SCE. The first reduction response is clearly present for both types of films. The quasi-reversible voltammetric signal at E_{mid} = -0.16 V vs. SCE seems to be consistent with the Fe(III/II) one electron reduction of the hemin unit in methemoglobin[12,27]. At this point, the second reduction peak occurring at -0.7V vs. SCE seems also likely to be due to the Fe (III/II) couple. It is possible to speculate that the TiO_2 film has structural effects on the hemoglobin molecule, causing the reduction potential of each species to differ, however it is only in the following investigation that the true nature of the peaks are revealed (see section 6.3.3).

Next, the reduction responses for hemoglobin are investigated in more detail. Figure 6.5 shows cyclic voltammograms obtained in phosphate buffer solution (pH 5.5) for TiO_2 film electrodes with (i, ii) one layer of TiO_2 and (iii, iv) 10 layers of TiO_2.

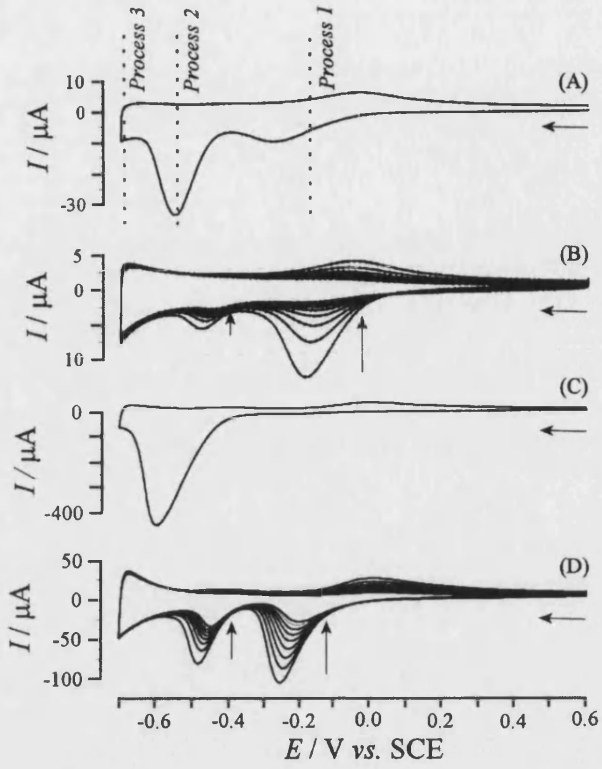

Figure 6.5 Cyclic voltammograms (scan rate 0.1 V s^{-1}) obtained for the reduction of hemoglobin immobilized in a 1 layer and in a 10 layer TiO_2 film at ITO electrodes. Voltammograms were obtained in aqueous 0.1M phosphate buffer (pH 5.5). (A) Scan 1 of 10 scans for a 1 layer TiO_2 film electrode. (B) Scans 2 to 10 for a 1 layer TiO_2 film electrode. (C) Scan 1 for a 10 layer TiO_2 film electrode. (D) Scans 2 to 10 for a 10 layer TiO_2 film electrode. Prior to voltammetric experiments, electrodes were immersed (1 h) in a solution of 1 mg mL^{-1} hemoglobin.

It is interesting to note that the magnitude of the voltammetric response for process 1 during the first potential cycle is not increased upon increasing the thickness of the TiO_2 film (see Figures 6.5i and ii). Consecutively cycling the applied potential causes this voltammetric response to decrease. For the 10 layer TiO_2 film electrode, the voltammetric signal during the first reduction for process 1 is very similar to that observed for the 1 layer TiO_2 film electrode. However, a very strong enhancement is observed in potential cycle 2 which is followed by a decay of the signal during subsequent cycles.

A second reduction (Process 2) is observed at a potential of ca. -0.5 V vs. SCE. This reduction is relatively small for 1 layer TiO_2 films but about 10-fold enhanced in the

10 layer TiO_2 film electrode. For both, 1 layer and 10 layer TiO_2 film electrode, this reduction process is pronounced only during the first reduction and gradually disappears during subsequent potential cycles.

A third reduction response observed at potentials negative of -0.6 V vs. SCE (see Figure 6.5) can be attributed to the reversible transfer of electrons into the TiO_2 host lattice. This process has been extensively studied[24] and linked to the Ti(IV/III) redox couple at the TiO_2 nanoparticle surface.

In order to explore the ability of methemoglobin to bind, experiments were conducted with a set of electrodes and in a range of different concentrations of methemoglobin. Cyclic voltammograms shown in Figure 6.6A demonstrate the effect of the methemoglobin concentration on the immobilization process. An increase in the amount of methemoglobin immobilized in TiO_2 is observed up to ca. 100 μM methemoglobin and is approximately consistent with a Langmuir adsorption isotherm (see Figure 6.6B). Next, the effect of time on the adsorption process is studied. For a 10 layer TiO_2 film electrode a considerable delay in adsorption is observed. The plot in Figure 6.6C shows that only after 10 h the process approaches completion (for a 10 layer film deposit). This rather slow adsorption process is not surprising due to the small pore size within the TiO_2 structure. It has been shown recently[17] that deposits with even smaller pore size (with 6 nm diameter TiO_2 nanoparticles) are essentially impenetrable for the methemoglobin molecules. Here, 40 nm TiO_2 nanoparticles are employed and a pore size of typically 10-20 nm can be estimated.

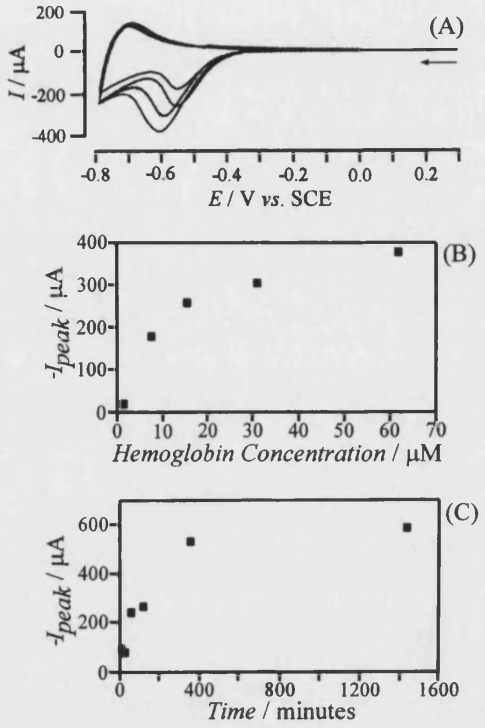

Figure 6.6 (A) Cyclic voltammograms (scan rate 0.1 V s^{-1}) for the reduction of methemoglobin immobilized in a 10 layer TiO_2 film at a 1 cm^2 ITO electrode immersed in 0.1 M phosphate buffer at pH 5.5. Prior to voltammetric experiments the electrodes were soaked for 2 h in 60 μM, 30 μM, 15 μM, and 7 μM hemoglobin in 0.1 M phosphate buffer at pH 5.5. (B) Plot of the cathodic peak current observed in the first potential cycle versus the concentration of methemoglobin during immobilization. (C) The effect of soaking time in 15 μM methemoglobin in 0.1 M phosphate buffer at pH 5.5 on the cathodic reduction peak during the first potential cycle.

Many studies have emerged in which methemoglobin is employed as an electrocatalyst. A range of processes from oxygen reduction[28], peroxide reduction[20], trichloroacetate reduction[29], and nitrite reduction[16] have been observed and attributed to the electrocatalytic effects of the porphyrinato-IX iron center. It is shown here that methemoglobin electrostatically immobilized into the TiO_2 host appears to be essentially inert toward the oxygen reduction process. Voltammograms in Figure 6.7A and 6.7B show the first and second potential cycle for electrodes in de-aerated phosphate buffer solution and in the presence of ca. 0.2 mM oxygen. Only process 3 (the formation of Ti(III)) is strongly affected by the

presence of oxygen. It is this inactivity towards oxygen that is the first indication of a problem occurring during the methemoglobin immobilization.

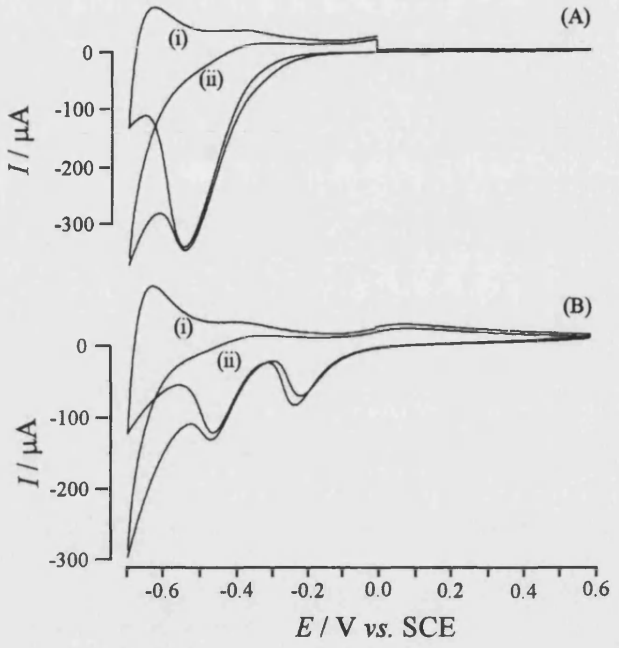

Figure 6.7. Cyclic voltammogram (scan rate 0.1 Vs^{-1}) for the reduction of methemoglobin immobilized in a 10 layer TiO_2 film electrodes and immersed in 0.1 phosphate buffer (pH 5.5). (A) Potential cycle 1 and (B) potential cycle 2 for a 10 layer TiO_2 electrode (methemoglobin immobilized by soaking for 12 h 0.1 M phosphate buffer at pH 5.5) (i) in de-aerated and (ii) non-de-aerated 0.1 M phosphate buffer solution (pH 5.5).

6.3.3 Evidence for Protein Denaturation and Demetallation

Further investigation into the voltammetric response for the reduction of methemoglobin on TiO_2 shows that not only the loss of hemin but also that complete demetallation of methemoglobin is possible. A voltammogram essentially identical to the methemoglobin response shown in figure 6.4 can be obtained by direct immobilization of Fe^{3+} into the TiO_2 film. Importantly this also shows no catalytic activity toward oxygen reduction. Figure 6.8 shows voltammograms obtained after immobilization of Fe^{3+} into a 10 layer TiO_2 film electrode.

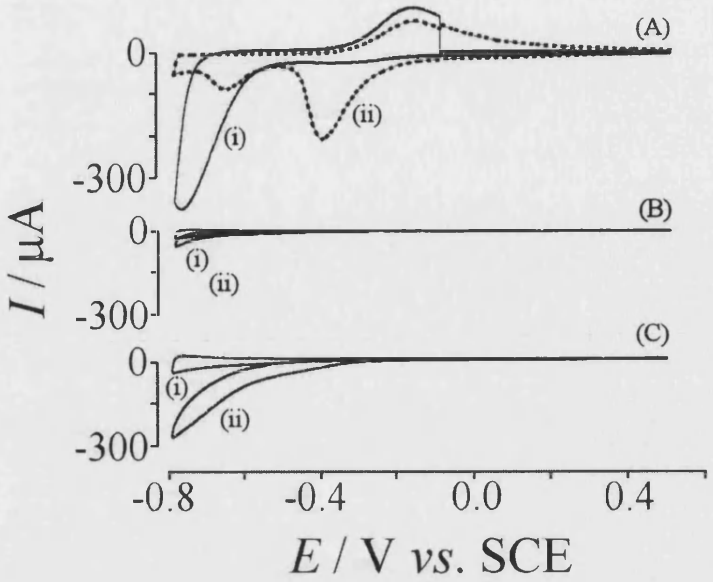

Figure 6.8. (A)(i) First potential cycle and (ii) third potential cycle for cyclic voltammograms (scan rate 0.1 V s^{-1}) obtained for the reduction of Fe^{3+} immobilized in a 10 layer TiO_2 film at ITO electrodes. Voltammograms were obtained in aqueous 0.1 M phosphate buffer (pH 5.5). Prior to voltammetric experiments, electrodes were immersed (1 h) in a solution of 60 μM Fe^{3+} in water. (B) Cyclic voltammograms (scan rate 0.1 V s^{-1}) obtained for the reduction of methemoglobin immobilized in a 10 layer TiO_2 film at ITO electrodes in the (i) absence (ii) presence of oxygen (air). Voltammograms were obtained in aqueous 0.1 M phosphate buffer (pH 5.5) containing 1 mM EDTA. Prior to voltammetric experiments, electrodes were immersed (1 h) in a solution of 1 mg mL^{-1} methemoglobin in 0.1 M phosphate buffer (pH 5.5) containing 1 mM EDTA. (C) Cyclic voltammograms (scan rate 0.1 V s^{-1}) obtained for the reduction of methemoglobin immobilized in a 10 layer TiO_2 film at ITO electrodes in the (i) absence (ii) presence of oxygen (air). Voltammograms were obtained in aqueous 0.1 M acetate buffer (pH 5.5) containing 1 mM EDTA. Prior to voltammetric experiments, electrodes were immersed (1 h) in a solution of 1 mg mL^{-1} methemoglobin in 0.1 M acetate buffer (pH 5.5) containing 1 mM EDTA.

In the first potential cycle a characteristic irreversible reduction at ca. -0.6 V vs. SCE is observed (see figure 6.8Ai), identical to process 2 observed in figure 6.5A. This is followed by the appearance of a new chemically reversible oxidation and reduction peak at ca. -0.08 and -0.32 V vs. SCE, respectively (see figure 6.8Aii), identical to process 1 from figure 6.5A. These processes are readily explained based on the known redox chemistry of the $Fe^{3+/2+}$ system under these conditions[30]. A poorly water soluble $FePO_4$ is formed initially immobilized on the TiO_2 surface. In the first

reduction process (first cycle, figure 6.8Ai) electrons flow through TiO_2 at sufficiently negative potential and $Fe_3(PO_4)_2$ is formed (see equation 6.1).

Process 2: $3\ Fe(PO_4)(s) + 3\ e^-(TiO_2) \rightleftharpoons Fe_3(PO_4)_2(s) + PO_4^{3-}(aq)$ (6.1)

Redistribution of this more water-soluble redox system occurs during subsequent oxidation and $FePO_4$ is deposited directly onto the ITO electrode surface within the porous host. The chemically reversible process 1 can be attributed to the $FePO_4/Fe_3(PO_4)_2$ redox system directly on ITO[31] (see equation 6.2).

Process 1: $3\ Fe(PO_4)(s) + 3\ e^-(ITO) \rightleftharpoons Fe_3(PO_4)_2(s) + PO_4^{3-}(aq)$ (6.2)

These results suggest a facile methemoglobin demetallation process in which methemoglobin in contact with the TiO_2 film is transformed into a metal-free protein. This process may also involve the free hemin metal complex as a reaction intermediate. It has been reported in the literature[31] that demetallation of hemin is possible at pH 5.5 and in the presence of phosphate and ferritin. Further evidence of this is confirmed below with the addition of the complexing agent EDTA.

By carrying out the voltammetric experiment in the presence of 1 mM EDTA in 0.1 M phosphate buffer (pH 5.5), the $Fe^{3+/2+}$ redox system is removed by complexation after the first reduction (for both cases immobilized Fe^{3+} or immobilized methemoglobin, not shown). Methemoglobin immobilized in the presence of 1 mM EDTA does not lead to a voltammetric response (see Figure 6.8B) and in the presence of oxygen no catalytic effect is observed. In contrast, the same experiment conducted in acetate buffer pH 5.5 instead of phosphate buffer (see Figure 6.8C) does lead to an enhanced current of the oxygen reduction indicating the presence of hemin (or hemoglobin). Similar results were reported also for thin film electrodes made from TiO_2 and nano-cellulose[32]. Based on these observation it seems likely that demetallation of methemoglobin occurs in the presence of phosphate (at pH 5.5) and in the presence of the porous host with negatively charged surface (phosphate binds to TiO_2[33]). In contrast, acetate binding to the TiO_2 surface is weaker and the charge of the surface is probably positive preventing the demetallation process.

6.4 Conclusions

It has been shown that TiO_2 films produced from 40nm particles are stable, electrically conducting and therefore suitable as a mesoporous host. Accumulation of hemoglobin into the film was observed, but rather than direct electrochemistry of the protein, voltammetric responses for Fe^{3+} (from protein demetallation) were observed. Redox protein reactivity can be complex and, in particular, when in contact with charged surfaces processes such as structural degradation and demetallation may occur. Under milder conditions, immobilization from an acetate buffer solution shows some catalytic behaviour characteristic of bound hemin or intact hemoglobin.

6.5 References

[1] J. Cooper, T. Cass, *Biosensors*, Oxford University Press, Oxford, 2004.

[2] C.H. Wang, C. Yang, Y.Y. Song, W. Gao, X.H. Xia, *Adv. Funct. Mater.*, 2005, **15**, 1267-1275.

[3] M.H. Ropers, R. Bilewicz, M.J. Stebe, A. Hamidi, A. Miclo, E. Rogalska, *Phys. Chem. Chem. Phys.*, 2001, **3**, 240-245.

[4] A.P. Fang, H.T. Ng, S.F.Y. Li, *Biosens. & Bioelectron.*, 2003, **19**, 43-49.

[5] H.Y. Lu, Z. Li, N.F. Hu, *Biophys. Chem.*, 2003, **104**, 623-632.

[6] S. Ben-Ali, D.A. Cook, P.N. Bartlett, A. Kuhn, *J. Electroanal. Chem.*, 2005, **579**, 181-187.

[7] (a) L. Shen, N.F. Hu, *Biomacromol.*, 2005, **6**, 1475-1483.

(b) P.L. He, M. Li, N.F. Hu, *Biopolym.*, 2005, **79**, 310-323.

[8] J. Yang, N.F. Hu, J.F. Rusling, *J. Electroanal. Chem.*, 1999, **463**, 53-62.

[9] J.F. Rusling (ed.), *Biomolecular Films*, Marcel Dekker, New York, 2003.

[10] C.G. Siontorou, D.P. Nikolelis, *Anal. Chim. Acta.*, 1997, **355**, 227-234.

[11] Y. Liu, H.Y. Liu, N.F. Hu, *Biophys. Chem.*, 2005, **117**, 27-37.

[12] P.L. He, N.F. Hu, *Electroanal.*, 2004, **16**, 1122-1131.

[13] E. Topoglidis, Y. Astuti, F. Duriaux, M. Grätzel, J.R. Durrant, *Langmuir*, 2003, **19**, 6894-6900.

[14] Q.W. Li, G.A. Luo, J. Feng, *Electroanal.*, 2001, **13**, 359-363.

[15] C.H. Fan, G.X. Li, J.Q. Zhu, D.X. Zhu, *Anal. Chim. Acta*, 2000, **423**, 95-100.

[16] S.M. Chen, C.C. Tseng, *J. Electroanal. Chem.*, 2005, **575**, 147-160.

[17] M.F. Perutz, A.J. Wilkinson, M. Paoli, and G.G. Dodson, *Annu. Rev. Biophys. Biomol. Struct.*, 1998, **27**, 1.

[18] M. Weissbluth, *Hemoglobin: Coopertivity and electronic properties*, Springer-Verlag, Berlin, 1974.

[19] C.A. Paddon, F. Marken, *Electrochem. Commun.*, 2004, **6**, 1249-1253.

[20] K.J. McKenzie, F. Marken, *Langmuir*, 2003, **19**, 4327-4331.

[21] K.J. McKenzie, F. Marken, M. Opallo, *Bioelectrochem.*, 2005, **66**, 41-47.

[22] F. Fabregat-Santiago, I. Mora-Sero, G. Garcia-Belmonte, J. Bisquert, *J. Phys. Chem. B*, 2003, **107**, 758-768.

[23] F. Marken, A.S. Bhambra, D.H. Kim, R.J. Mortimer, S.J. Stott, *Electrochem. Commun.*, 2004, **6**, 1153-1158.

[24] K.J. McKenzie, P.M. King, F. Marken, C.E. Gardner, J.V. Macpherson, *J. Electroanal. Chem.*, 2005, **579**, 267-275.

[25] M. Weissbluth, *Hemoglobin*, Springer, Berlin, 1974.

[26] R.E. Benesch, R. Edalji, R. Benesch, *Biochem.*, 1977, **16**, 2594.

[27] L. Shen, N.F. Hu, *Biochem. Biophys. Acta*, 1608 (2004) 22-23.

[28] H. Zhou, R.W. Yang, Y. Xu, K. Han, G.X. Li, *Anal. Lett.*, 2005, **38**, 2103-2115.

[29] X. Ma, X.J. Liu, H. Xiao, G.X. Li, *Biosens. & Bioelectron.*, **20**, 1836-1842.

[30] F. Marken, D. Patel, C.E. Madden, R.C. Millward, S. Fletcher, *New J. Chem.*, 2002, **26**, 259-263.

[31] R.R. Crichton, J.A. Soruco, F. Roland, M.A. Michaux, B. Gallois, G. Precigoux, J.P. Mahy, D. Mansuy, *Biochem.*, 1997, 36, 15049.

[32] M.J. Bonné, E.V. Milsom, M. Helton, W. Thielemans, S. Wilkins, F. Marken, *Elecrochem. Commun.*, 2007, **9**, 1985-1990.

[33] K.J. McKenzie, P.M. King, F. Marken, C.E. Gardner, J.V. Macpherson, *J. Electroanal. Chem.*, 2005, **579**, 267-275.

7. SnO_2-Poly(diallyl-dimethylammonium chloride) Films: Electrochemical Evidence for Heme-Protein Absorption, Denaturation, and Demetallation

7.1 Introduction

The use of mesoporous metal oxide films as hosts for biological redox systems has generated widespread interest in particular for sensor applications[1,2] and new types of host films are continuously developed[3]. These novel protein substrates combine the attractive properties of high surface area, optical transparency, non-toxicity, ease of fabrication, chemical and photochemical stability with the possibility of direct electron transfer between protein redox sites and the host electrode[4]. The direct electrochemistry of immobilized proteins and enzymes is often possible in these films and is useful for the design of biomimetic model systems[5] or as a basis for a range of sensing strategies[6] without the need for electron transfer mediators or promoters. However, proteins are very sensitive to environmental conditions and a change in environment could result in complex restructuring or denaturation. This may not be immediately obvious from the electrochemical behaviour and even demetallation may occur as highlighted in this report.

In the past the direct electrochemistry of heme proteins has been investigated in clay films[7], in SiO_2[8], TiO_2[9], ZnO[10], NiO[11], and in SnO_2 nanoparticle assemblies[12], in DNA[13], or in surfactant assemblies[14]. Sol-gel silicate films have been developed to host hemoglobin for electrocatalytic reactions[15,16]. Proteins have been shown to easily absorb into suitable nanoparticle assemblies directly from aqueous solutions, driven mainly by electrostatic interactions[17], and displaying high binding stability with apparently little denaturation. Recently, the advantages of using SnO_2 nanoparticle assemblies were highlighted[18] in particular the higher electrical conductivity of SnO_2 nanoparticle films when compared to that of TiO_2 or ZnO nanoparticle assemblies. Topoglidis et al. successfully immobilized non-heme proteins into SnO_2 assemblies[19,20] and heme proteins with nitric oxide sensing capabilities into modified SnO_2 assemblies[21]. SnO_2 has been employed as an electrochemically active host for proteins such as microperoxidase-11[22],

cytochromes[23], and hemoglobin[24]. The presence of additives such as poly-L-lysine has been shown to substantially promote the binding of proteins into SnO_2[25]. SnO_2 nanocomposites have also been successfully employed as electrodes for horse reddish peroxidase redox chemistry[26]. In this chapter nanocomposite films of SnO_2 nanoparticles assembled with the cationic poly(diallyl-dimethylammonium chloride) or PDDAC binder are investigated as an effective and electrochemically active host system for heme proteins. It is shown that, perhaps surprisingly, even under mild conditions in 0.1 M phosphate buffer denaturation and even heme demetallation are dominant processes.

7.2 Experimental

7.2.1 Reagents

Chemical reagents such as perchloric acid (70% A.C.S reagent), KCl, KOH, phosphoric acid (85% wt% solution in water, A.C.S reagent), hemin, $Fe(NO_3)_3$ hydrate were obtained commercially (Sigma-Aldrich) and used without further purification. Methemoglobin (Hb, bovine methemoglobin, H2625, from Sigma) was used without further purification. Unless stated otherwise, a 1 mg cm^{-3} Hb or cytochrome $P450_{cam}$ solution was prepared in aqueous 0.1 M phosphate buffer at pH 5.5 or 7. All solutions were prepared using de-ionised water with a resistivity of not less than 18 MΩ cm (Elga, High Wycombe, UK).

A sol of 35 wt% SnO_2 nanoparticles (nominal 15 nm diameter) was obtained either from Nyacol (US) or Alfa Aesar (UK). A dilute precursor sol was prepared by dilution of 1 cm^3 of SnO_2 sol into 10 cm^3 deionised water to give a 3.5 wt% sol). The cationomer poly(diallyl-dimethylammonium chloride) (PDDAC, Aldrich, average molecular weight < 100 kD, 35 wt% in water), an organic binder with quarternary ammonium groups, was diluted into de-ionised water to give a 0.35 wt% solution.

7.2.2 Cytochrome $P450_{cam}$ (CYP101) Expression and Activity Testing

A literature method was followed for the expression and isolation of cytochrome $P450_{cam}$[27]. *Escherichia Coli* JM109 cells were transfected with the pAW7292

plasmid. The *E. coli* was grown in LB broth at 30°C for 9 hours. At 6 hours the media was inoculated with camphor and the temperature increased to 37°C to promote protein production. The cells were then harvested by centrifugation for 5 minutes at 5000 rpm at 4°C. Each cell pellet was then re-suspended and combined in 20 cm^3 of buffer containing 40 mM potassium phosphate and 1 mM camphor, at pH 7.4. The cells were repeatedly lysed by sonication for 1 minute and at ca. 2°C and centrifuged at 4°C. The resulting cell free supernatant containing the CYP101 protein was removed and combined. The protein was then separated on an ÄKTA™ system from Amersham Pharmacia Biotech Ltd. Supernatant was run on an SDS-PAGE gel, with a single band a 46.9 KDa, characteristic of CYP101 protein being used to identify both that the protein had been expressed and had been purified. An NADH consumption assay was performed to determine the activity of the expressed CYP101 in solution (0.1 μmol dm^{-3} CYP101, 250 μmol dm^{-3} NADH, 10 μmol dm^{-3} putidaredoxin and 1 μmol dm^{-3} putidaredoxin reductase in 50 μmol dm^{-3} Tris pH 7.4 with 2 μmol dm^{-3} camphor). The absorption peak at 340 nm, characteristic of NADH was followed with time on a Helios γ spectrophotometer and the protein activity number thus calculated. An activity number of 5620 min^{-1} (5620 moles of NADH consumed / mol of CYP101 / minute) was obtained.

Cytochrome $P450_{cam}$ expression and activity testing was performed by Hayley Dash.

7.2.3 Instrumentation

Electrochemical experiments were conducted with a PGSTAT 30 Autolab system (Eco Chemie, Netherlands) in a conical three-electrode cell. The counter electrode was platinum gauze and the reference electrode was a KCl saturated calomel electrode (SCE, Radiometer). The working electrodes were prepared from tin-doped indium oxide (ITO) coated glass (10 mm × 60 mm, resistivity 15 Ω per square, Image Optics Components Ltd.). ITO electrodes were cleaned prior to film deposition by rinsing in ethanol followed by deionised water and furnace treated (Elite tube furnace) at 500°C in air for 60 minutes. UV/Vis spectra of solution and solid samples were obtained with a Helios γ spectrometer (Thermo Electron Corp.). The temperature during all measurements was maintained at 22 ± 2 °C. An atomic

force microscope (Digital Instruments Nanoscope III, used in contact mode) and a scanning electron microscope (JEOL JSM6310) were used to obtain images of SnO_2 nanoparticle films. Prior to SEM imaging samples were gold sputter coated to enhanced the image quality.

7.2.4 Procedures and Electrode Design

A simple layer-by-layer dip coating technique following the Decher method[28,29] was used to form SnO_2-polymer mesoporous nanocomposite films on ITO coated glass electrodes. First, the clean ITO electrodes were dipped into poly(diallyl-dimethylammonium chloride) (PDDAC, cationic binder, 0.35 wt% in water) solution to reverse the charge on the electrode and enable tin dioxide binding. They were then rinsed with deionised water, dried (at ca. 50 °C) before being dipped into a SnO_2 sol (3.5wt% in water, ca. 15 nm diameter), once again washed, and then dried. SnO_2 sols were observed to gradually lose the ability to bind to the cationic surface (presumably due to CO_2 uptake) and therefore fresh solutions were always required. Each dipping step was timed to allow 60 seconds immersion. Further layers of SnO_2 polymer were built up by continuing these dipping steps. Once the desired number of layers was achieved some of the electrodes were heat treated to remove the organic content (500°C, 30 minutes, Elite tube furnace).

Methemoglobin and cytochrome $P450_{cam}$ absorption was achieved by equilibrating the SnO_2-poly(diallyl-dimethylammonium chloride) film electrode in a solution of methemoglobin (1 mg cm^{-3}) or cytochrome $P450_{cam}$ (1 mg cm^{-3}) in aqueous 0.1 M phosphate buffer (pH 5.5) for a minimum of 1 hour, followed by rinsing in de-ionised water. Electrodes were stored in phosphate buffer solution pH 5.5 at 4°C in the dark.

7.3 Results and Discussion

7.3.1 Deposition and Characterization of Nanoparticulate SnO_2–poly(diallyl-dimethylammonium chloride) Film Electrodes

Initial test experiments confirmed that continued alternate deposition of SnO_2 nanoparticles and poly(diallyl-dimethylammonium chloride) binder allows visible films to be deposited onto glass and tin-doped indium oxide (ITO) coated glass slides. Experimentally, a clean ITO electrode is dipped first into poly(diallyl-dimethylammonium chloride) (0.35 wt% in water), then rinsed with water and dried, dipped into SnO_2 sol (3.5 wt% in water), and again rinsed with water followed by drying (see experimental section 7.2.4). Repeating this sequence leads to the gradual growth of a mesoporous SnO_2-poly(diallyl-dimethylammonium chloride) film at the electrode surface. In order to characterize the topology and thickness of the films atomic force microscopy (AFM) and scanning electron microscopy (SEM) imaging were employed.

Films deposited in various thicknesses and before/after heat treatment were characterized by AFM. The electrode surface was scratched with a scalpel prior to imaging in order to expose the bare electrode surface and to allow film thickness information to be obtained. Figures 7.1A and 7.1B show typical images and cross section data obtained for 5-layer films before and after a 30 minute heat treatment at 500 °C.

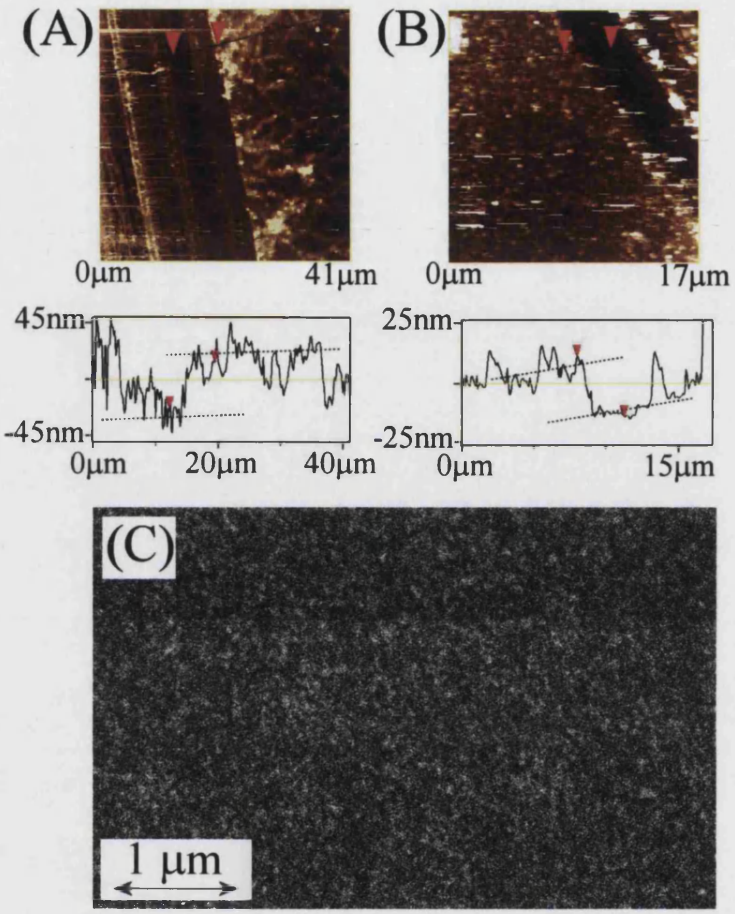

Figure 7.1 AFM topography images and section analysis for a scratched 5-layer SnO_2-poly(diallyl-dimethylammonium chloride) film (A) before and (B) after heat treatment at 500 °C for 30 minutes. The cross section analysis for the two types of films shows a thickness of approximately 50 nm and 25 nm, respectively. (C) SEM image of a 5-layer film of SnO_2-poly(diallyl-dimethylammonium chloride).

The AFM images confirm the formation of a smooth and uniform film. It can be seen that a five layer deposit of the SnO_2-poly(diallyl-dimethylammonium chloride) film has a thickness of approximately 50 nm (see Figure 7.1A cross section). Doubling the number of deposition cycles leads to doubling of the thickness. The increase in thickness is therefore approximately linear with 10 nm per layer. The heat treated 5-layer film (with all organic components removed) shows much clearer outline of the

particulate components and a reduced purely inorganic SnO_2 film thickness of approximately 25 nm (Figure 7.1B). The removal of the polymer binder by heat and some particle sintering (which becomes more significant during prolonged treatment at 500 °C) results in a loss of approximately 50% of the film volume.

For a film with a 5-layer nanocomposite deposit, SEM images (see Figure 7.1C) clearly show a highly uniform coating with SnO_2 nanoparticles bound by poly(diallyl-dimethylammonium chloride). Individual particles of nominal 15 nm diameter are not fully resolved but the uniform mesoporous structure is revealed.

7.3.2 Voltammetric Characterisation of Nanocomposite SnO_2–poly(diallyl-dimethylammonium chloride) Film Electrodes

Figure 7.2 shows typical cyclic voltammetry responses for ITO electrodes coated with a film of SnO_2-poly(diallyl-dimethylammonium chloride) (or SnO_2-PDDAC) immersed in aqueous 0.1 M phosphate buffer solution. Figure 7.2A shows the reduction and re-oxidation of a 10-layer SnO_2-PDDAC film in comparison to the background response obtained with a clean ITO electrode. It can be seen that a nearly symmetric (reversible) charging-discharging current commences at ca. -0.4 V vs. SCE (see Zone 2). At potentials negative of ca. -0.8 V vs. SCE the process becomes chemically irreversible presumably due to the onset of hydrogen evolution. Figure 7.2B demonstrates that the voltammetric currents associated with the reduction and re-oxidation of the SnO_2 deposit scale with the amount of deposit (or the thickness of the film). Increasing the scan rate causes an increase in the current response (see Figure 7.2C) and reveals a further weaker charging current commencing at ca. -0.1 V vs. SCE (see Zone 1). The current in this region is likely to correspond to more highly solvated SnO_2 sites at the surface of the nanoparticles. These current responses are consistent with n-type semiconducting behaviour (similar to TiO_2[30]). However, electrically conducting characteristics due to surface states can be expected probably even within the positive potential range. This is consistent with literature reports on the properties of SnO_2 films[31] and protein modified SnO_2 films[32].

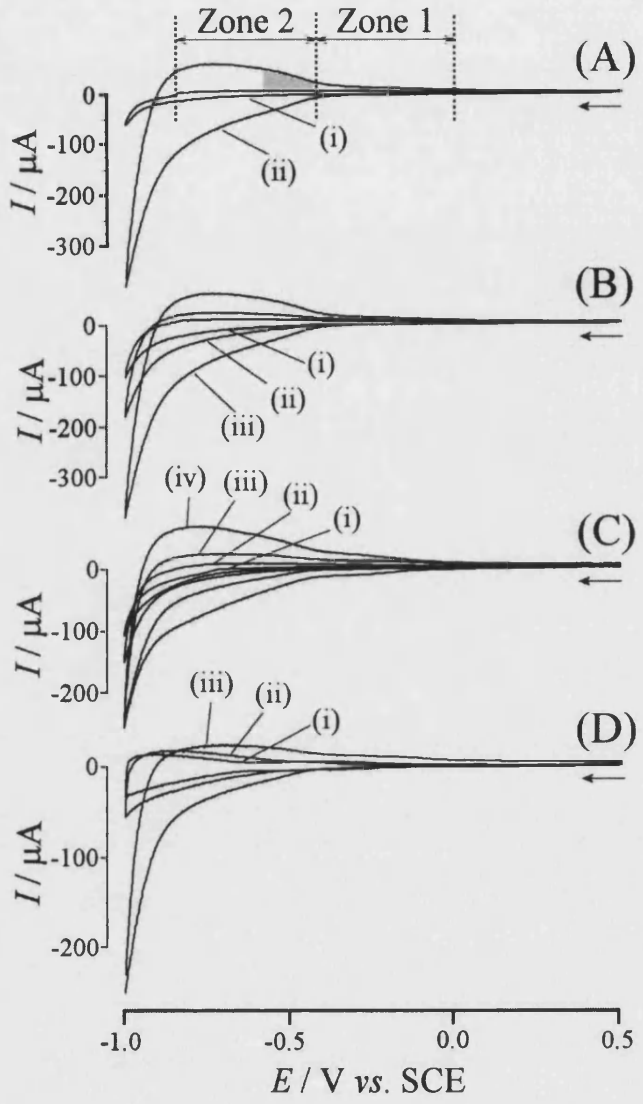

Figure 7.2 (A) Voltammograms (scan rate 0.1 Vs^{-1}) obtained for a 1cm^2 ITO electrode coated with a (i) 0-layer and (ii) 10-layer SnO_2-PDDAC film and immersed in 0.1 M phosphate buffer pH 5.5. (B) Cyclic voltammograms (scan rate 0.1 Vs^{-1}) obtained for a 1 cm^2 ITO electrode coated with (i) 1, (ii) 3, and (iii) 10 layers of SnO_2-PDDAC nanocomposite and immersed in aqueous 0.1M phosphate buffer at pH 5.5. (C) Cyclic voltammograms (scan rates (i) 0.02, (ii) 0.05, (iii) 0.1, and (iv) 0.2 Vs^{-1}) obtained for a 5-layer SnO_2-PDDAC film immersed in 0.1 M phosphate buffer at pH5.5. (D) Cyclic voltammograms (scan rate 0.1Vs^{-1}) obtained for a 5-layer SnO_2-PDDAC film electrode immersed in 0.1M phosphate buffer solution at (i) pH 8.5, (ii) pH7.0, and (iii) pH 5.5.

In Figure 7.2D the effect of the pH on the voltammetric response is demonstrated. The reduction signal is shifted to more negative potentials in more alkaline solution

as expected for a process involving the uptake of protons during reduction or charging of SnO_2. Overall, these reduction responses are consistent with a process involving a reversible charging of the SnO_2 film in a process tentatively assigned to the mechanism described as in equation 7.1.

$$[SnO_2]_n + e^- + H^+(aq) \rightleftharpoons \{[SnO_2]_n{}^-H^+\} \quad (7.1)$$

It is interesting to explore the number of electrons injected into the SnO_2-poly(diallyl-dimethylammonium chloride) film per SnO_2 nanoparticle at a given potential. From the AFM thickness data the number of particles in a 10-layer deposit of SnO_2-PDDAC can be estimated as 4×10^{12} particles (per cm^2). By comparison with the charge under the voltammetric signals the number of electrons transferred per SnO_2 nanoparticle can be obtained. The area shaded gray in Figure 7.2A corresponds to a charge consistent with approximately 50 electrons per SnO_2 nanoparticle which is reasonable considering the considerably higher number of surface Sn atoms per particle (ca. 10^4). Next, the effects of additional protein based redox centers immobilised into the SnO_2-PDDAC film are investigated.

7.3.3 Attempted Immobilization and Reactivity of Methemoglobin in SnO_2–poly(diallyl-dimethylammonium chloride) Nanocomposite Film Electrodes

The diameter of the SnO_2 nanoparticles, nominal ca. 15 nm, is suitable for the formation of pores and the immobilization of a high molecular weight protein such as hemoglobin or methemoglobin (the Fe(III) form of hemoglobin) with a molecular weight of ca. 68 kD and an approximate diameter of 55 Å[33,34]. Hemoglobin consists of four subunits each of ca. 17 kD and dissociation into dimers or monomer subunits has been observed for example in the presence of high applied pressures or with suitable allosteric effectors[35]. It has been proposed recently that mesoporous films made from small 6 nm diameter TiO_2 nanoparticles inhibit the absorption of large hemoglobin proteins[36].

Figure 7.3A shows typical cyclic voltammograms obtained for SnO_2-PDDAC film modified electrodes after immobilization of methemoglobin (the electrode was immersed for 24h in 15 μM methemoglobin in aqueous 0.1 M phosphate buffer pH

5.5) immersed in aqueous 0.1 M phosphate buffer pH 5.5. A well defined reduction – reoxidation response is observed at a potential of -0.25 V vs. SCE and the symmetry of the signal suggests facile electron transfer and transport within the mesoporous host film. The apparently effective adsorption of the protein into the mesoporous film appears remarkable due to the (in average) positive total charge on both mesoporous structure and protein at pH 5.5. The immobilization of methemoglobin into calcined SnO_2 also appears to occur (data not shown) giving a very similar voltammetric response.

Changing the thickness of the SnO_2-PDDAC film at the electrode surface allows the effectiveness of the process to be confirmed. Figure 7.3B shows the linear increase of the charge under the apparent methemoglobin re-oxidation peak as a function of layers deposited (or film thickness). The charge under the voltammetric response is surprisingly high (it suggests the uptake of ca. 60 methemoglobin molecules per SnO_2 nanoparticle within the film) and this is the first indication of a problem during the methemoglobin immobilisation.

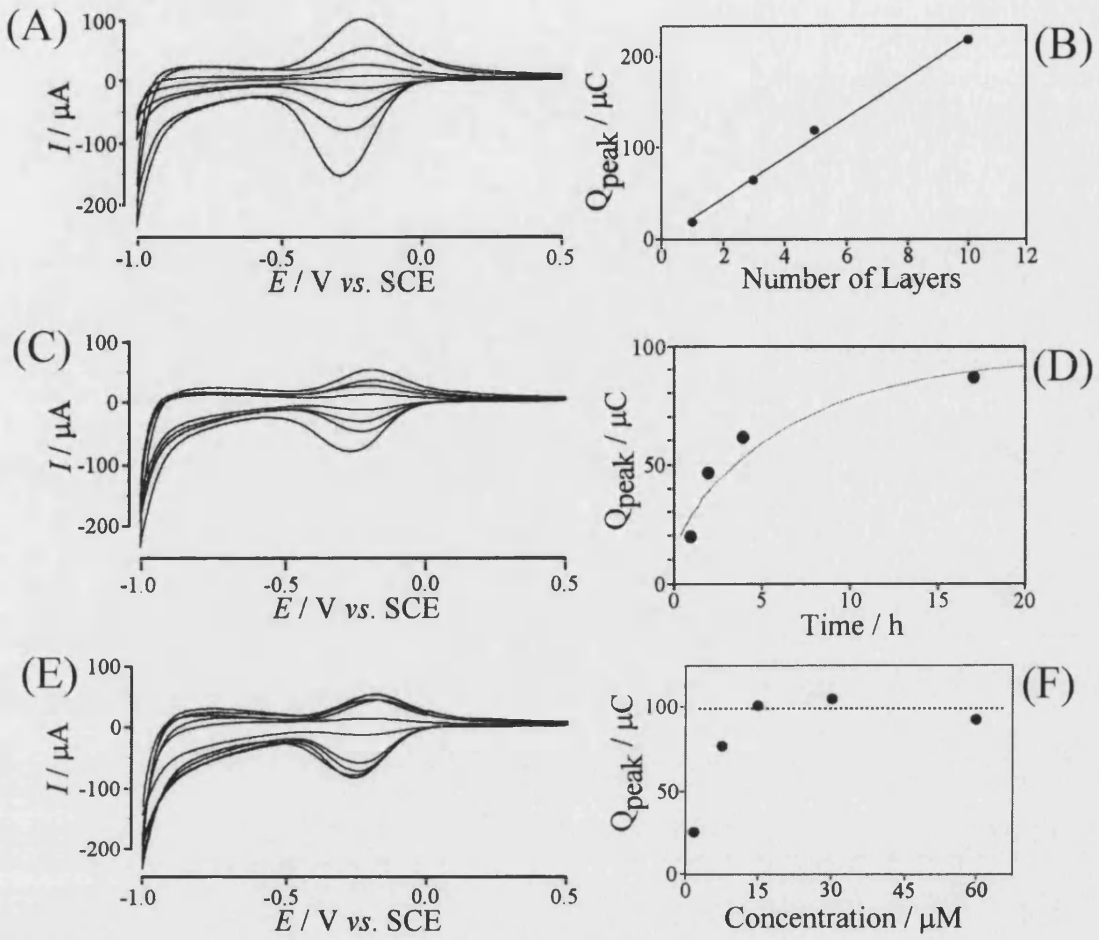

Figure 7.3 (A) Cyclic voltammograms (scan rate 0.1 Vs^{-1}) obtained for the reduction and re-oxidation of absorbed methemoglobin on an ITO electrode coated with 1, 3, 5, and 10 layers of SnO_2-PDDAC nanocomposite and immersed in aqueous 0.1 M phosphate buffer at pH5.5. (B) Plot of the charge under the reduction peak, Q_{peak}, versus the number of SnO_2-PDDAC layers deposited at the electrode surface. (C) Cyclic voltammograms (scan rate 0.1Vs^{-1}) obtained for the reduction of absorbed methemoglobin in a 5-layer SnO_2-PDDAC nanocomposite film immersed in aqueous 0.1 M phosphate buffer pH 5.5. The methemoglobin absorption was carried out in a 15 μM solution in 0.1 M phosphate buffer pH5.5 for 1, 2, 4, and 17 hours. (D) Plot of the charge under the peak versus absorption time (the line corresponds to a diffusion process with $D_{methemoglobin} = 4 \times 10^{-20}$ m^2s^{-1}, see text). (E) Cyclic voltammograms (scan rate 0.1Vs^{-1}) obtained for the reduction and re-oxidation of absorbed methemoglobin in a 5-layer SnO_2-PDDAC nanocomposite film immersed in aqueous 0.1 M phosphate buffer pH 5.5. Methemoglobin absorption was carried out in 1.5 μM, 7.5 μM, 15 μM, 30 μM, 60 μM methemoglobin solution (0.1 M phosphate buffer pH5.5 for 17 hours). (F) Plot of the charge under the oxidation peak versus the methemoglobin concentration during absorption.

UV/Vis-spectroelectrochemical experiments were conducted in order to assess the effect of the SnO_2-PDDAC environment on the protein and weak absorption changes at ca. 415 nm (not shown) appeared to confirm the presence of electrochemically active methemoglobin. Next, the time and concentration dependence of the methemoglobin absorption process are investigated. An experiment was conducted in which the uptake of methemoglobin into a 5-layer SnO_2-PDDAC film was monitored with time. Figure 7.3C shows a typical set of voltammetric responses obtained as a function of absorption time and in Figure 7.3D the increase in the charge under the voltammetric peak is plotted versus time. The limit of approximately 100 μC is reached only after ca. 24h consistent with slow uptake of protein into the film. If protein diffusion is assumed to be the rate determining step this corresponds to an estimated diffusion coefficient of $D_{methemoglobin} = 4 \times 10^{-20}$ m^2s^{-1}. In order to explore the effect of the methemoglobin concentration during absorption on the immobilization process, the protein concentration was gradually varied from 1.5 μM to 60 μM. The data and plot shown in Figure 7.3E and 7.3F show the characteristic behaviour roughly consistent with a Langmuir-type isotherm with the approximate binding constant $K = 2 \times 10^5$ M^{-1}.

Voltammetric data presented up to this point seem to support the reversible electron transfer to hemoglobin immobilized within the mesoporous SnO_2-PDDAC host. However, similar experiments conducted with only Fe^{3+} in low concentration in the deposition solution (in the absence of any protein) result in essentially identical voltammetric responses. In order to distinguish between Fe^{3+} bound to the SnO_2 surface and hemoglobin immobilized within the mesoporous host, experiments were conducted in the presence of ethylenediaminetetraacetic acid (EDTA). Figure 7.4 shows typical cyclic voltammograms obtained in the presence of 1 mM EDTA. The peak response rapidly decreases for both the methemoglobin (Figure 7.4A) and Fe^{3+} (Figure 7.4B). The remaining reversible voltammetric response is likely to be associated with Fe^{3+} bound strongly and irreversibly to the SnO_2 surface. In order to explain the above data a sequence of protein immobilization, demetallation, and iron removal seems likely. The demetallated methemoglobin protein may remain bound to the SnO_2-PDDAC film. Immobilisation of methemoglobin in the presence of EDTA results in featureless voltammograms consistent with those shown in Figure 7.2.

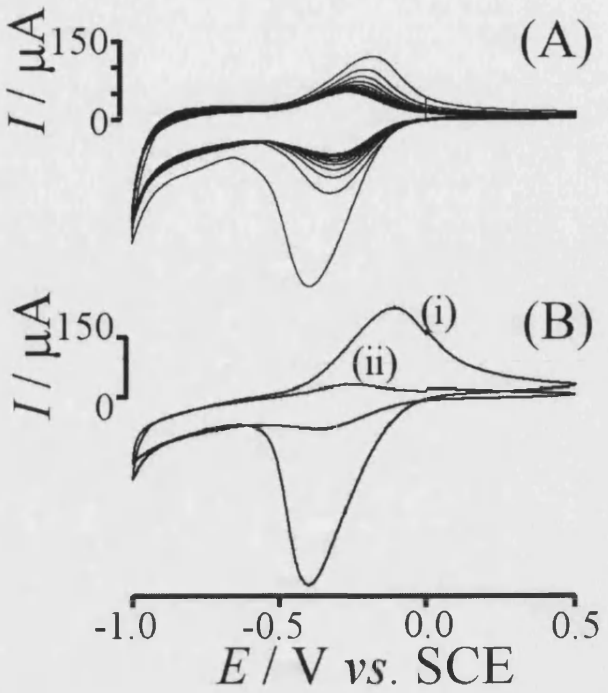

Figure 7.4 (A) Cyclic voltammograms (scan rate 0.1 Vs^{-1}) obtained for the reduction of absorbed methemoglobin (absorption from 15 μM methemoglobin in 0.1 M phosphate buffer pH5.5 for 24 h) in a 5-layer SnO_2-PDDAC nanocomposite film immersed in aqueous 0.1 M phosphate buffer pH 5.5 in the presence of 1 mM EDTA. (B) Cyclic voltammograms (scan rate 0.1 Vs^{-1}, (i) 1st cycle and (ii) 10th cycle) obtained for the reduction of absorbed Fe^{3+} (absorption from ca. 60 μM Fe^{3+} in 0.1 M phosphate buffer pH5.5 for 24 h) in a 5-layer SnO_2-PDDAC nanocomposite film immersed in aqueous 0.1 M phosphate buffer pH 5.5 in the presence of 1 mM EDTA.

It can be concluded that what appeared to be a reduction – reoxidation process for methemoglobin is actually likely to be a $Fe^{3+/2+}$ redox system (in the presence of phosphate [37]) probably formed after adsorption of the protein into the mesoporous film and by immobilization of Fe^{3+} at the SnO_2 surface (see equation 7.2).

$$Fe(III)PO_4(SnO_2\ surface) + e^- \rightleftharpoons 1/3\ Fe_3(II)(PO_4)_2(SnO_2\ surface) + 1/3\ PO_4^{3-} \quad (7.2)$$

The fact that demetallation of methemoglobin occurs in particular at pH 5.5 and in the presence of phosphate is consistent with observations in TiO_2-cellulose films[38] and has been highlighted previously for a related process in ferritin[39]. However, further experimental work will be required to further resolve the fate of

methemoglobin in SnO_2-PDDAC films and the effect of the reaction conditions (pH, ionic strength, electrolyte composition, etc.). The problem of distinguishing intact immobilized redox proteins and partially or fully denatured redox proteins has been emphasized recently[40]. The use of EDTA to sequester "free" $Fe^{3+/2+}$ could provide a chemical test for demetallation processes.

7.3.4 Attempted Immobilization and Reactivity of Cytochrome *P*450$_{cam}$ (CYP101) in SnO_2–poly(diallyl-dimethylammonium chloride) Film Electrodes

Cytochrome *P*450s represent an enormously extended and versatile group of redox proteins with very important biological functions in hydroxylation and drug metabolism[41]. It has been proposed that immobilization of cytochrome *P*450 systems in redox active films at electrodes could lead to new insights into their reactivity and function with applications in novel specific sensor devices[42]. In this study cytochrome *P*450$_{cam}$ was absorbed into SnO_2-PDDAC nanocomposite electrodes from a 0.1 M phosphate buffer pH 5.5 solution containing 17 μM cytochrome *P*450$_{cam}$. The structure of *P*450$_{cam}$ is known[43,44,45] and the protein has a molecular weight of about 50 kD with an approximate diameter of 4-5 nm. In buffer solution at a pH of 5.5 the protein is expected to behave similarly to the methemoglobin system. However, there is only one heme group per cytochrome *P*450$_{cam}$ protein.

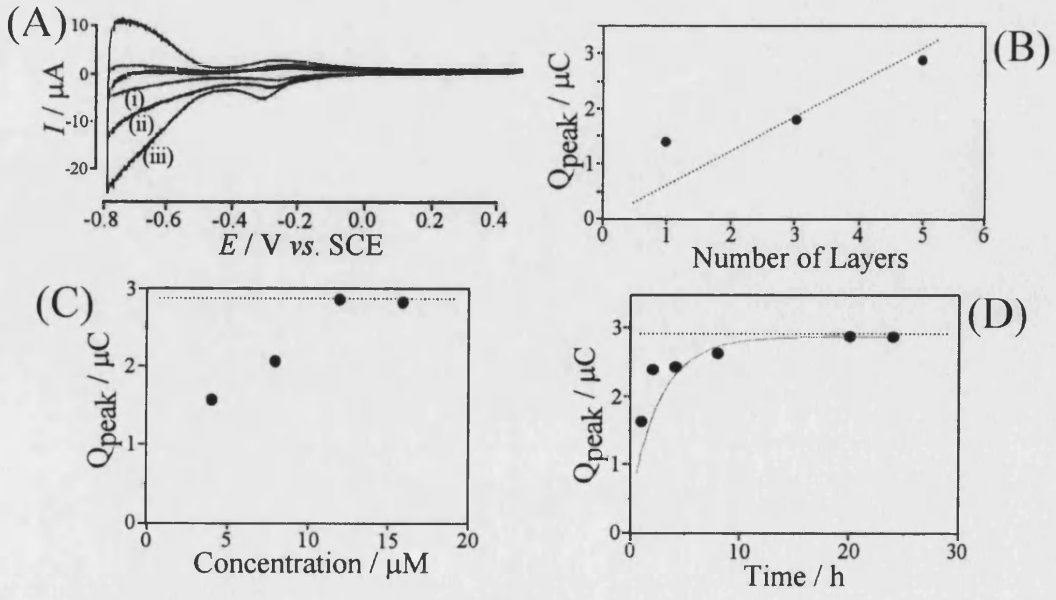

Figure 7.5 (A) Cyclic voltammograms (scan rate 0.1 Vs^{-1}) obtained for the reduction and re-

oxidation of immobilised cytochrome $P450_{cam}$ on an ITO electrode coated with (i) 1, (ii) 3, and (iii) 5 layers of SnO_2-PDDAC nanocomposite film (the protein was immobilised by 20 h accumulation from a 17 μM cytochrome $P450_{cam}$ solution in 0.1 M phosphate buffer pH 5.5) immersed in aqueous 0.1 M phosphate buffer pH7. (B) Plot showing the effect of the number of SnO_2-PDDAC layers on the charge under the reversible voltammetric signal. (C) Plot of the charge under the voltammetric signal versus the concentration of cytochrome *P*450 during accumulation into a 5-layer SnO_2-PDDAC film. (D) Plot of the charge under the voltammetric peak versus the accumulation time.

Figure 7.5 shows typical voltammetric responses observed for the reduction and re-oxidation of cytochrome $P450_{cam}$ accumulated within the SnO_2-PDDAC nanocomposite film, with a midpoint potential of -0.28 V vs. SCE. The voltammetric signal is approximately 40 times smaller when compared to the corresponding methemoglobin signal (see Figure 7.3) but otherwise very similar. From the voltammetric responses it can be seen that the increase in film thickness is correlated to the corresponding increase in charge for the protein reduction and re-oxidation (see Figure 7.5B). Figure 7.5C shows a plot of the charge under the voltammetric signal for immobilized cytochrome $P450_{cam}$ as a function of the protein solution concentration during accumulation. The estimated Langmuirian binding constant (estimated from the point of half coverage) is approximately $K = 2 \times 10^5\ M^{-1}$. Next, the effect of the accumulation time is considered. Figure 7.5D demonstrates that for a 5-layer SnO_2-PDDAC film the protein accumulation goes to completion after approximately 20 hours. Due to the similarity in the voltammetric signal it is again likely that Fe^{3+} released from the protein is detected rather than the intact protein.

In order to explore and contrast the reactivity of methemoglobin, cytochrome $P450_{cam}$, Fe^{3+} and hemin immobilised in SnO_2-PDDAC nanocomposite films, voltammetric experiments in the presence and in the absence of oxygen were conducted. Hemin, the prosthetic group in heme proteins, is known to effectively catalyse the reduction of oxygen[46,47].

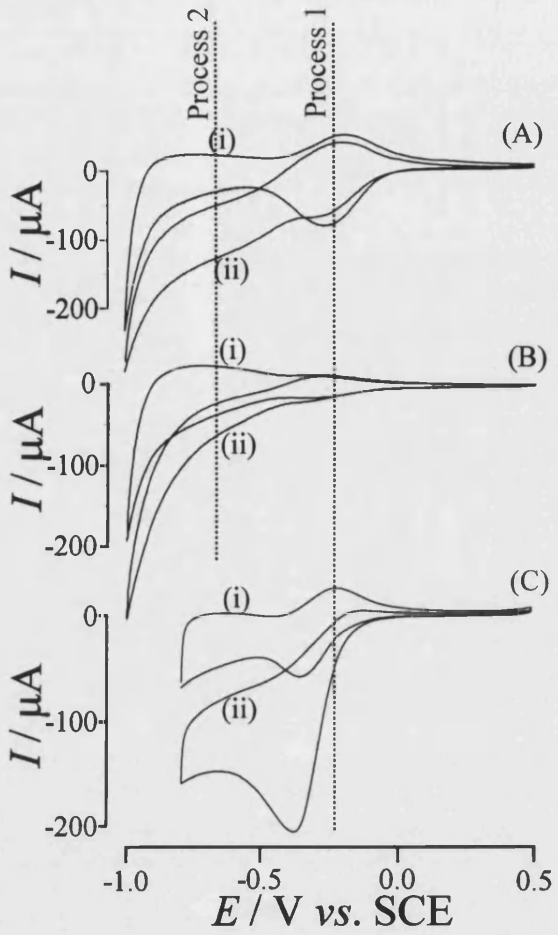

Figure 7.6 (A) Cyclic voltammograms (scan rate 0.1 Vs^{-1}) obtained for the reduction of absorbed hemoglobin (absorbed from 15 μM Hb solution, 17 hours) in a 5-layer SnO_2-PDDAC nanocomposite film with (ii) and without (i) oxygen present in 0.1M pH5.5 phosphate buffer solution. (B) Cyclic voltammograms (scan rate 0.1 Vs^{-1}) obtained for the reduction of absorbed cytochrome $P450_{cam}$ (absorbed from 12μM $P450_{cam}$ solution, 17 hours) in a 5-layer SnO_2-PDDAC nanocomposite film with (ii) and without (i) oxygen present in 0.1M pH5.5 phosphate buffer solution. (C) Cyclic voltammograms (scan rate 0.1 Vs^{-1}) obtained for the reduction of absorbed hemin (absorbed from 60μM hemin in 0.1 M carbonate buffer pH 9, 17 hours) in a 5-layer SnO_2-PDDAC nanocomposite film with (ii) and without (i) oxygen present in 0.1 M pH5.5 phosphate buffer solution.

Figure 7.6 shows cyclic voltammograms for the reduction of (A) methemoglobin and (B) cytochrome $P450_{cam}$ compared (ii) in the presence and (i) in the absence of oxygen (ca. 0.2 mM oxygen in phosphate buffer pH 5.5). In both cases it can clearly be seen that the original reduction and re-oxidation responses for the immobilized Fe^{3+} (after protein demetallation) are not affected (see Process 1). The reduction of oxygen occurs in both cases as a separate irreversible redox system at a potential of

ca. -0.5 V vs. SCE (Process 2). In the absence of protein and using a Fe^{3+}-modified 5-layer SnO_2-PDDAC film electrode the same voltammetric features are observed (not shown). Finally, with hemin directly immobilized into the SnO_2-PDDAC film the catalytic reduction of oxygen is clearly observed (see Figure 7.6C).

In conclusion, demetallation of both methemoglobin and cytochrome $P450_{cam}$ appears to dominate the electrochemical responses after the attempted immobilization into SnO_2-PDDAC films and meaningful information about the redox properties of the proteins has not been obtained. A major factor in the demetallation process appears to be the presence of charged surfaces e.g. the SnO_2-PDDAC host. However, more details about the effects of the reaction conditions on the denaturation processes will be required.

7.4 Conclusions

In this study it has been shown that SnO_2-PDDAC films produced in a layer-by-layer deposition procedure are electrochemically active and electrically conducting and therefore suitable as mesoporous hosts. Accumulation of heme proteins into the films has been observed, however, rather than direct electrochemistry of the protein, voltammetric responses for immobilized Fe^{3+} (from protein demetallation) have been observed. The reactivity towards oxygen and EDTA allows protein, hemin, and Fe^{3+} based redox processes to be distinguished. The question of why facile demetallation occurs for heme proteins but not for hemin remains open.

7.5 References

[1] L. Gorton, *Biosensors and Modern Biospecific Analytical Techniques*, Elsevier, Amsterdam, 2005.

[2] J. Cooper, T. Cass, *Biosensors, Oxford University Press*, Oxford, 2004.

[3] F. Davis, S.P.J. Higson, *Biosens. Bioelectron.*, 2005, **21**, 1.

[4] J.F. Rusling, R.J. Forster, *J. Coll. Interface Sci.*, 2003, **262**, 1.

[5] J. Hirst, *Biochim. Biophys. Acta Bioenerg.*, 2006, **1757**, 225.

[6] J.F. Rusling, Acc. Chem. Res. 31 (1998) 363.

[7] Y.L. Zhou, Z. Li, N.F. Hu, Y.H. Zeng, J.F. Rusling, *Langmuir,* 2002, **18,** 8573.

[8] P.L. He, N.F. Hu, *Electroanalysis,* **2004,** 16, 1122.

[9] W.W. Yang, Y. Bai, Y.C. Li, C.Q. Sun, *Anal. Bioanal. Chem.*, 2005, **382**, 44.

[10] X.L. Zhu, I. Yuri, X. Gan, I. Suzuki, G.X. Li, *Biosens. Bioelectron.*, 2007, **22**,1600.

[11] A. Salimi, E. Sharifi, A. Noorbakhsh, S. Soltanian, *Electrochem. Commun.*, 2006, **8**, 1499.

[12] E. Topoglidis, Y. Astuti, F. Duriaux, M. Grätzel, J.R. Durrant, *Langmuir*, 2003, **19**, 6894.

[13] A.K.M. Kafi, F. Yin, H.K. Shin, Y.S. Kwon, *Thin Solid Films*, 2006, **499**, 420.

[14] X.L. Chen, N.F. Hu, Y.H. Zeng, J.F. Rusling, J. Yang, *Langmuir,* 1999, **15** 7022.

[15] Q.L. Wang, G.X. Lu, B.J. Yang, *Biosens. & Bioelectron.*, 2004, **19**, 1269.

[16] G.Y. Shi, Z.Y. Sun, M.C. Liu, L. Zhang, Y. Liu, Y.H. Qu, L.T. Jin, *Anal. Chem.*, 2007, **79,** 3581.

[17] K.J. McKenzie, F. Marken, *Langmuir,* 2003, 19, 4327.

[18] E. Topoglidis, Y. Astuti, F. Duriaux, M. Grätzel, J.R. Durrant, *Langmuir,* 2003, **19**, 6894.

[19] E. Topoglidis, E. Palomares, Y. Astuti, A. Green, C.J. Campbell, J.R. Durrant, *Electroanalysis,* 2005, 17, 1035.

[20] Y. Astuti, E. Topoglidis, P.B. Briscoe, A. Fantuzzi, G. Gilardi, J.R. Durrant, *J. Am. Chem. Soc.*, 2004, **126**, 8001.

[21] E. Topoglidis, B.M. Discher, C.C. Moser, P.L. Dutton, J.R. Durrant, *ChemBioChem* , 2003, **4**, 1332.

[22] Y. Astuti, E. Topoglidis, G. Gilardi, J.R. Durrant, *Bioelectrochem.*, 2004, **63**, 55.

[23] E. Topoglidis, B.M. Discher, C.C. Moser, P.L. Dutton, J.R. Durrant, *ChemBioChem,* 2003, 4, 1332.

[24] E. Topoglidis, Y. Astuti, F. Duriaux, M. Grätzel, J.R. Durrant, *Langmuir,* 2003, **19,** 6894.

[25] E. Topoglidis, E. Palomares, Y. Astuti, A. Green, C.J. Campbell, J.R. Durrant, *Electroanalysis*, 2005, **17,**1035.

[26] N.Q. Jia, Q. Zhou, L. Liu, M.M. Yan, Z.Y. Jiang, *J. Electroanal. Chem.*, 2005, **580**, 213.

[27] A.C.G. Westlake, C.F. Harford-Cross, J. Donovan, L.-L. Wong, *Eur. J. Biochem.*, 1999, **265**, 929.

[28] G. Decher, J.B. Schlenoff, *Multilayer thin films*, Wiley-VCH, New York, 2003.

[29] K.J. McKenzie, F. Marken, M. Hyde, R.G. Compton, *New J. Chem.*, 2002, **26**, 625.

[30] F. Marken, A.S. Bhambra, D.H. Kim, R.J. Mortimer, S.J. Stott, *Electrochem. Commun.*, 2004, **6**, 1153.

[31] A.N.M. Green, E. Palomares, S.A. Haque, J.M. Kroon, J.R. Durrant, *J. Phys. Chem. B*, 2005, **109**, 12525.

[32] E. Topoglidis, Y. Astuti, F. Duriaux, M. Grätzel, J.R. Durrant, *Langmuir*, 2003, **19**, 6894.

[33] M. Weissbluth, *Hemoglobin*, Springer-Verlag, Berlin, 1974.

[34] L. Stryer, *Biochemistry*, W.H. Freeman and Company, New York, 1995, pp. 150-151.

[35] G. Schay, L. Smeller, A. Tsuneshige, T. Yonetani, J. Fidy, *J. Biol. Chem.*,

2006, **281**, 25972.

[36] C.A. Paddon, F. Marken, *Electrochem. Commun.*, 2004, **6,** 1249.

[37] F. Marken, D. Patel, C.E. Madden, R.C. Millward, S. Fletcher, *New J. Chem.*, 2002, **26,** 259.

[38] M.J. Bonné, E.V. Milsom, M. Helton, W.Thielemans, S. Wilkins, F. Marken, *Electrochem. Commun.*, 2007, 9 (2007) in print.

[39] N. Carette, W. Hagen, L. Bertrand, N. de Val, D. Vertommen, F. Roland, L. Hue, R.R. Crichton, *J. Inorg. Biochem.*, 2006, **100**, 1426.

[40] Z. Brusova, L. Gorton, E. Magner, *Langmuir*, **22**, 11453.

[41] P.R. Ortiz de Montellano, *Cytochrome P450, Structure, Mechanism, and Biochemistry*, 3rd ed., Kluwer, New York, 2005.

[42] J.F. Rusling, E.G. Hvastkovs, J.B. Schenkman, *Curr. Opinion Drug Disc. Develop.*, 2007, **10**, 67.

[43] T.L. Poulos, B.C. Finzel, A.J. Howard, *J. Molecular Biol.*, 1987, **195**, 687.

[44] I.G. Denisov, T.M. Makris, S.G. Sligar, I. Schlichting, *Chem. Rev.*, 2005, **105** 2253.

[45] A.R. Dunn, I.J. Dmochowski, A.M. Bilwes, H.B. Gray, B.R. Crane

[46] Y.F. Gao, J.Y. Chen, *J. Electroanal. Chem.*, 2005, **578**, 129.

[47] M. J. Bonné, J.E. Taylor, A.K. Carver, M. Helton, F. Marken, *J. Electroanal. Chem.*, 2007, **601**, 211.

8. Electrochemical Characterisation of TiO_2 Nanotubes

8.1 Introduction

Titanium dioxide is a commercial material with diverse applications[1]. Titanium dioxide occurs in different structural types and can be engineered into many different forms such as nanoparticles, exfoliated nano-sheets[2,3], nano-fibers[4], sol-gels[5], surfactant-templated structures[6], and nanotubes[7]. TiO_2 nanotubes are a novel and structurally organised nanosized material which are synthesised under alkaline hydrothermal conditions[8]. In this synthesis the starting material, anatase, is partially dissolved into sheets, which are then proposed to fold back into nanotube-like structures due to the asymmetric distribution of hydrogen[9] or because of mechanical tensions arising during dissolution-crystallisation[10]. By varying the synthesis conditions (temperature, TiO_2 concentration, pH) the process can be controlled to give nanotube materials with differing diameters and degrees of porosity[10]. The resulting nanotube material when treated with acid may be structurally described as monoclinic titanate $H_2Ti_3O_7$[11] which implies the presence of labile protons and cation exchange capability[12,13]. Due to the unusual nanotubular structure and the interesting physicochemical properties of TiO_2 nanotubes, there are many possible applications emerging including gas adsorption[14], as a substrate for catalysis[15,16], in battery materials[17,18,19], in dye-sensitised solar cells[20], as a hydrogen gas sensor[21], and in photocatalysis[22,23].

The electrochemical properties of TiO_2 nanotubes can be expected to be very similar to those of mesoporous films of TiO_2 nanoparticles[24] despite the fact that optical properties are different due to the quantum size effects[25]. Relatively little electrochemical information is available about the TiO_2 nanotubes and it is shown here that electrochemical experiments with deposits of TiO_2 nanotubes immobilised onto boron-doped diamond substrates can be readily conducted. In this manner electron transfer and conductivity, as well as adsorption of redox active cations onto the nanotube surface can be assessed and quantified.

In this chapter experiments are described in which both TiO_2 nanotubes and TiO_2 nanoparticles are immobilised by suspension evaporation onto an inert boron-doped diamond electrode and immersed into aqueous electrolyte solutions. Voltammetric experiments demonstrate very similar characteristics for the Ti(IV/III) redox system in both forms of TiO_2. In contrast, adsorption of cations in neutral media is shown to be efficient only for TiO_2 nanotubes. The number of cation binding sites is compared to the number of replaceable protons in the TiO_2 nanotube structure. Binding is demonstrated to be very effective for the redox protein cytochrome *c* which is immobilised in electrochemically active form.

8.2 Experimental

8.2.1 Chemical Reagents

Medola's blue (Aldrich), phytic acid (*myo*-insitolhexakis(dihydrogen phosphate) dodecasodium salt hydrate), perchloric acid (70% A.C.S reagent), $NaClO_4$, $NiNO_3$, NaOH (all Aldrich), ethanol (Fisher Scientific, HPLC grade), cytochrome *c* (Sigma) were obtained commercially and used without further purification. TiO_2 nanoparticle sol (ca. 6 nm diameter, anatase, 30-35% in aqueous HNO_3, pH 0-1, TKS-202) was obtained from Tayca Corporation Japan. Both the TiO_2 nanoparticles and TiO_2 nanotubes were prepared by sonication (20 kHz Fisherbrand ultrasonic bath) as 3 % wt aqueous suspensions. All solutions were prepared using deionised water with a resistivity of not less than 15 MΩ cm.

8.2.2 Instrumentation

Electrochemical experiments were conducted with a PGSTAT 30 Autolab system (Eco Chemie, Netherlands) in a 100 mL three-electrode cell. The counter electrode was platinum gauze and the reference electrode was a saturated calomel electrode (SCE, Radiometer). Polycrystalline boron-doped diamond with a mirror finish polish (mineral acid treated, doping level ca. 10^{20} cm^{-3}, Windsor Scientific, Slough, UK) was obtained in the form of plates (5mm × 5mm × 0.6mm) for electrochemical experiments (mounted with silver epoxy back contact in epoxy) and in the form of 3 mm diameter disks (for SEM imaging experiments). Zeta potential measurements

were obtained with a ZetaPlus Zeta Potential Analyser (Brookhaven Instruments Corporation) using the ZetaPals method. Zeta potential values were reported after calculation using the Smoluchowski equation. Average electrophoretic mobilities were determined (10 cycles per run) in disposable plastic curvettes (10mm path length), each sample was run 10 times. The aqueous solution was thoroughly de-aerated with argon (Pureshield, BOC) prior to conducting experiments. Experiments were conducted at 22 ± 2°C. For Field Emission Gun Scanning Electron Microscopy (SEM) a Leo 1530 system was used. Samples were prepared by scratching (to reveal a film cross section) and gold sputter coating prior to analysis. The BET area and BJH pore size distribution of the samples was measured, using nitrogen adsorption, on a Micromeritics ASAP 2010 instrument.

8.2.3 TiO_2 Nanotube Synthesis

TiO_2 nanotubes were prepared following a literature procedure[10]. Briefly, 20 g of titanium dioxide (anatase) was added to 300 mL 10 M NaOH solution and heated for 22 hours at 140 °C in a Teflon linen autoclave. The white, powdery TiO_2 was thoroughly washed with water then with 0.05 M H_2SO_4, followed by vacuum-drying at 80 °C. (All TiO_2 nanotubes used in this thesis were prepared by Dmitry Bavykin).

8.3 Results and Discussion

8.3.1 Characterisation of TiO_2 Nanotubes

TiO_2 nanotubes are grown from a TiO_2 precursor under alkaline hydrothermal synthesis conditions. Figure 8.1A shows a typical SEM image of the tubular material with an outer tube diameter of typically 8-20 nm, inner diameter of 3-5 nm, and a tube length of up to several microns. These nanotubes have been found to possess a high surface area (BET: ca. 150 $m^2 g^{-1}$), porosity (BJH pore volume: ca. 0.41 $cm^3 g^{-1}$) and a structure related to $H_2Ti_3O_7$ or $Na_2Ti_2O_4(OH)_2$ or $H_2Ti_4O_9 \cdot H_2O$[26] rather than that of the starting material anatase. This change in structure and the availability of labile cations dramatically changes the surface characteristics and the ability of the TiO_2 nanomaterial to bind cations from solution.

In order to use well defined amounts of TiO_2 nanotubes for deposition onto boron-doped diamond surfaces, first an aqueous suspension was formed. The material is readily suspended (3 weight% in distilled water) in the presence of ultrasound. However, the nanotube material is mechanically fragile and smaller tube fragments are obtained after sonication. Figure 8.1B shows a typical image of a TiO_2 nanotube deposit formed by evaporation of suspension onto a flat boron-doped diamond electrode surface. The diamond surface is featureless and the TiO_2 nanotubes form a disordered thin layer with each tube being approximately 100 nm to 200 nm in length and typically 10 nm in diameter. The diameter appears slightly wider due to a thin gold coating applied prior to imaging. However, more accurate values have been determined by TEM.

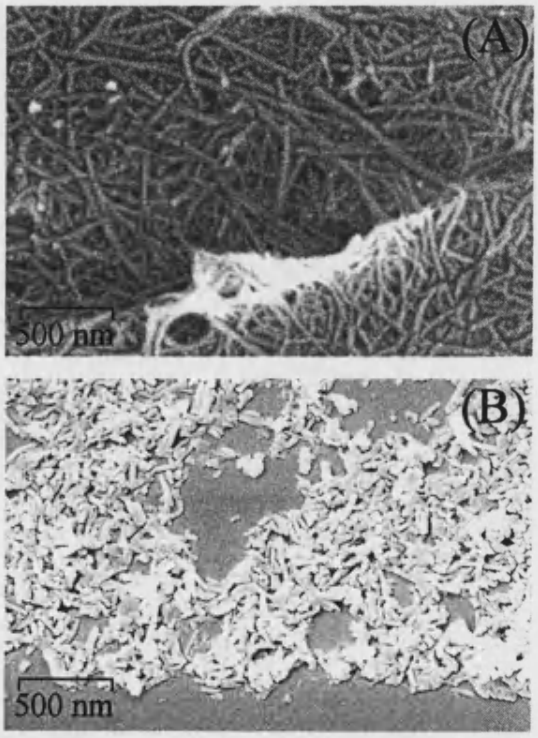

Figure 8.1 SEM images of (A) as grown TiO_2 nanotubes and (B) TiO_2 nanotubes treated with ultrasound and deposited from aqueous solution.

In contrast to TiO_2 (anatase) nanoparticles which are positively charged in neutral media (p.z.c. ca. 6[27]) and readily interact with negatively charged surfaces or ions, TiO_2 nanotubes from alkaline hydrothermal synthesis are negatively charged and interact with cationic species. The reason for this distinctive behaviour is the

presence of cation binding sites which have formed during hydrothermal synthesis in the presence of NaOH (incorporation of Na^+). For the suspension in water the zeta potential can be determined as -43 mV (pH 8). By adjusting the pH with NaOH and H_2SO_4 a zeta potential of -37 mV (pH 11.5) and +7 mV (pH 2.3) were determined, respectively. Therefore the average point of zero charge of ca. 3 can be estimated in agreement with a material which is negatively charged over most of the pH range. In order to further quantify the number of acidic sites in the structure a titration curve was recorded with 0.05 M NaOH (see Figure 8.2). It can be seen that the protons in the TiO_2 nanotube structure can be gradually replaced. At pH 7 approximately 2×10^{-3} mol g^{-1} are consumed to replace acidic protons in the structure (corresponding to 25% of all protons in $H_2Ti_3O_7$) and the process continues in more alkaline solution. Protons from throughout the structure appear to be labile.

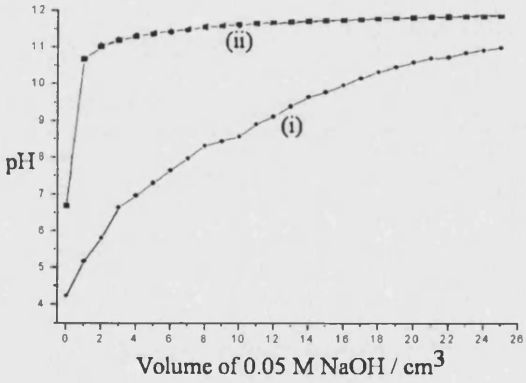

Figure 8.2 Plot of the titration curve for (ii) the blank and (i) 0.1 g TiO_2 nanotubes dispersed in water. Data provided by Dmitry Bavykin.

A considerable amount of labile protons and binding sites for cations exist and it is interesting to explore the ability of cations to bind to this TiO_2 nanotube surface. Only a fraction of the labile protons will be available at the surface as electrostatic cation binding sites and this number can be determined via voltammetric measurements and for several types of cations.

8.3.2 Electrochemical Characterisation of TiO_2 Nanotubes Deposited onto Boron-Doped Diamond Electrodes

After deposition of the TiO_2 nanotubes or TiO_2 (anatase) nanoparticles onto a suitably inert electrode surface such as boron-doped diamond, a characteristic reduction response can be observed in voltammetric experiments (see Figure 8.3). Deposits of anatase nanoparticles on polished boron-doped diamond immersed in aqueous 0.1 M $NaClO_4$ / 2 mM $HClO_4$ are shown to exhibit a reduction commencing at a potential of ca. -0.7 V vs. SCE (see Figure 8.3A). The process is associated with a Ti(IV/III) type reaction and conduction of electrons through the oxide[28]. Figure 8.3A shows voltammetric responses for the reduction of different amounts of TiO_2 immobilised at a 25 × 10^{-6} m^2 electrode at a scan rate of 100mVs^{-1}. A characteristically shaped signal is observed consistent with a reversible transfer of electrons from the electrode to anatase accompanied by adsorption of protons. For a higher surface coverage with TiO_2 nanoparticles the voltammetric response increases in magnitude but the effect is non-linear.

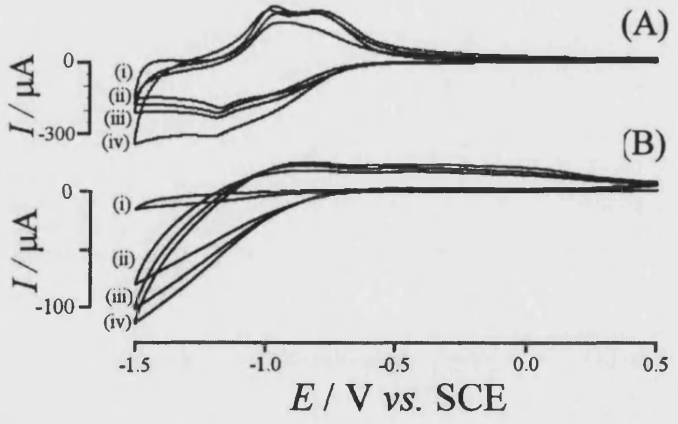

Figure 8.3 Cyclic voltammograms (scan rate 100 mVs^{-1}) for the reduction of (A) TiO_2 nanoparticles and (B) TiO_2 nanotubes immobilised at boron-doped diamond electrodes and immersed in 0.1 M $NaClO_4$ / 2 mM $HClO_4$ for (i) 15 μg, (ii) 30 μg, (iii) 45 μg, and (iv) 60 μg deposit.

For a deposit of TiO_2 nanotubes a similar electrochemical response is obtained compared to that for anatase. Figure 8.1 shows SEM images of the TiO_2 nanotubes on boron-doped diamond deposited in a highly non-uniform way. This non-

uniformity of the deposit as well as some loss due to material dislodged from the surface is believed to cause some irreproducibility. However, the Ti(IV/III) reduction is clearly observed. The voltammetric response observed in aqueous 0.1 M $NaClO_4$ / 2 mM $HClO_4$ appears less reversible (see Figure 8.3B) when compared to the response observed for anatase nanoparticles (see Figure 8.3A). The drawn-out shape of the voltammetric signal may be attributed to a slow transfer of electrons between boron-doped diamond substrate and TiO_2 rather than to an intrinsic property of the TiO_2 nanotubes. Similar experiments conducted with tin-doped indium oxide (ITO) electrodes rather than boron-doped diamond substrates also show very similar and almost reversible behaviour for both materials, nanoparticles and nanotubes (not shown). In summary, at a potential where Ti(IV/III) reduction occurs TiO_2 nanotubes exhibit an electrochemical reactivity similar to that of anatase. However, the ability of TiO_2 nanotubes to bind cations is dramatically different when compared to anatase. Next, the ability of TiO_2 nanotubes to adsorb cations (in contrast to anatase which binds anions) will be explored further.

8.3.3 Adsorption and Electrochemistry of Medola's Blue at TiO_2 Nanotube Surfaces

The redox mediator[29,30,31] and dye Medola's blue has been used previously to modify electrodes. Meldola's blue has been used successfully in the design of an amperometric sensor for glucose[32] and for NADH[33] determinations. Meldola's blue is a cation in the oxidised (coloured) state and readily adsorbs onto negatively charged surfaces[34]. Electrochemical studies show that in aqueous media Medola's blue undergoes a two-electron reduction and shows a stable and reversible signal at pH dependent potential[35]. The reduced form of Meldola's blue is protonated with a pK_A of approximately 5 (see figure 8.4).

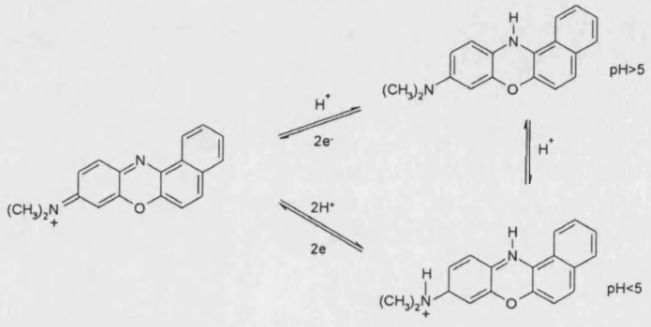

Figure 8.4 Schematic showing oxidation states of Medola's blue.

Medola's blue dissolved in water readily adsorbs onto negatively charged TiO_2 nanotube surfaces (immobilised at boron-doped diamond surfaces) but does not adsorb onto positively charged TiO_2 nanoparticles. Figure 8.5 shows typical voltammetric responses (10 continuous potential cycles) for the reduction of Meldola's blue adsorbed onto 1.5 μg TiO_2 nanotubes and immersed in (A) aqueous 0.1 M $NaClO_4$ and (B) 0.1 M $NaClO_4$/ 0.002 M $HClO_4$. During the reduction a well defined response is observed. Overall the reduction is accompanied by some loss of the reduced form of Meldola's blue from the surface during continuing potential cycling. This effect is less significant in the presence of protons due to the positive charge which is maintained after reduction in the presence of acid (see Figure 8.5B).

In order to quantify the adsorption process and to carry out surface charge measurements, the adsorption of the Medola's blue onto the TiO_2 nanotubes was investigated in more detail. The effect of varying the amount of Meldola's blue on the electrode surface is shown in Figure 8.5C. The amount of TiO_2 nanotubes clearly changes the magnitude of the voltammetric response but for deposits of more than 5 μg the effect becomes non-linear. The error in measurements is mainly due to the non-uniformity of the deposit. From the plot in Figure 8.5D it can be seen that the surface coverage of TiO_2 nanotubes with Meldola's blue is approximately 7×10^{-5} mol g^{-1}.

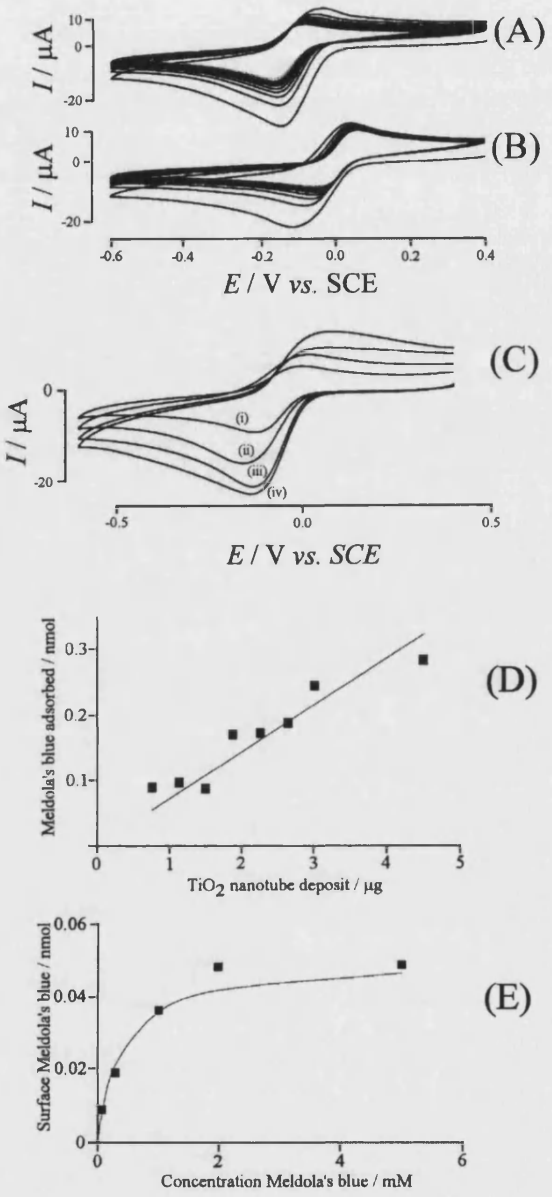

Figure 8.5 (A) Cyclic voltammograms (scan rate 100 mV s^{-1}) for 1.5 μg nanotubes immobilised on boron-doped diamond, immersed in 2 mM Medola's blue, and transferred to 0.1 M $NaClO_4$. (B) Voltammograms as in (A) but transferred into 0.1 M $NaClO_4$/2 mM $HClO_4$. (C) Cyclic voltammograms (scan rate 100 mV s^{-1}) for (i) 0.75 μg, (ii) 1.5 μg, (iii) 2.25 μg, and (iv) 3.0 μg nanotubes immobilised on boron-doped diamond, immersed in 2 mM Medola's blue, and transferred to 0.1 M $NaClO_4$. (D) Plot of the charge under the reduction peak versus the amount of TiO_2 nanotubes immobilised at the boron-doped diamond surface. (E) Plot of the charge under the reduction peak versus the concentration of Meldola's blue in the adsorption solution.

Next, for a fixed amount of 0.75 μg TiO_2 nanotubes deposited onto boron-doped diamond the concentration of Meldola's blue in the deposition solution was varied. The electrode was immersed for 5 minutes, rinsed with water, and transferred into an aqueous 0.1 M $NaClO_4$ solution. The charge under the first reduction peak was evaluated and is plotted against the concentration of Meldola's blue in the deposition solution (see Figure 8.5E). A Langmuirian model gives a reasonable fit and the parameters for adsorption, binding constant $K_{Meldola's\ blue}$ = 2500 $mol^{-1}dm^3$ and surface concentration 7 × 10^{-5} mol g^{-1} are obtained (see Table 8.1). It is interesting to compare this value with the approximate BET surface area 150 m^2 g^{-1} for this material, which suggests an area of ca. 19 Å × 19 Å per Meldola's blue molecule (or per negative charge on the surface). This value is not unreasonable when accounting for the probably less accessible surface area within tubes (the true molecular area is approximately 8 Å × 14 Å). It is interesting to compare these results with data for other types of adsorbed cations.

Table 8.1 Data for adsorption of cationic redox systems onto TiO_2 nanotubes.

Redox System	**Binding Constant** [a] **/ mol^{-1} dm^3**	**Binding Sites** [b] **/ mol g^{-1}**	**Adsorption Conditions**
Meldola's blue	2500 ± 700	7 ± 2 × 10^{-5}	Aqueous solution, 5 minutes, 1.5 μg
Ni^{2+}	250 ± 100	4 ± 2 × 10^{-5}	Aqueous solution, 5 minutes, 15 μg
Cytochrome *c*	2 ± 1 [c]	0.9 ± 0.2 × 10^{-5}	Aqueous solution, 5 minutes, 30 μg

[a] approximate, assuming Langmuirian adsorption (errors estimated). [b] number of +1 binding sites determined voltammetrically (errors estimated). [c] this apparent binding constant does not correspond to a true equilibrium value.

8.3.4 Adsorption and Electrochemistry of Ni^{2+} at TiO_2 Nanotube Surfaces

Next, the adsorption of a transition metal cation, Ni^{2+}, from aqueous solution onto TiO_2 nanotube surfaces is investigated. Similar to the adsorption of Ni^{2+} into cation adsorbing clay materials[36], adsorption onto cation adsorbing TiO_2 nanotubes occurs

readily. The TiO_2 nanotube material may be regarded as a support of electrocatalytically active nickel. In order to quantify the amount of nickel adsorbed from neutral aqueous solution, an alkaline electrolyte system, 1 M NaOH, was employed as the electrolyte for voltammetric measurements. Ni^{2+} was adsorbed for 5 minutes from 20 mM aqueous solution onto TiO_2 nanotubes immobilised at boron-doped diamond electrodes, rinsed with water, and transferred into aqueous 1 M NaOH. Under these conditions the Ni(II) hydroxide is oxidised reversibly to a catalytically active Ni(III) hydroxide (see equation 8.1[37]) and the magnitude of the voltammetric response can be taken as a measure of the amount of immobilised nickel.

$$Ni(OH)_2 = NiO(OH) + e^- \quad (8.1)$$

Initial tests showed that in the absence of TiO_2 nanotubes essentially no Ni^{2+} adsorption onto the freshly polished boron-doped diamond surface occurred. Figure 8.6A shows typical voltammetric responses (scan 1 and scan 4 are shown). The oxidation and reduction are observed at 0.32 V and 0.27 V vs. SCE, respectively. The shape of the signal changes from the first to later potential cycles presumably due to structural changes during the initial oxidation. In similar experiments it was established that under these conditions the Ni^{2+} ions did not adsorb onto the surface of TiO_2 nanoparticles (see Figure 8.6B).

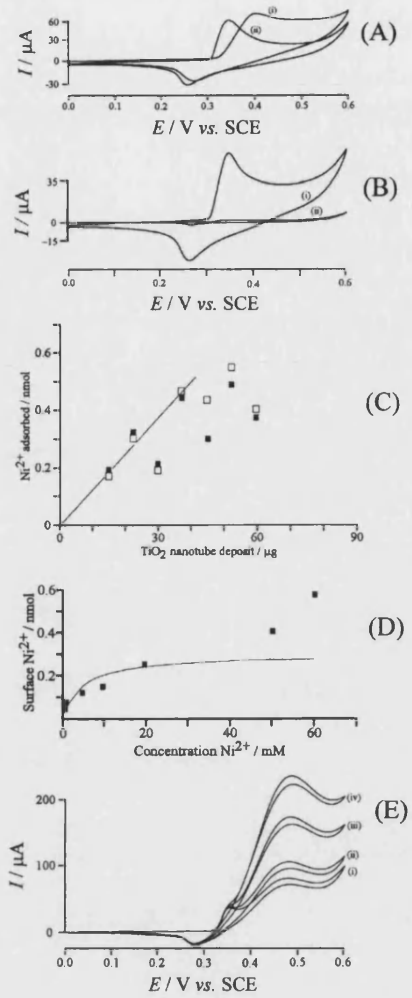

Figure 8.6 (A) Cyclic voltammograms (scan rate 100 mV s^{-1}, (i) first cycle, (ii) fourth cycle) for the oxidation of Ni^{2+} immobilised (5 minutes in 20 mM Ni^{2+}) on 15 μg TiO_2 nanotubes and immersed in 1M NaOH. (B) Cyclic voltammograms (scan rate 100 mV s^{-1}) for the oxidation of Ni^{2+} immobilised on (i) 15 μg TiO_2 nanotubes and (ii) 15 μg anatase nanoparticles. (C) Plot of the charge under the oxidation (black square) and the reduction (open square) peak obtained from voltammograms (100 mV s^{-1}) for variable amounts of TiO_2 nanotubes immobilised at boron-doped diamond electrodes, immersed for 5 minutes in 20 mM Ni^{2+}, and transferred into 1 M NaOH. (D) Plot of the charge under the reduction peak obtained from voltammograms (scan rate 100 mV s^{-1}) for 15 μg TiO_2 nanotubes immobilised at boron-doped diamond electrodes, immersed in Ni^{2+} solutions with variable concentration, and transferred into 1 M NaOH. (E) Cyclic voltammograms for the oxidation of (i) 100 mM, (ii) 150 mM, (iii) 300 mM, and (iv) 500 mM ethanol in 1 M NaOH at a boron-doped diamond electrode with 30 μg TiO_2 nanotubes immobilised after immersion into 20 mM Ni^{2+} solution.

The adsorption of the Ni^{2+} ions onto the TiO_2 nanotubes was further investigated in order to determine the saturation concentration of nickel ions on the TiO_2 surface. When the amount of nanotubes immobilised on the BDD electrode was varied it was found that the nickel oxidation response generally increased with increasing amounts of nanotubes. From the limiting values (assuming that some dislodged TiO_2 material and non-homogeneity are responsible for the error) the surface coverage of ca. 1.3×10^{-5} mol g^{-1} can be estimated (using a 20 mM Ni^{2+} solution and 5 minutes immersion for adsorption). By varying the concentration of Ni^{2+}, the adsorption of nickel ions was found to be inconsistent with a Langmuirian isotherm (see Figure 8.6D) in particular at high Ni^{2+} concentrations. However, when forced into the data, the isotherm suggests a binding constant of ca. 200 mol^{-1} dm^3 and the number of binding sites 0.3 nmol for 15 µg TiO_2. This corresponds to a number of cationic binding sites of 4×10^{-5} mol g^{-1} which is in good agreement with the value obtained for Meldola's blue (see Table 8.1). The value of cation binding sites determined here may be regarded as evidence for purely electrostatic binding. However, as shown by the titration experiment there are approximately 100-fold more cation binding sites and depending on the metal cation and adsorption conditions these can become available[38]. The deviation from Langmuirian adsorption could be associated with Ni^{2+} accessing more binding sites at higher Ni^{2+} concentration. Further work addressing the nature of binding sites and the effect of time on the adsorption process are in progress.

Previous studies have shown that nickel redox systems may act as a mediator for the oxidation of alcohols in alkaline media[39,40] and Ni^{2+} immobilised onto TiO_2 nanotubes shows a similar effect. When ethanol is added into the aqueous 1 M NaOH solution, a strong oxidation current commences at a potential where the Ni(III) is formed (see Figure 8.6E). Similar experiments with only TiO_2 nanotubes or bare boron-doped diamond confirm that Ni(III) is essential for the oxidation to be observed. In the presence of ethanol an additional irreversible oxidation peak is present at +0.4 V vs. SCE directly following the oxidation of the Ni^{2+} and therefore Ni^{2+} adsorbed onto TiO_2 nanotubes is acting as an electrocatalyst. The amount of ethanol added to the electrolyte solution was varied and the voltammetric response for the oxidation of the ethanol was found to increase approximately linearly within the concentration range 10 mM to 500 mM.

8.3.5 Adsorption and Electrochemistry of Cytochrome c at TiO_2 Nanotube Surfaces

Experiments with the redox protein cytochrome *c* are conducted in order to establish the ability of TiO_2 nanotubes to act as a novel substrate for biological redox systems. Ferrocytochrome *c* is a redox protein with a diameter of ca. 3.4 nm[41], an overall charge at neutral pH of +9[42], and the ability to reversibly exchange one electron from a covalently bound heme unit.

$$\text{Fe(III) cytochrome } c + e^- \rightleftharpoons \text{Fe(II) cytochrome } c \qquad (8.2)$$

It has previously been shown that cytochrome *c* can be surface immobilised by electrostatic interaction[43] and that it remains active on a range of electrodes with negative surface functionalities such as carboxylate[44], polysulfonates[45], polyphosphate (DNA)[46], and phytic acid modified surfaces[47]. The positively charged lysine-rich region of the protein is responsible for docking the protein to complementary negatively charged surfaces and enabling electron transfer (in nature with cytochrome *c* oxidase). Cytochrome *c* may be considered as a model system for biological electron transfer and bioelectrocatalysis due to similarities with other heme-type redox proteins.

Boron-doped diamond electrodes were prepared by immobilising various amounts on TiO_2 nanotubes onto the boron doped diamond electrode surface and immersion into in a solution of cytochrome *c* for 5 minutes. The electrode was rinsed and cyclic voltammetry performed in aqueous phosphate buffer at pH 7. In the absence of TiO_2 nanotubes no signal for cytochrome *c* was detected. This is consistent with a previous study showing that diffusion controlled electron transfer between boron-doped diamond and cytochrome *c* occurs without strong interaction[48]. Figure 8.7A shows cyclic voltammograms for the reduction of cytochrome *c* immobilised onto 30 μg TiO_2 nanotubes after immersion into aqueous solutions of cytochrome *c* containing 0.1 mM, 0.3 mM, and 0.8 mM of the protein. A well-defined and reversible response with E_{mid}= 0.01V vs. SCE is detected and is consistent with earlier reports for cytochrome *c* immobilised in mesoporous TiO_2 films[49]. The voltammetric signal is stable over prolonged periods of potential cycling and

therefore loss of the protein from the surface after immobilisation appears to be insignificant. The resistive nature of the voltammetric signals (broad peaks and increasing peak-to-peak separation with increasing amounts of deposit) may be attributed to sluggish electron transfer between TiO_2 and the boron-doped diamond substrate rather than transfer between cytochrome *c* and TiO_2 nanotubes. Varying the scan rate (see Figure 8.7B) results in an approximately linear increase in current consistent with a surface immobilised redox system. For increased amounts of TiO_2 nanotubes immobilised onto the boron-doped diamond electrode the peak height increases. However, at approximately 30 μg a limit is reached.

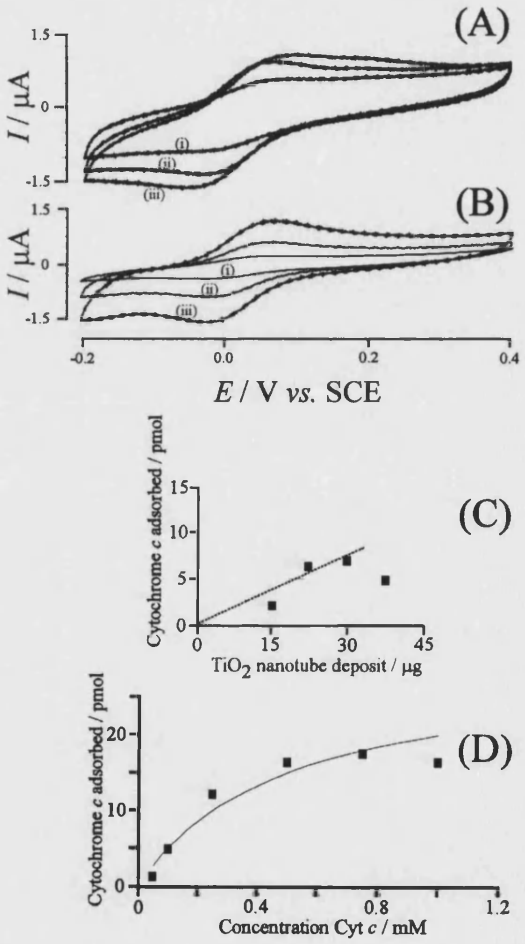

Figure 8.7 (A) Cyclic voltammograms (scan rate 100 mV s^{-1}) in 0.1 M phosphate buffer pH 7 for the reduction and oxidation of cytochrome *c* on 30 μg TiO_2 nanotubes on boron-doped diamond immobilised by 5 minute immersion into (i) 0.1 mM, (ii) 0.3 mM, and (iii) 0.8 mM solution. (B) Cyclic voltammograms (scan rates (i) 10, (ii) 50, and (iii) 100 mV s^{-1}) in 0.1 M phosphate buffer pH 7 for the reduction and oxidation of cytochrome *c* immobilised from 0.5 mM solution onto 30 μg TiO_2 nanotubes on boron-doped diamond. (C) Plot of the charge

under the cytochrome *c* reduction peak versus the amount of TiO_2 nanotubes immobilised at the boron-doped diamond electrode. (D) Plot of the charge under the cytochrome *c* reduction peak for 30 μg TiO_2 nanotubes immobilised, immersed into cytochrome *c* solutions of variable concentration, and transferred into 0.1 M phosphate buffer pH 7.

From the effect of concentration on the voltammetric response (see Figure 8.7D) it can be seen that a limit of approximately 30 pmol on 30 μg TiO_2 nanotube deposit exists and therefore a limit of 1×10^{-6} mol g^{-1} adsorption (this value is not optimised for time dependence or other parameters affecting the immobilisation). When taking into account the charge of overall +9 the number of cationic sites determined with cytochrome *c* is 0.9×10^{-5} mol g^{-1}, which is lower than values observed with Meldola's blue and Ni^{2+} (see Table 8.1). However, the size of cytochrome *c* restricts the binding sites in the TiO_2 nanotube deposit and a "full" coverage is unlikely to be achieved with the adsorption methodology.

8.4 Conclusions

TiO_2 nanotube material has been shown to act as a versatile substrate material for the immobilisation of cationic redox systems. The availability of cationic sites has been determined as approximately 7×10^{-5} mol g^{-1}. A much higher number of labile protons (2×10^{-3} mol g^{-1}) within the TiO_2 nanotube structure suggests that an even higher loading with catalytically active Ni^{2+} can be achieved under more forceful conditions. The ability of TiO_2 nanotubes to conduct electrons at sufficiently negative potentials and to act as a support for redox proteins such as cytochrome *c* suggests future applications in biosensors.

8.4 References

[1] A. Fujishima, K. Hashimoto, T. Watanabe, *TiO_2 photocatalysis fundamentals and applications*, BKC, Tokyo, 1999.

[2] W. Sugimoto, O. Terabayashi, Y. Murakami, Y. Takasu, *J. Mater. Chem.*, 2002, **12**, 3814.

[3] Sakai, N.; Ebina, Y.; Takada, K.; Sasaki, T., *J. Am. Chem. Soc.*, 2004, **126** 5851.

[4] Z.Y. Yuan, B.L. Su, *Colloids Surf. A*, 2004, **241**, 173.

[5] G.F. Fu, P.S. Vary, C.T. Lin, *J. Phys. Chem. B*, 2005, **109**, 8889.

[6] T. Sreethawong, Y. Suzuki, S. Yoshikawa, *J. Solid State Chem.*, 2005, **178** 329.

[7] D. Gong, C.A. Grimes, O.K. Varghese, W. Hu, R.S. Singh, Z. Chen, E. C. Dickey, *J. Mater. Res.*, 2001, **16**, 3331.

[8] T. Kasuga, M. Hiramatsu, A. Hoson, T. Sekino, K. Niihara, *Langmuir*, 1998, **14**, 3160.

[9] S. Zhang, Q. Chen, L.-M. Peng, *Phys. Rev. B*, 2005, **71**, 014104.

[10] D.V. Bavykin, V.N. Parmon, A.A. Lapkin, F.C. Walsh, *J. Mater. Chem.*, 2004, **14**, 3370.

[11] Q. Chen, G.H. Du, S. L.-M. Zhang Peng, *Acta Cryst. B*, 2002, **58**, 587.

[12] X. Sun, Y. Li, *Chem. Eur. J.*, 2003, **9**, 2229.

[13] J.J. Yang, Z.S. Jin, X.D. Wang, W. Li, J.W. Zhang, S.L. Zhang, X.Y. Guo, Z.J. Zhang, *Dalton Trans.*, 2003, 20, 3898.

[14] D.V. Bavykin, in preparation.

[15] Lin CH, Chien SH, Chao JH, Sheu CY, Cheng YC, Huang YJ, Tsai CH, *Catal. Lett.*, 2002, **80**, 153.

[16] V. Idakiev, Z.-Y. Yuan, T. Tabakova, B.-L. Su, *Appl. Catal. A*, 2005, **281,** 149.

[17] L. Kavan, M. Kalbac, M. Zukalova, I. Exnar, V. Lorenzen, R. Nesper, M. Grätzel, *Chem. Mater.*, 2004, **16**, 477.

[18] Y.G. Wang, X.G. Zhang, *J. Electrochem. Soc.*, 2005, **152**, A671.

[19] G. Armstrong, A.R. Armstrong, J. Canales, P.G. Bruce, *Chem. Commun.*, 2005, 2454.

[20] M. Adachi, Y. Murata, I. Okada, S. Yoshikawa, *J. Electrochem. Soc.*, 2003, 150, G488.

[21] O.K. Vardhese, D. Gong, M. Paulose, K.O. Ong, E.C. Dickey, C.A. Grimes, *Adv. Mater*, 2003, **15**, 624.

[22] C.-H. Lin, C.-H. Lee, J.-H. Chao, C.-Y. Kuo, Y.-C. Cheng, W.-N. Huang, H.-W. Chang, Y.-M. Huang, M.-K. Shih, *Catal. Lett.*, 2004, **98**, 66.

[23] J.-C. Xua, M. Lua, X.-Y. Guob, H.-L. Lia, *J. Mol. Catal. A*, 2005, 226, 123.

[24] F. Marken, A.S. Bhambra, D.H. Kim, R.J. Mortimer, S.J. Stott, *Electrochem. Commun.*, 2004, **6,** 1153.

[25] D.V. Bavykin, S.N. Gordeev, A.V. Moskalenko, A.A. Lapkin, F.C. Walsh,

J. Phys. Chem. B:, 2005, **109**, 8565.

[26] A. Nakahira, W. Kato, M. Tamai, T. Isshiki, K. Nishio, H. Aritani, *J. Mater. Sci.*, 2004, **39**, 4239.

[27] M. Kosmulski, *Adv. Coll. Interf. Sci.*, 2002, **99**, 255.

[28] F. Fabregat-Santiago, I. Mora-Sero, G. Garcia-Belmonte, J. Bisquert, *J. Phys. Chem. B*, 2003, **107**, 758.

[29] B. Prieto-Simon, E. Fabregas, Biosens. *Bioelectron.*, 2004, **19**, 1131.

[30] S. Sampath, O. Lev, *J. Elctroanal. Chem.*, 1998, **446**, 57.

[31] R. Wedge, R.M. Pemberton, J.P. Hart, R. Luxton, *Analusis*, 1999, **27**, 570.

[32] L.Q. Mao, K. Yamamoto, *Talanta*, 2000, **51**, 187.

[33] L.T. Kubota, F. Gouvea, A.N. Andrade, B.G. Milagres, G.D. Neto, *Electrochim. Acta*, 1996, **41**, 1465.

[34] C.U. Ferreira, J.E. Goncalves, R.A.C. Goncalves, A.J.B. de Oliveira, *J. New Mater. Electrochem. Syst.*, 2003, **6**, 251.

[35] C.U. Ferreira, Y. Gushikem, L.T. Kubota, *J. Solid State Electrochem.*, 2000, **4**, 298.

[36] B. Ballarin, R. Seeber, D. Tonelli, A. Vaccari, *J. Electroanal. Chem.*, 1999, **463**, 123.

[37] D.A. Corrigan, S.L. Knight, *J. Electrochem. Soc.*, 1989, **136**, 613.

[38] D.V. Bavykin, A.A. Lapkin, P.K. Plucinski, J.M. Friedrich, Frank C. Walsh, J. Catal., (2005) submitted.

[39] T.C. Wen, C.C. Hu, Y.J. Li, *J. Electrochem. Soc.*, 1993, **140**, 2554.

[40] Y.C. Weng, T.C. Chou, *J. Electrochem. Soc.*, 2003, **150**, C385.

[41] L. Stryer, *Biochemistry*, W.H. Freeman and Company, New York, 1995, p. 541.

[42] S. Imabayashi, T. Mita, T. Kakiuchi, *Langmuir,* 2005, **21**, 1470 and references cited therein.

[43] M. Fedurco, *Coord. Chem. Rev.*, 2000, **209**, 263.

[44] A. Avila, B.W. Gregory, K. Niki, T.M. Cotton, *J. Phys. Chem. B*, 2000, **104**, 2759.

[45] G.X. Li, H.R. Shi, H.Q. Fang, H.Y. Chen, D.X. Zhu, *Anal. Lett.*, 1997, **30**, 235.

[46] T.Y. Lee, H.J. Kim, J.O. Moon, Y.B. Shim, *Electroanalysis*, 2004, **16**, 821.

[47] K.J. McKenzie, F. Marken, *Langmuir*, 2003, **19**, 4327.

[48] F. Marken, C.A. Paddon, D. Asogan, *Electrochem. Commun.*, 2002, **4**, 62.

[49] K.J. McKenzie, F. Marken, M. Opallo, *Bioelectochem.*, 2005, **66**, 41.

9. Probing pH-Sensitive Redox Processes in a Mesoporous TiO_2-Nafion Film Electrode with Fourier-Transform Large-Amplitude Sinusoidally Modulated Voltammetry

9.1 Introduction

Alternating current (ac) voltammetry, first introduced in the 1950s[1], and intensively developed by Smith[2], is in principle a far more powerful technique than the dc method for quantitative evaluation of electrode processes. An alternating potential (E_{ac} or ΔE) of known angular frequency (ω) is superimposed onto the waveform used in dc techniques, and the ac response measured as a function of dc potential and angular frequency to extract the kinetic and thermodynamic data. Consequently, a great deal of information additional to that available in dc voltammetry can be obtained[3].

Traditionally in ac techniques, such as impedance spectroscopy, theoretical treatment of data often requires the amplitude of the applied alternating potential to be small so that the solution may be linearised[4]. The use of a small ac amplitude gives rise to only extremely small second and higher harmonic current responses and the advantage of these higher harmonics (for example an ideally zero capacitive current or kinetic information at higher frequencies) can not be exploited.

Recently, however, ac voltammetric methods have undergone a considerable development, in particular with the availability of fast and affordable computing facilities[5, 6]. Instrumentation has been specifically developed that can exploit the attractive features of the large-amplitude method combined with fast Fourier-transformation. Complementary numerical simulations by Gavaghan et al[3] for all amplitudes of ac current has utilised the Fourier transform (FT) method of analysis to separate the dc signal and harmonics of the ac signal. Numerical simulations employing the same well known protocols applied in dc cyclic voltammetry combined with Fourier transform analysis then produce the dc and fundamental harmonic responses, in addition to resolved higher ac harmonics that emerge from non-linearities associated with the use of large-amplitude methods. The separation of

the dc and ac harmonics gives rise to patterns of behaviour that are intuitively obvious and has enabled a simple protocol to be developed to estimate uncompensated resistance (R_u), capacitance of the double layer (C_{dl}), and slow electron transfer kinetics (in particular, the reversible potential E^o, rate constant k_o, and α from the Butler-Volmer model)[7]. Already work carried out exploiting this method has included elucidating an EC mechanism of a biocatalytic process[8] and the electron transfer mechanism associated with surface bound proteins[9].

Here we use the method of large-amplitude sinusoidally modulated voltammetry (LASMV) to investigate the conductivity of a TiO_2-Nafion® film electrode (see chapter 3) and to probe the oxidation mechanism for immobilised ferrocenylmethyl-trimethylammonium$^+$ ($TMAFc^+$) within the TiO_2-Nafion® film. From traditional cyclic voltammetry two electrochemical processes for the oxidation of $TMAFc^+$ are seen, process 1 (a reversible one electron transfer of the $TMAFc^+$ present at the ITO surface), and process 2 (the irreversible reduction of $TMAFc^+$ by electron conduction through the TiO_2-Nafion® film). LASMV allows further study of these electron transfer processes and additionally the assignment of an EC′ mechanism for process 2 is made. Finally, the low capacitive background of the second harmonic response is exploited to simplify read-out of potential differences for the TiO_2-Nafion® film and immobilised $TMAFc^+$ over a range of pH values. Application of this system as a reference-free pH probe is explored.

9. 2 Experimental

9.2.1 Chemical Reagents

Nafion® perfluorinated ion-exchange resin (5%wt., in a mixture of lower aliphatic alcohols and H_2O), KCl, sodium acetate trihydrate, glacial acetic acid, ferrocenylmethyl-trimethylammonium iodide (all Aldrich) were obtained commercially and used without further purification. TiO_2 sol (ca. 6 nm diameter, anatase, 30-35% in aqueous HNO_3, pH 0.5, TKS-202) was obtained from Tayca Corp, Japan. Solutions were prepared using filtered and deionized water with a resistivity of not less than 18 MΩ cm.

9.2.2 Instrumentation

The Fourier transform (FT) ac voltammetric instrumentation utilised a conventional three-electrode potentiostat (Oxford Electrodes, UK) to generate the dc potential sweep. This was input into a 40MHz DDS function/Arbitary generator (Thurlby Thandar Instruments, Cambridgeshire, England) which added to the dc sweep the ac waveform. Input and output from the potentiostat was recorded on a deep memory oscilloscope (Agilent Technologies) with data transferred and processed on a personal computer. POT software (developed by D. Elton, La Trobe University, Melbourne) was used to perform the Fourier-transform inverse Fourier-transform calculations with data presented in the Origin (Microcal Software Inc) data graphics program. Conventional dc cyclic voltammetric experiments were undertaken with a microAutolab III system (Eco Chemie, Netherlands).

A standard three-electrode electrochemical cell was employed in all electrochemical experiments, with a saturated calomel reference electrode, SCE, (Radiometer, Copenhagen) placed ca. 0.5 cm from the working electrode and a 2 cm × 2 cm platinum gauze counter electrode. The working electrodes were made from tin-doped indium oxide (ITO) coated glass (10 mm × 60 mm, 15 Ω per square, Image Optics, Basildon, UK). The ITO electrode was rinsed with ethanol and water, heat treated in

a furnace (Elite Thermal Systems Ltd.) for 1 h at 500°C, and re-equilibrated to ambient conditions prior to use. Prior to voltammetric experiments, solutions were de-aerated with argon (BOC). All experiments were conducted at a temperature of 22 +/- 2°C.

9.2.3. Layer-by-Layer Formation of TiO_2 – Nafion® Nanocomposite Films

The deposition procedure followed a literature procedure (see chapter section 3.2.3) and consisted of a sequence of liquid immersion steps with (i) a TiO_2 sol (6 nm diameter, 3%wt in aqueous nitric acid, pH ca. 2) for 60 seconds followed by rinsing with distilled water and methanol, (ii) dipping into Nafion® anionomer solution (ca. 0.5 wt% in methanol) for ~10 seconds followed by rinsing with methanol and distilled water. This completed a single layer deposition for the simple TiO_2-Nafion® film and the cycle was repeated to add more layers. Each deposition cycle adds approximately 25nm thickness of mesoporous TiO_2-Nafion to the thin film electrode (see chapter 3.3.1).

9.3. Results and Discussion

9.3.1. Background LASMV Response of an ITO Electrode Coated with Mesoporous TiO_2-Nafion

Mesoporous TiO_2 films have been studied with voltammetric and impedance techniques (see chapter 2) and depending on the solution environment are known to undergo chemically reversible reduction processes. A typical dc cyclic voltammetric response is shown in Figure 9.1A. The onset of the reduction occurs at a potential of -0.6 V vs. SCE (in aqueous acetate buffer pH 5.5) and is observable with a very small current region (see P2). The main reduction process commences at ca. -0.7 V vs. SCE and is observed as an exponentially increasing current response (see P1). The process giving rise to this large reduction current has been described as a Ti(IV/III) process[10] (equation 9.1).

P1: $Ti(IV)O_2(bulk) + e^- + H^+(aq) \rightleftharpoons Ti(III)OOH(bulk)$ (9.1)

Accordingly, the small initial reduction current (see P2) can be identified as a process located at more readily reduced surface sites (equation 9.2).

P2: $Ti(IV)O_2(surface) + e^- + H^+(aq) \rightleftharpoons Ti(III)OOH(surface)$ (9.2)

These voltammetric reduction processes have been demonstrated to exhibit current magnitudes that are proportional to the amount of TiO_2 deposited at the electrode surface and to shift in potential by close to 59 mV per unit solution pH (in agreement with equations 9.1 and 9.2).

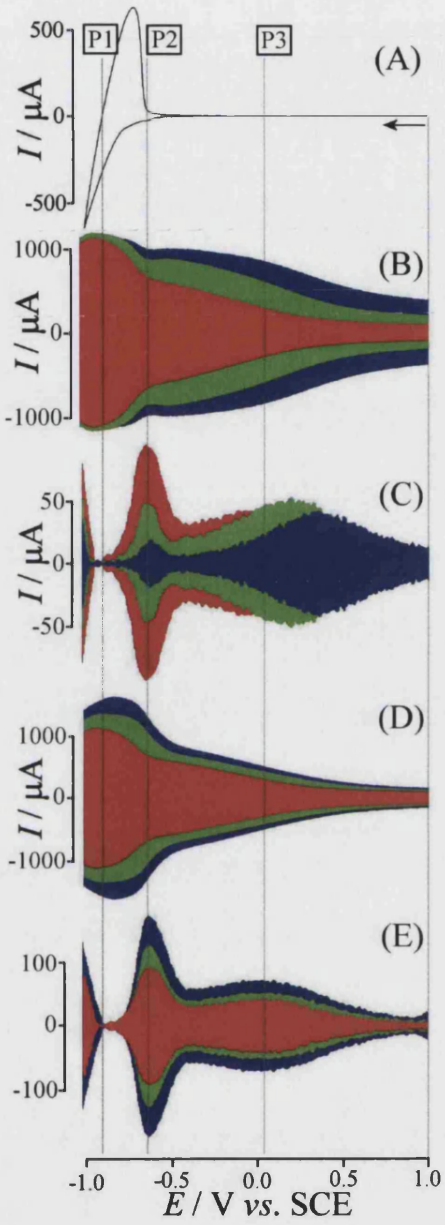

Figure 9.1 (A) Cyclic voltammogram and (B-E) LASMV voltammetric response for the reduction of a 20 layer TiO_2-Nafion electrode immersed in aqueous 0.1 M pH5.5 acetate buffer (scan rate $100mVs^{-1}$): (B) fundamental harmonic current response, (C) second harmonic current response (18Hz = red , 36Hz = green, 72Hz = blue) frequency and 400mV amplitude, (D) fundamental harmonic current response, (E) second harmonic current response (18Hz frequency, amplitude 200mV = red, 240mV = green, 280mV = blue).

An additional voltammetric response (see P3) is observed in LASMV data. This process is due to the tin-doped indium oxide (ITO) surface film on the substrate electrode. Data recorded with a bare electrode (not shown) shows the same feature

which is due to the increasing capacitance of the ITO (a highly degenerate n-type semiconductor). The fundamental harmonic in LASMV (see Figure 9.1B) strongly amplifies this background signal in comparison to the TiO_2 capacitive current contributions. Also in the second harmonic (see Figure 9.1C) a broad peak for P3 is observed over the range of 0 to +1V.

In large-amplitude sinusoidally modulated voltammograms (LASMV) of mesoporous TiO_2 several new features are observed. Figure 9.1B shows the first harmonic response as a function of the applied frequency. It can be seen that two processes, P1 and P3, show significant responses and as the frequency is increased (from 18Hz to 36Hz and to 72Hz) P3 increases whereas P1 seems constant. Both processes are believed to be essentially capacitive in nature (P1: charging of the TiO_2 surface and P3: charging of the ITO surface) and for a RC circuit element the increase in frequency is associated with a corresponding decrease in impedance[11] (equation 9.3).

$$|Z| = \sqrt{R^2 - \frac{1}{\omega^2 C^2}} \tag{9.3}$$

In this equation the total impedance of the RC element is determined by the resistance R, the capacitance C, and the angular frequency ω. For both an increase in frequency and an increase in capacitance a limit of impedance is reached at $|Z| = R$ and this can be observed in Figure 9.1B. The current amplitude is limited at approximately 1100 μA, which with an amplitude of 400 mV corresponds to a limiting resistance of R = 360 Ω. This limiting resistance reflects the typical resistance of the ITO conducting layer leading into the cell. This resistance effectively limits the current response in the first harmonic.

The second harmonic signal (see Figure 9.1C) shows a strong feature at the potential where process P2 is observed and it is likely to be associated with the Ti(IV/III) redox process (equation 9.2). Here, the current response *decreases* with higher frequency. The fact that this signal is highly sensitive to the frequency is a sign for irreversible electron transfer and transport within the TiO_2 film which is strongly

suppressed at higher frequencies. However, this current response is also coupled to the ITO resistance and inspection of Figure 9.1B shows that the current simply converges towards the limit imposed by the impedance. Therefore, the peak for P2 in the second harmonic will disappear as the current response in the first harmonic converges to a constant value. Process P3 appears to undergo a shift to more positive potentials with increasing frequencies which may be linked to the characteristic shape of the ITO capacitance response (compare Figure 9.1B and 9.1C).

Next, the effect of the sinusoidal amplitude is investigated (see Figure 9.1D and 9.1E). Increasing the amplitude from 400mV to 480mV and to 560mV generally increases the LASMV responses as expected for R and RC-type equivalent circuits. Only nodal zones in the second harmonic which reflect the maxima in the first harmonic responses remain zero, independent of the applied amplitude. In the next section the effects of an immobilised redox system within the mesoporous TiO_2-Nafion® film is investigated and compared to the well known LASMV characteristics for reversible solution redox systems.

9.3.2. LASMV Response of Ferrocenylmethyl-trimethylammonium$^+$ Immobilised into Mesoporous TiO_2-Nafion®

For solution redox systems with planar diffusion and with reversible electron transfer, data analysis for LASMV signals has been described and fully supported by computer simulation studies[7]. Here, immobilised redox systems within the TiO_2-Nafion® film deposit are investigated. The ferrocenylmethyl-trimethylammonium$^+$ cation ($TMAFc^+$) is readily immobilised by ion exchange adsorption onto the TiO_2-Nafion film (see chapter section 3.3.2). The reversible one electron transfer (equation 9.4) occurs as an apparently diffusion controlled process due to the electron hopping process typical for redox systems in Nafion[12]. Figure 9.2A shows the peak shaped responses (see P4) with peak currents approximately linear to the square root of the scan rate (not shown).

P4: $Fc^{2+}(Nafion) + e^-(ITO) \rightleftharpoons Fc^+(Nafion)$ (9.4)

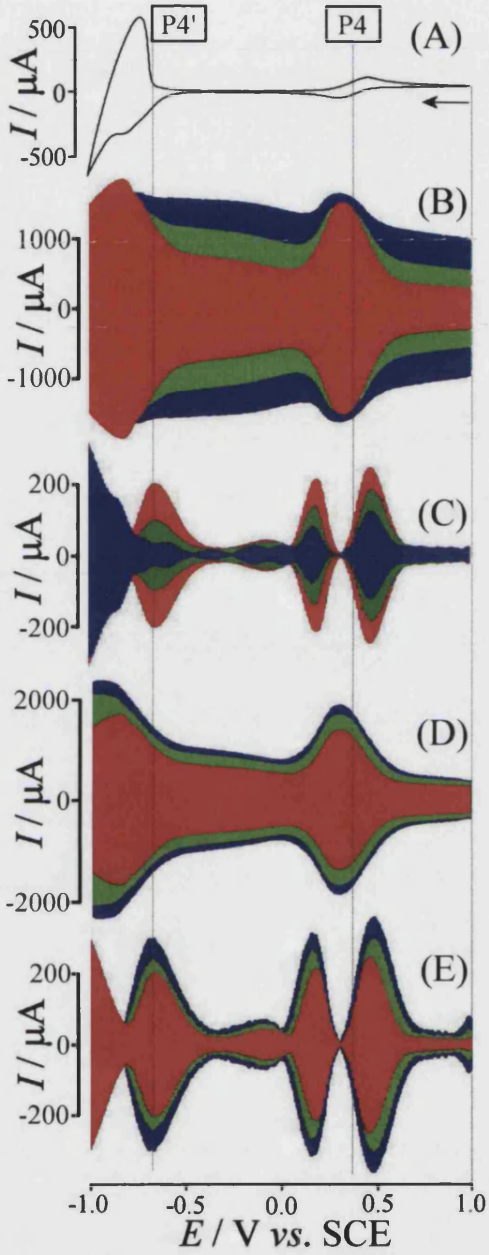

Figure 9.2 (A) Cyclic voltammogram and (B-E) LASMV voltammetric response for the oxidation and reduction of ferrocenylmethyl-trimethylammonium^{+} immobilised in a 20 layer TiO_2-Nafion® electrode (immersed in 0.1M acetate buffer pH5.5, scan rate 100mVs^{-1}): (B) fundamental harmonic current response, (C) second harmonic current response recorded at three different frequencies (18Hz = red, 36Hz = green, 72Hz = blue frequency) and with 400mV amplitude, (D) fundamental harmonic current response, and (E) second harmonic current response at 18Hz frequency and with three different amplitudes 200mV = red, 240mV = green, 280mV = blue).

In the first and second harmonic, LASMV responses (see Figure 9.2B and 9.2C) for ferrocenylmethyl-trimethylammonium$^+$ oxidation is clearly observed and the response shape is consistent with a diffusion controlled redox system. Voltammetric experiments conducted at a range of different scan rates result in a typical peak current versus square root scan rate dependence which supports this conclusion (see chapter section 3.3.3). The effect of frequency on the first and second harmonic are investigated first. In Figure 9.2B it can be seen that a clear peak feature for process P4 is observed only at lower frequencies and the reason for this behaviour can be found in the RC impedance limit (see section 9.3.1). The resistance R of the ITO film electrode again creates a cut-off current limit, in this case of approximately 1600 μA and only the frequency effect on the capacitive background is observed. In the second harmonic data (Figure 9.2C) the opposite effect is observed and the increase in frequency actually decreases the peak current. This decrease in second harmonic peak current is dominated by the ITO resistance effect and as the first harmonic response converges to a constant value the second harmonic converges to zero. The asymmetry of the response for P4 is readily explained based on the capacitive background for the ITO film which pushes the left of the current signal (at lower potentials) closer to the current cut-off.

A very interesting additional voltammetric feature is observed at a potential of -0.7 V vs. SCE very close to the onset of the TiO_2 reduction process (see P4'). Oxidised ferrocenyltrimethylammonium^{2+} is present within the TiO_2-Nafion matrix and not reduced in the process P4 due to the limited rate of charge diffusion within the mesoporous structure. However, at a potential of -0.7 V vs. SCE the electrical conductivity of TiO_2 is increased (due to the presence of new charge carriers) and the indirect reduction via TiO_2 becomes possible (P4′, see equation 9.5).

$$\text{P4}': \quad Fc^{2+}(\text{Nafion}) + e^-(TiO_2) \rightleftharpoons Fc^{+}(\text{Nafion}) \qquad (9.5)$$

The corresponding LASMV response for process P4′ is not observed in the fundamental harmonic but clearly visible as an increased response in the second harmonic (see Figure 9.2C). The fact that rather than creating a new signal for this process, the signal for P2 is simply increased suggests that these two processes are

linked and that P2 provides the conduction mechanism for the electrochemical process P4′ to occur. The mechanism is that of a EC′ process[13], however, with all reagent immobilized within the TiO_2-Nafion® film deposit.

The effect of frequency on the voltammetric signals is substantial in particular for the more irreversible signal P4′. This becomes almost invisible when going from a frequency of 18Hz to 72Hz. In contrast the amplitude parameter causes only minor changes in the LASMV responses (see Figure 9.2D and 9.2E). In the next section the effect of pH on the voltammetric response is explored.

9.3.3. LASMV Response of Ferrocenylmethyl-trimethylammonium$^+$ Immobilised into Mesoporous TiO_2-Nafion® as a Function of pH

It is well known that voltammetric processes are sensitive to proton activity if protons are involved in the chemical reaction steps before the rate determining process. Here, the reduction of TiO_2 is known to show a pH dependent shift. In contrast the oxidation of ferrocenylmethyl-trimethylammonium$^+$ is expected to be independent of solution pH. If both processes can be combined, a reference-free pH probe can be developed. The design of reference-free pH probes based on carbon electrodes has been reported recently[14] and the obvious benefit of this approach is the removal of the need for a precise and expensive reference electrode system.

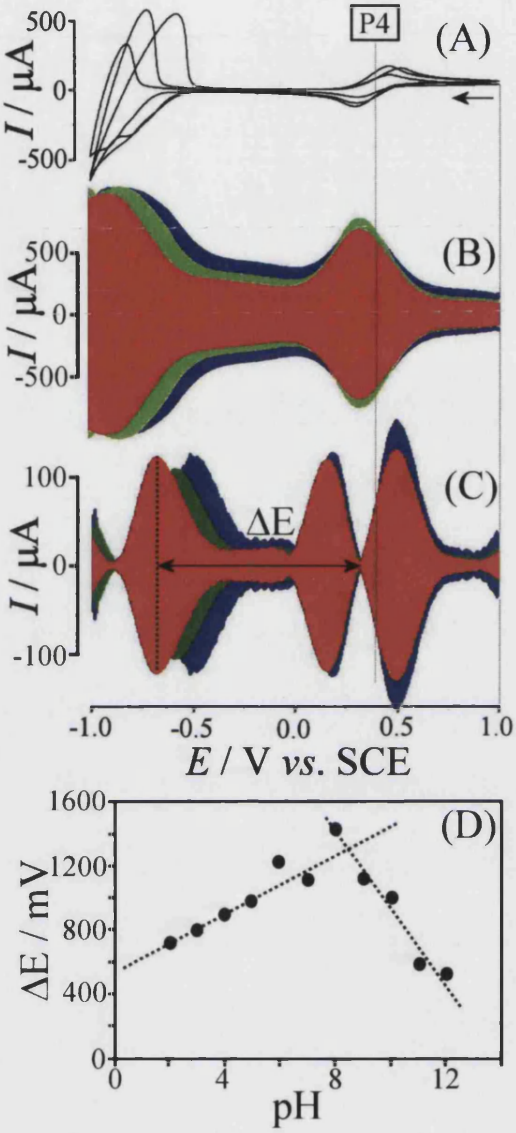

Figure 9.3 (A) DC cyclic voltammogram, (B) LASMV fundamental harmonic response, and (C) LASMV second harmonic response for the oxidation and reduction of ferrocenylmethyl-trimethylammonium^{+} immobilised in a 20 layer TiO_2-Nafion® electrode, immersed in aqueous 0.1M acetate buffer with pH4.5 (red), pH5.5 (green), and pH6.5 (blue) (scan rate 100mVs^{-1}, frequency 18Hz, amplitude 200mV). (D) Plot of the separation ΔE of the 2nd harmonic node for P4 and the peak for P2 versus pH in Britton-Robinson buffer.

Here, the use of LASMV is explored to simplify complex voltammetric responses and to simplify the read-out of potential differences in a reference-less pH probe. Figure 9.3 shows typical voltammetric and LASMV responses for a TiO_2-Nafion® electrode with the ferrocenylmethyl-trimethylammonium^{+} redox system

immobilised. In Figure 9.3A it can be seen that in contrast to the ferrocenylmethyl-trimethylammonium$^{2+/+}$ redox system, the TiO_2 reduction is clearly pH sensitive. The reduction response shifts to more negative potentials in increasingly alkaline conditions. However, the voltammetric response for the TiO_2 reduction is complex and the shift is very difficult to quantify. In the first harmonic (see Figure 9.3B) the potential shift in the TiO_2 response is more clearly observed and in the second harmonic (see Figure 9.3C) a well defined peak shift is observed.

Finally, measurements obtained over a wide pH range of 2-12 in Britton-Robinson buffer have been recorded. Figure 9.3D shows the potential separation of the second harmonic node for P4 and the peak for P2 with respect to pH. Over the range of pH2-8 there is a linear correlation between ΔE and pH, with a gradient of 90mV per pH unit. Above pH8 the potential shift becomes smaller and a relationship with a negative gradient is recorded. Although only useful over acidic pH range, the quantification of potential shift with pH is made possible only by analysing the second harmonic of the LASMV response.

9.4. Conclusions

Large amplitude sinusoidal modulated voltammetry (LASMV) has been applied to a complex electrode reaction with charge diffusion via hopping and electron transport via mesoporous TiO_2. The analysis of fundamental and second harmonic responses allow mechanistic conclusions and the evaluation of a pH sensitive parameter. In future LASMV could be employed in sensor devices to enhance and optimise detection current.

9.5 References

[1] D. C. Grahame, *Journal of Electroanalytical Chemistry*, 1952, **99**, 370c.

[2] D. E. Smith, in *Electroanalytical Chemistry*, ed. A. J. Bard, Marcel Dekker, New York, Editon edn., 1966, vol. 1.

[3] D. J. Gavaghan and A. M. Bond, *Journal of Electroanalytical Chemistry*, 2000, **480**, 133-149.

[4] A. J. Bard and L. R. Faulkner, *Electrochemical Methods: Fundamentals and Applications*, Wiley, New york, 1980.

[5] A. M. Bond, N. W. Duffy, S. X. Guo, J. Zhang and D. Elton, *Analytical Chemistry*, 2005, **77**, 186A-195A.

[6] S. O. Engblom, J. C. Myland and K. B. Oldham, *Journal of Electroanalytical Chemistry*, 2000, **480**, 120-132.

[7] A. A. Sher, A. M. Bond, D. J. Gavaghan, K. Harriman, S. W. Feldberg, M. W. Duffy, S. X. Guo and J. Zhang, *Analytical Chemistry*, 2004, **76**, 6214-6228.

[8] B. D. Fleming, J. Zhang, A. M. Bond, S. G. Bell and L. L. Wong, *Analytical Chemistry*, 2005, **77**, 3502-3510.

[9] S. X. Guo, J. Zhang, D. M. Elton and A. M. Bond, *Analytical Chemistry*, 2004, **76**, 166-177.

[10] F. Marken, A. Bhambra, D. Kim, R. Mortimer and S. Stott, *Electrochem. Commun.*, 2004.

[11] A. J. Bard and L. R. Faulkner, in *Electrochemical Methods*, John Wiley & Sons, New York, Editon edn., 2001, p. 373.

[12] D. A. Buttry and F. C. Anson, *J. Am. Chem. Soc*, 1983, **105**, 685.

[13] A. J. Bard and L. R. Faulkner, in *Electrochemical Methods*, John Wiley & Sons, New York, Editon edn., 2001, p. 474.

[14] N. S. Lawrence, M. Pagels, S. F. J. Hackett, S. McCormack, A. Meredith, T. G. J. Jones, G. G. Wildgoose, R. G. Compton and L. Jiang, *Electroanalysis*, 2007, **19**, 424-428.

Summary

The work carried out in this thesis primarily involved the formation and characterisation of TiO_2 mesoporous films deposited onto ITO electrodes with applications as novel sensory devices. The films were deposited using a layer-by-layer methodology involving i) dip of substrate into a TiO_2 particle solution, ii) dip of substrate into a organic binder solution. The range of binders used includes: molecular binders (such as phytic acid), polyelectrolytes (such as poly(diallyl-dimethylammonium chloride) and Nafion®) and redox active species (such as flavin adenine dinucleotide). The range of nanoparticles used to prepare new composite materials was also extended to include larger 40nm diameter TiO_2 nanoparticles, SnO_2 nanoparticles (ca. 20nm diameter), TiO_2 nanotubes and gold nanoparticles (ca. 20nm diameter). Each new composite material was shown to be stable and with pores capable of immobilising redox active species, when characterised both electrochemically and using surface techniques such as FEGSEM, AFM or SAXS/WAXS.

Thin mesoporous films of TiO_2 were demonstrated to allow immobilisation of redox active molecules such as ferrocenylmethyl-trimethylammonium$^+$ or FAD. Electron exchange between the oxide host and the organic guest was shown to be dependent on the availability of a sufficient concentration of electrons/holes in the oxide and the kinetics of electron tunnelling. For both a TiO_2-Nafion and a TiO_2-FAD film electrode, two types of voltammetric signal were observed; one shown to be reduction of the redox active species immobilised on TiO_2 but with electron transfer occurring directly from ITO and the second as reduction of the redox active species by diffusion of electrons through the TiO_2 structure. Further investigation of this electron transfer mechanism using LAMSV allowed an EC' type mechanism for the reduction of ferrocenylmethyl-trimethylammonium$^+$, via the TiO_2-Nafion film, to be concluded. At sufficiently negative potentials, voltammetry and impedance measurements suggest very fast transport of electrons within the oxide films, and an entirely new type of measurement (employing a TiO_2 phytate – TiO_2 FAD mixed film) allowed a realistic estimate for the electron diffusion coefficient to be obtained as 10^{-6} m^2s^{-1} consistent with other literature estimates. Furthermore, clear evidence

for a change in electronic structure upon calcination of TiO_2 composite films was obtained on comparison of the voltammetric responses for a TiO_2-FAD electrode and calcined TiO_2 electrode with FAD immobilised from solution. It is possible that the calcination process has resulted in better inter-particle contact, resulting in improved mobility of electrons through the TiO_2 structure.

Properties including high surface area, porosity, low cost of preparation and non-toxicity make thin mesoporous TiO_2 films desirable for a range of analytical, sensor and catalytic applications. Each composite in this thesis has shown promise for a range of applications. The low level detection of nitric oxide (NO) was shown at a TiO_2-gold composite. Although further mechanistic evaluation into the reduction of NO on gold is required, this composite shows promise as a potential biosensor. The preference for cationic redox systems allowed the binding sites of TiO_2 nanotubes to be determined, as well as adsorption of the protein cytochrome *c*. The evaluation of proteins is important for both mechanistic details to be obtained as well as applications as sensory devices. Unfortunately both 40nm TiO_2 films and SnO_2-PDDAC composites were shown to be unsuitable for the immobilisation of the protein hemoglobin. It was shown that not only did the protein denature but total demetallation occurred. However under milder deposition conditions and in the absence of phosphate, some evidence for heme immobilisation was found, which may aid further development of composites that are suitable for protein immobilisation. Finally a TiO_2-Nafion® film with immobilised ferrocenylmethyl-trimethylammonium+ was explored as a potential reference-free pH probe, using the LAMSV to simplify data evaluation. Although the probe showed a linear response only over an acidic pH range, further development to a wide pH range would be possible by exploring other suitable redox systems.

Publications

- "SnO_2-Poly(diallyl-dimethylammonium chloride) Films: Electrochemical Evidence for Heme-Protein Absorption, Denaturation, and Demetallation" E. V. Milsom, H. A. Dash, T. A. Jenkins, C. M. Halliwell, A. Thetford, N. Bligh, W. Nogala, M. Opallo, F. Marken, *Journal of Electroanalytical Chemistry*, in press.
- "Electrocatalytic oxidation of nitric oxide at TiO_2–Au nanocomposite film electrodes", E. V. Milsom, J. Novak, M. Oyama, F. Marken, *Electrochemistry communications,* 2007, 9: 436-442.
- "Layer-by-layer deposition of open-pore mesoporous TiO_2-Nafion® film electrodes", E. V. Milsom, J. Novak, S. J. Green, X. Zhang, S. J. Scott, R. J. Mortimer, K. Edler, F. Marken, *Journal of Solid State Electrochemistry*, 2007, 11: 1109-1117.
- "The effects of conductivity and electrochemical doping on the reduction of methemoglobin immobilized in nanoparticulate TiO_2 films", E. V. Milsom, H. A. Dash, T. A. Jenkins, M. Opallo, F. Marken, *Bioelectrochemistry,* 2006, 70: 221-227.
- "Redox Processes in Mesoporous Oxide Membranes: Layered TiO_2 Phytate and TiO_2 Flavin Adenine Dinucleotide Films", E. V. Milsom, H. R. Perrott, L. M. Peter, F. Marken, *Langmuir,* 2005, 21 (21): 9482-9487
- "A Novel Cation-Binding TiO_2 Nanotube Substrate for Electro- and Bioelectro-Catalysis", D. V. Bavykin, E. V. Milsom, F. Marken, Duk-Hyun Kim, Jason Riley, F.C. Walsh, K. H. El-Abiary, A.A. Lapkin, *Electrochemistry Communications,* 2005, 7 (10): 1050-1058.